

NEW MATERIALS AND PROCESSING TECHNIQUES FOR  
BIOMEDICAL APPLICATIONS

DEVELOPMENT OF NEW COLLOIDAL AND ELECTROCHEMICAL  
PROCESSING TECHNIQUES FOR ORTHOPAEDIC IMPLANT  
COATINGS AND BIOSENSORS

By AMANDA CLIFFORD, B.Eng

A Thesis Submitted to the School of Graduate Studies in Partial Fulfilment of the  
Requirements for the Degree Doctor of Philosophy in Materials Science and Engineering

McMaster University

© Copyright by Amanda Clifford, September 2019

McMaster University DOCTOR OF PHILOSOPHY (2019) Hamilton, Ontario (Materials  
Science and Engineering)

TITLE: Development of new colloidal and electrochemical processing techniques for  
orthopaedic implant coatings and biosensors

AUTHOR: Amanda Clifford, B. Eng (McMaster University)

SUPERVISOR: Dr. Igor Zhitomirsky, Distinguished Engineering Professor, Ph.D.,  
P.Eng.

NUMBER OF PAGES: xix, 176

## **LAY ABSTRACT**

New coatings for biomedical implant materials and their related manufacturing processes must be developed to increase the lifespan of clinically used orthopaedic implants to prevent painful and costly revision surgeries. Coatings that consist of bioactive materials increase the lifespan of orthopaedic implants by decreasing scar tissue formation and inflammation, as well as improving the quality of the chemical and physical connection at the interface between the synthetic implant and natural bone. Bone is a natural composite material, so when designing replacement materials, we aim to imitate the natural chemical composition and structure of human bone.

One manufacturing technique that shows great promise for fabrication of composite coatings that mimic natural bone is called electrophoretic deposition (EPD), which uses an electric field to deposit charged materials on a conductive substrate. The primary challenge when manufacturing materials using EPD, is the coagulation and non-uniform distribution of particles in the precursor suspension, which leads to undesirable properties in the final coatings. One way we can circumvent this issue, is through use of dispersing agents, which are small charged or uncharged molecules that separate particles in a suspension by electrostatic repulsion, physical separation or some combination of both. Conventional dispersing agents have been used successfully for other applications, but they are often toxic and cannot be used for the



fabrication of biomedical materials. This work describes the discovery of new dispersing agents, biomedical coatings and manufacturing processes for the fabrication of coatings that not only increase implant lifespan, but also have other functions, such as biosensing for disease detection.

## ABSTRACT

Development of a new generation of nanocomposite biomedical implant coatings that contain bioactive ceramics and polymers *and* tailored surface features, both of which promote cell adhesion, proliferation, and interlocking at the bone tissue/implant interface, is crucial to extending the lifespan of orthopaedic implants. Use of combined colloidal and electrochemical processing techniques, in particular electrophoretic deposition (EPD), have the ability to fabricate these new multi-component materials with relative ease. They also can be used to fabricate nanostructures and surface topography, that mimic the structure of human skeletal tissue at the nanoscale. Furthermore, colloidal-electrochemical processing techniques may also be easily upscaled, towards clinical product development and mass manufacturing, unlike many processing techniques commonly used in nanotechnology.

Since the success of EPD depends on the use of a stable colloidal precursor, barriers to widespread use of colloidal-electrochemical methods for fabrication of these novel biomaterials, is the lack of efficient and biocompatible dispersants and extractors. One approach to developing suitable dispersing and extracting agents lies in deriving inspiration from the natural world, also known as biomimetics. Based on this approach, new extracting agents inspired by the chemical structure of mussel adhesive proteins (MAPs) were discovered for the efficient particle extraction and formation of organic-inorganic composite films, containing hydroxyapatite (HA) nanorods. Building upon this approach, we utilized catechol (CAT), the functional group in MAPs that allows for their ultra-strong adhesion, and functionalized amine-containing biopolymers. We used chitosan (CHIT) and poly-L-lysine (PLL) as model biopolymers and found that CAT

functionalization imparted remarkable properties such as robust adhesion, stability across a wider pH range, and redox-capacitance. Future applications of these films were explored, including not only orthopaedic implant applications, but also electrochemical and photoelectrochemical sensing applications. Finally, biomimetic inspiration was derived from the human digestive system, to use bile acid salts (BAS) as powerful solubilizing, charging, dispersing and film-forming agents for the fabrication of composite coatings, containing water insoluble drugs. These coatings can be used for local drug delivery of anti-biotics, to prevent surgical infection post-implantation, and use of BAS surfactants paves the way for solubilization and dispersion of other hydrophobic functional drugs and molecules, as well as fabrication of functional composite films using EPD.

## ACKNOWLEDGEMENTS

First, I would like to give my utmost thanks to my supervisor, Dr. Igor Zhitomirsky. He is one of the most humble, kind, and intelligent scientists I have ever had the pleasure of knowing and I will forever be grateful for his supervision and mentorship.

I would also like to express my deepest gratitude to Dr. Kathryn Grandfield, who provided me with endless career guidance. I will forever be grateful and hope to pass forward the mentorship you have shown me to another young woman in science.

I would like to acknowledge members of the Zhitomirsky lab and my office mates in JHEA203C for making everyday more enjoyable—thanks to fun times and great conversations with colleagues such as yourselves.

Finally, I would like to thank my parents Pamela and D'Arcy for fostering a love of learning from an early age, as well as my husband Rami for his endless encouragement and support in all my endeavours. Special acknowledgment goes to my father D'Arcy for inspiring me to pursue materials science and engineering.

## TABLE OF CONTENTS

|   |             |
|---|-------------|
| <b>Lay Abstract.....</b>                                    | <b>iii</b>  |
| <b>Abstract.....</b>  | <b>v</b>    |
| <b>Acknowledgements.....</b>                                | <b>vii</b>  |
| <b>Table of Contents.....</b>                               | <b>viii</b> |
| <b>List of Figures and Tables.....</b>                      | <b>xii</b>  |
| <b>List of Abbreviations.....</b>                           | <b>xvii</b> |
| <b>Declaration of Academic Achievement.....</b>             | <b>xix</b>  |
| <b>Chapter 1: Introduction.....</b>                         | <b>1</b>    |
| 1.1 Overall Context.....                                    | 1           |
| 1.2 Thesis Overview.....                                    | 5           |
| 1.3 References.....   | 9           |
| <b>Chapter 2: Literature Review.....</b>                    | <b>11</b>   |
| 2.1 Orthopaedic Implant Materials.....                      | 11          |
| 2.1.1 Bioactivity of Materials.....                         | 11          |
| 2.1.2 Metallic Materials for Orthopaedic Applications.....  | 13          |
| 2.1.2.1 Stainless Steels and Cobalt-Chromium Alloys.....    | 13          |
| 2.1.2.2 Titanium and Ti Alloys.....                         | 14          |
| 2.1.3 Bioceramics and Bioactive Glasses.....                | 16          |
| 2.1.3.1 Alumina and Zirconia-based Ceramics.....            | 16          |
| 2.1.3.2 Titania Ceramics.....                               | 17          |
| 2.1.3.3 Calcium Phosphates and Hydroxyapatite.....          | 18          |
| 2.1.3.4 Bioactive Glasses.....                              | 20          |
| 2.1.4 Effect of Surface Properties on Osseointegration..... | 22          |
| 2.2 Fundamentals of Electrophoretic Deposition.....         | 24          |
| 2.2.1 Particle Interaction in a Colloid: DLVO Theory.....   | 26          |
| 2.2.2 Limitations to DLVO Theory.....                       | 29          |

|  |           |
|--|-----------|
| 2.2.3 Particle Charging and Electrophoretic Mobility.....  | 31        |
| 2.2.4 Deposition Yield and Mechanism of Deposition.....  | 34        |
| 2.2.5 Biomimetic Dispersing Agents.....  | 36        |
| 2.2.6.1 Catecholic Molecules.....  | 36        |
| 2.2.6.2 Catechol-Modified Polysaccharides.....   | 40        |
| 2.2.6.3 Bile Acids and Bile Acid Salts.....  | 42        |
| 2.3 Research Objectives.....   | 44        |
| 2.4 References.....  | 45        |
| <b>Chapter 3: Biomimetically modified chitosan for electrophoretic deposition of composites.....</b>             | <b>54</b> |
| 3.1 Abstract.....  | 55        |
| 3.2 Introduction.....  | 56        |
| 3.3 Experimental.....  | 59        |
| 3.4 Results and Discussion.....  | 62        |
| 3.5 Conclusion.....  | 76        |
| 3.6 Acknowledgements.....  | 77        |
| 3.7 References.....  | 77        |
| <b>Chapter 4: Synthesis, liquid – liquid extraction and deposition of hydroxyapatite nanorod composites.....</b> | <b>84</b> |
| 4.1 Abstract.....  | 85        |
| 4.2 Introduction.....  | 85        |
| 4.3 Experimental Procedures.....   | 86        |
| 4.4 Results and Discussion.....  | 87        |
| 4.5 Conclusions.....   | 93        |
| 4.6 Acknowledgements.....  | 93        |

|  |            |
|--|------------|
| 4.7 References.....  | 93         |
| <b>Chapter 5: Biomimetic modification of poly-L-lysine and electrodeposition of nanocomposite coatings for orthopaedic applications.....</b> | <b>95</b>  |
| 5.1 Abstract.....  | 96         |
| 5.2 Introduction.....  | 97         |
| 5.3 Experimental.....  | 99         |
| 5.3.1 Chemicals.....   | 99         |
| 5.3.2 Electrochemical Coating Fabrication.....   | 100        |
| 5.3.3 Coating Characterization.....  | 101        |
| 5.3.4 Cell Culturing.....  | 102        |
| 5.3.5 Cell Metabolism.....   | 103        |
| 5.3.6 Alkaline Phosphatase Activity.....   | 103        |
| 5.4 Results and Discussion.....  | 103        |
| 5.5 Conclusion.....  | 115        |
| 5.6 Acknowledgements.....  | 116        |
| 5.7 Appendix A. Supplementary Data.....  | 116        |
| 5.8 References.....  | 120        |
| <b>Chapter 6: Aqueous electrophoretic deposition of drugs using bile acids as solubilizing, charging and film-forming agents.....</b>        | <b>125</b> |
| 6.1 Abstract.....  | 126        |
| 6.2 Introduction.....  | 126        |
| 6.3 Experimental.....  | 128        |
| 6.4 Results and Discussion.....  | 128        |
| 6.5 Conclusion.....  | 134        |
| 6.6 Acknowledgements.....  | 134        |
| 6.7 References.....  | 135        |

|   |            |
|---|------------|
| <b>Chapter 7: Integrating TiO<sub>2</sub> Nanoparticles within a Catecholic Polymeric Network Enhances the Photoelectrochemical Response of Biosensors.....</b> | <b>137</b> |
| 7.1 Abstract.....   | 138        |
| 7.2 Introduction.....   | 139        |
| 7.3 Results and Discussion.....   | 143        |
| 7.4 Conclusions.....  | 155        |
| 7.5 Methods.....  | 156        |
| 7.5.1 Chemicals.....  | 156        |
| 7.5.2 TiO <sub>2</sub> Surface Modification.....  | 157        |
| 7.5.3 Electrode Fabrication.....  | 157        |
| 7.5.4 Material Characterization.....  | 158        |
| 7.5.5 Photoelectrochemical Characterization.....  | 158        |
| 7.5.6 DNA Hybridization Experiments.....  | 159        |
| 7.6 Supporting Information.....   | 159        |
| 7.7 Acknowledgements.....   | 161        |
| 7.8 References.....   | 162        |
| <b>Chapter 8: Conclusions.....</b>  | <b>170</b> |
| 8.1 Summary of Conclusions and Contributions.....   | 170        |
| 8.2 Limitations and Future Work.....  | 172        |
| <b>Chapter 9: Contributions.....</b>  | <b>174</b> |
| 9.1 Peer-reviewed Publications.....   | 174        |
| 9.2 Patents.....  | 175        |
| 9.3 Conference Presentations.....   | 175        |



## LIST OF FIGURES AND TABLES

|   |    |
|---|----|
| Figure 1-1: Hierarchical structure of bone from the nanoscale (left) to the mesoscale (right).....  | 2  |
| Figure 2-1: Osseointegration confirmed at (A) low magnification and (B) high magnification by direct contact between bone tissue at the nanoscale using STEM HAADF TEM.....   | 12 |
| Figure 2-2: Schematic diagram illustrating dual-scale topography introduced in a two-step process. (A-C) Microscale features were introduced using 3D printing, and (F-D) nanoscale features were introduced using electrochemical anodization.....   | 23 |
| Figure 2-3: Schematic diagram of (A) cathodic EPD in a two-electrode cell and (B) cathodic EPD using (a) charged particles and (b) charged molecules.....   | 24 |
| Figure 2-4: Potential energy curves as a function of interparticle distance, $H$ , for (a) a stable colloidal suspension and a (b) unstable colloidal suspension containing flocculated particles.....  | 28 |
| Figure 2-5: Schematic diagram of the various mechanisms of particle stabilization in a colloid, including (a) Electrostatic stabilization, (b) steric stabilization, and (c) electrosteric stabilization.....   | 30 |
| Figure 2-6: Schematic diagram of the diffuse or electrical double layer and electrical potential as a function of distance, where (a) is the surface charge, (b) Stern layer and (c) diffuse-layer of oppositely charged ions.....  | 32 |
| Figure 2-7: Zeta potential as a function of pH for charged ceramic particles dispersed in an aqueous medium.....  | 33 |
| Figure 2-8: Chemical structure of catechol molecule and diagram of mechanism of mussel surface adhesion. (B) chemical structures of catechol-family molecules.....  | 37 |
| Figure 2-9: (A) Schematic diagram of various configurations of catecholic bonding with metal oxides, including (a) chelating, (b) inner sphere bridging, (c) outer sphere bridging and (d) carboxylic adsorption. (B) UV-vis spectra of unmodified $\text{TiO}_2$ nanoparticles (A) compared to catechol-modified $\text{TiO}_2$ nanoparticles (B-F), indicating absorption shifting to longer wavelengths..... | 39 |
| Figure 2-10: Current electrochemical method for catechol functionalization of chitosan.....   | 42 |
| Figure 3-1: Chemical structures of (A) CHIT, (B) DHBA and (C) CHIT-DHBA.....  | 62 |

|   |    |
|---|----|
| Figure 3-2: SEM image of a cross section of a CHIT-DHBA film (F) on a platinized silicon (Si) wafer substrate.....  | 63 |
| Figure 3-3: FTIR spectra of as-received (a) DHBA and (b) CHIT powders, (c) DHBA modified CHIT powders and (d) deposited CHIT-DHBA.....  | 64 |
| Figure 3-4: CVs for (A) pure CHIT and (B) CHIT-DHBA deposited on Pt in Hank's balanced salt solution, collected at a scan rate of $5 \text{ mV s}^{-1}$ , the arrows show increasing cycle number.....  | 65 |
| Figure 3-5: CVs for (a) pure CHIT and (b) CHIT-DHBA deposited on Au in phosphate buffered saline ( $\text{pH} = 7$ ) containing $50 \mu\text{M Ru}(\text{NH}_3)_6\text{Cl}_3$ , collected at a scan rate of $5 \text{ mV s}^{-1}$ .....   | 66 |
| Figure 3-6: TEM image of Ag particles, prepared by reduction of $\text{Ag}^+$ in $\text{AgNO}_3$ solutions using DHBA as a reducing agent.....  | 67 |
| Figure 3-7: X-ray diffraction patterns of (a) Ag particles, prepared by reduction of $\text{Ag}^+$ in $\text{AgNO}_3$ solutions using DHBA as a reducing agent and (b) CHIT-DHBA-Ag deposit prepared by EPD (● – peaks, corresponding to JCPDS file 04-0783 for Ag).....  | 68 |
| Figure 3-8: Adsorption of CHIT-DHBA on inorganic particles, involving (A) bridging and (B) chelating bonding to metal atoms (M) on the particle surface.....  | 69 |
| Figure 3-9: CV for CHIT-DHBA-Ag, coated on Pt in Hank's balanced salt solution, collected at a scan rate of $5 \text{ mV s}^{-1}$ , the arrow shows increasing cycle number.....  | 70 |
| Figure 3-10: SEM images of (A) pure CHIT-DHBA, (B) CHIT-DHBA- $\text{TiO}_2$ , (C) CHIT-DHBA-HA and (D) CHIT-DHBA-Ag films, prepared by EPD.....  | 72 |
| Figure 3-11: XRD patterns of (a) CHIT-DHBA-HA, (b) CHIT-DHBA- $\text{TiO}_2$ and (c) CHIT-DHBA- $\text{TiO}_2$ -HA films, prepared from $0.5 \text{ g L}^{-1}$ $\text{CHIT}^+$ -DHBA solutions, containing (a) $1 \text{ g L}^{-1}$ HA, (b) $1 \text{ g L}^{-1}$ $\text{TiO}_2$ and (c) $1 \text{ g L}^{-1}$ HA and $1 \text{ g L}^{-1}$ $\text{TiO}_2$ , (■ - peaks corresponding to JCPDS file 09-0432 for HA, ● - peaks corresponding to JCPDS file 021-1276 for $\text{TiO}_2$ )..... | 73 |
| Figure 3-12: Tafel plots in Hank's solutions for (a) uncoated stainless steel and (b) coated stainless steel by deposition from $1 \text{ g L}^{-1}$ $\text{TiO}_2$ suspension, containing $0.5 \text{ g L}^{-1}$ $\text{CHIT}^+$ -DHBA.....  | 75 |
| Figure 4-1: (A) Chemical structure of LG, (B) adsorption of LG, involving (a) bridging, (b) chelation, (C) chemical structure of HDPA, (D) adsorption of HDPA, involving (a, b) chelation, (c, d) bridging.....   | 88 |

|   |     |
|---|-----|
| Figure 4-2: (A) X-ray diffraction pattern of HA (●- JCPDS file 09-0432), (B) TEM image of HA, (C) schematic of liquid-liquid extraction, (D) (a) as precipitated HA, (b) HA extraction using LG, (c) HA extraction using HDPA.....  | 89  |
| Figure 4-3: FTIR spectra of (a) HA, extracted using LG, (b) HA, extracted using HDPA, (c) LG (d) HDPA.....  | 90  |
| Figure 4-4: SEM images of (A) HA powder after drying, arrows show agglomerates, (B) HA-PMMA prepared using LG, (C) HA-PMMA prepared using HDPA.....   | 92  |
| Figure 5-1. Chemical structure of (A) PLL, (B) DHBA and (C) PLL-DHBA.....   | 104 |
| Figure 5-2: UV-vis spectra of (a) PLL, (b) DHBA and (c) PLL-DHBA. Insert: (a) pure PLL, (b) PLL-DHBA, and (c) pure DHBA in solution.....  | 105 |
| Figure 5-3: X-ray diffraction patterns for (a) PLL-DHBA-HA, (b) PLL-DHBA-TiO <sub>2</sub> and (c) PLL-DHBA-HA-TiO <sub>2</sub> , (■ – corresponds to JCPDS file 00-024-0033 for HA, ● – corresponds to JCPDS file 01-089-0553 TiO <sub>2</sub> , and ▲ – corresponds to JCPDS file 00-044-1294 for Ti substrate).....   | 108 |
| Figure 5-4: SEM images of PLL-DHBA-HA coatings at (A) low and (B) high magnification, exhibiting dual-scale topography.....   | 109 |
| Figure 5-5: AFM results for (A) PLL-DHBA-HA, (B) PLL-DHBA-TiO <sub>2</sub> and (C) PLL-DHBA-HA-TiO <sub>2</sub> . PLL-DHBA-HA-TiO <sub>2</sub> exhibited the greatest surface roughness, followed by PLL-DHBA-HA and then PLL-DHBA-TiO <sub>2</sub> .....   | 110 |
| Table 5-1: Comparison of average contact angles and average roughness for PLL-DHBA coatings.....  | 112 |
| Figure 5-6: (A) Cell metabolism results for EPD films at 1 and 3-day time points. Cell metabolism showed significant increases from 1 to 3 days for the PLL-DHBA-TiO <sub>2</sub> film only ( $p < 0.05$ ). Additionally, the PLL-DHBA-TiO <sub>2</sub> film demonstrated significantly greater cell metabolism at 3 days compared to the other EPD films. Errors bars represent standard deviation. (B) ALP activity results for EPD films at 1 and 3-day time points. ALP activity showed significant increases from 1 to 3 days for the PLL-DHBA-TiO <sub>2</sub> film only ( $p < 0.05$ ). The PLL-DHBA-TiO <sub>2</sub> film demonstrated significantly greater ALP activity at 3 days compared to the other EPD films ( $p < 0.05$ )..... | 114 |
| Figure 5-S1: FTIR spectrum of PLL-DHBA.....   | 116 |
| Figure 5-S2: Representative images of PLL-DHBA coatings after adhesive tape test.....   | 117 |

|  |     |
|--|-----|
| Figure 5-S3: Chemical adsorption of PLL-DHBA involving interactions with metal ions (M) on the inorganic particle surface: (A) bridging and (B) chelating bonding.....   | 118 |
| Figure 5-S4: SEM images of (A,B) PLL-DHBA-TiO <sub>2</sub> and (C,D) PLL-DHBA-HA-TiO <sub>2</sub> coatings at low and high magnification, exhibiting dual-scale topography.....  | 119 |
| Figure 5-S5: Contact angle results for (A) PLL-DHBA, (B) PLL-DHBA-HA, (C) PLL-DHBA-TiO <sub>2</sub> , and (D) PLL-DHBA-HA-TiO <sub>2</sub> . All coatings were hydrophilic, but PLL-DHBA-HA exhibited the greatest hydrophilicity, followed by PLL-DHBA-TiO <sub>2</sub> , PLL-DHBA-HA-TiO <sub>2</sub> , and PLL-DHBA.....  | 120 |
| Figure 6-1: Chemical structures of ChNa, DchNa, TC and IB.....   | 129 |
| Figure 6-2: CVs for cycles 1–5 in (A) ChNa-TC, (B) ChNa-IB, (C) DchNa-TC, and (D) DchNa-IB solutions.....  | 131 |
| Figure 6-3: XRD patterns of deposits prepared from solutions (A) (a) ChNa-TC, (b) DchNa-TC and (B) (a) ChNa-IB, (b) DchNa-IB (■ – JCPDS file 039–1985 of TC, ▼ - JCPDS file 032–1723 of IB, ◆ - JCPDS file 015–1048 of ChH, ● – JCPDS file 008–0759 of DChH).....  | 132 |
| Figure 6-4: SEM images of films, prepared from (A) ChNa, (B) DchNa, (C) ChNa-TC, (D) DchNa-TC, I ChNa-IB and (F) DchNa-IB solutions.....   | 133 |
| Figure 7-1: Chemical characterization of P25-TiO <sub>2</sub> modified with different ligands. (a) Chemical structures of (i) catecholic bonding of DHB to P25-TiO <sub>2</sub> , (ii) bonding between chitosan and P25-TiO <sub>2</sub> , and (iii) catecholic bonding between DHB–CHIT and P25-TiO <sub>2</sub> . (b) FTIR spectra of as-received (i) DHB and (ii) CHIT powders. FTIR spectra of P25-TiO <sub>2</sub> modified with (iii) CHIT, (iv) DHB, and (v) DHB–CHIT.....  | 144 |
| Figure 7-2: Structural, optical, and photoelectrochemical characterizations of films created from unmodified and functionalized P25-TiO <sub>2</sub> nanoparticles. (a) Schematics of (i) unmodified P25-TiO <sub>2</sub> , (ii) DHBA-modified P25-TiO <sub>2</sub> , (iii) chitosan-modified P25-TiO <sub>2</sub> , and (iv) DHBA–chitosan-modified P25-TiO <sub>2</sub> . Images demonstrating scanning electron micrographs (b), UV/visible absorbance (c), and IPCE (d) of films created from P25-TiO <sub>2</sub> nanoparticles demonstrated in (a). The inset in (d) demonstrates the mechanism of photoelectrochemical oxidation of ascorbic acid (AA) using P25-TiO <sub>2</sub> ..... | 147 |
| Figure 7-3: Enhancing the base photocurrent of the P25-TiO <sub>2</sub> electrodes. (a) PEC current density measurements for P25-TiO <sub>2</sub> with different surface functionalization and their respective current response (left) and as summarized in bar plots (right). The inset demonstrates the spectrum of the optical excitation source. “D” denotes DHB, and “C” denotes chitosan. (b) PEC current density measurements with increasing P25-TiO <sub>2</sub> concentration in a P25-TiO <sub>2</sub> –DHB–CHIT film (left) and as summarized as bar plots (right).   |     |

Error bars represent one standard deviation and 1–6× concentration refers to 33.3, 66.6, 99.9, 133.2, 166.5, and 199.8 g L<sup>-1</sup>, respectively.....150

Figure 7-4: Photoelectrochemical DNA detection using TiO<sub>2</sub>–DHB–CHIT electrodes. (a) Scanning electron micrograph of TiO<sub>2</sub>–DHB–CHIT electrodes. (b) Schematic demonstration of the biofunctionalization of electrodes with probe DNA, hybridization with complementary target DNA, and photoelectrochemical detection using ascorbic acid as the reporter. (c) Photocurrent density of bare, probe-modified, and probe-modified electrode hybridized with complementary DNA target (+target). (d) Percentage current decrease measured between probe-modified electrodes incubated with matched (complementary) and mismatched target DNA. Error bars represent one standard deviation.....152

Figure 7-S1: Raman spectroscopy of i) unmodified P25-TiO<sub>2</sub>, ii) DHBA-modified P25-TiO<sub>2</sub>, iii) chitosan-modified P25-TiO<sub>2</sub>, and iv) DHBA-chitosan-modified P25-TiO<sub>2</sub>.....159

Figure 7-S2: Bandgap measurements of modified TiO<sub>2</sub> nanoparticles

Diffuse reflectance spectroscopy was performed on photo-electrodes with different surface functionalization. Bandgap of 3.04 eV was obtained for all four materials by extrapolating the linear portion of the obtained curves to determine the x-intercept. No significant change in bandgap was seen in either of the functionalizations as compared to bare P25-TiO<sub>2</sub>.....160

Figure 7-S3: Stability measurements of electrodes fabricated with increasing P25-TiO<sub>2</sub> concentration in a P25-TiO<sub>2</sub>-DHB-CHIT film.....161

Figure 7-S4: Photocurrent response following storage in dark condition at 4°C for 7 days...161

## LIST OF ABBREVIATIONS AND SYMBOLS

|      |   |
|------|---|
| AC   | Alternating Current                     |
| AFM  | Atomic Force Microscopy                 |
| ALG  | Alginic Acid                            |
| AT   | Anti-Thrombin                           |
| ATZ  | Alumina Toughened Zirconia              |
| BA   | Bile Acids                              |
| BAS  | Bile Acid Salts                         |
| BG   | Bioactive Glass                         |
| BSA  | Bovine Serum Albumin                    |
| CaP  | Calcium Phosphate                       |
| CAT  | Catechol                                |
| CHIT | Chitosan                                |
| CV   | Cyclic Voltammetry                      |
| DC   | Direct Current                          |
| DNA  | Deoxyribonucleic Acid                   |
| EPD  | Electrophoretic Deposition              |
| FTIR | Fourier Transform Infrared Spectroscopy |
| GOx  | Glucose Oxidase                         |
| HA   | Hydroxyapatite                          |
| Hb   | Hemoglobin                              |
| HDPA | Hexadecylphosphonic Acid                |
| HLA  | Hyaluronic Acid                         |
| IB   | Ibuprofen                               |
| IPCE | Incident Photon to Current Efficiency   |
| LG   | Lauryl Gallate                          |

|                 |                                  |
|-----------------|----------------------------------|
| PEC             | Photoelectrochemical             |
| PLL             | Poly-L-lysine                    |
| PMMA            | Polymethylmethacrylate           |
| MO <sub>x</sub> | Metal Oxide                      |
| MWCNTs          | Multi-Walled Carbon Nanotubes    |
| NPs             | Nanoparticles                    |
| SEM             | Scanning Electron Microscopy     |
| SS              | Stainless Steel                  |
| TC              | Tetracycline                     |
| TCP             | Tricalcium Phosphate             |
| TEM             | Transmission Electron Microscopy |
| THA             | Total Hip Arthroplasty           |
| UV-Vis          | Ultraviolet-Visible Spectroscopy |
| XRD             | X-Ray Diffraction                |
| YSZ             | Yttria-Stabilized Zirconia       |
| ZTA             | Zirconia Toughened Alumina       |

## DECLARATION OF ACADEMIC ACHEIEVEMENT

This dissertation was written to fulfill requirements of the Ph.D. degree in the Department of Materials Science and Engineering at McMaster University. All work described was undertaken from September 2016 to September 2019.

The majority of the experiments described in the following written document were conceived of and conducted by the author of this thesis, in consultation with the supervisor, Dr. Igor Zhitomirsky. Exceptions are as follows:

*Chapter 3:* Dr. Xin Pang obtained TEM images of in-situ reduced Ag nanoparticles in Figure 6, and Mr. Ryan Poon collected the XRD patterns for DHBA-Ag and CHIT-DHBA-Ag found in Figure 7.

*Chapter 4:* Dr. Mustafa Ata obtained SEM images of the HA-PMMA composite film surfaces for Figure 4.

*Chapter 5:* Mr. Bryan Lee conducted *in vitro* cell testing and contributed to the manuscript.

*Chapter 7:* Ms. Amanda Victorious conducted all PEC and DNA experiments, and Mr. Sudip Saha collected UV-vis and IPCE data. The final manuscript was written in a collaborative effort between Ms. Amanda Victorious and myself. Mr. Sudip Saha contributed to the manuscript, and Dr. Leyla Soleymani assisted with editing of the final manuscript and served as the PI for this work.



## **Chapter 1: Introduction**

### **1.1 Overall Context**

Bone is a natural hierarchical organic-inorganic composite material that at the nanoscale consists of carbonated HA nanoplates contained within a matrix of type I collagen [1,2]. The remarkable mechanical properties of bone, including high strength and fracture toughness can be attributed to its hierarchical structure [3]. Many efforts have been made to develop materials to replace damaged skeletal tissue [4], but this has proved challenging due to the aggressive physiological environment and complex mechanical loading conditions that must be withstood by the implant material. Clinical implant outcomes and bone healing are both dependent both on biological and mechanical properties [5], but early iterations of orthopaedic implant materials focused on selecting materials that were (i) bioinert and (ii) mechanically stabilized the damaged bone tissue or joint. As such, metallic materials, including stainless steel, titanium alloys and cobalt-chromium alloys have a long history of clinical use for the treatment of bone fractures and defects due to their mechanical properties and adequate biocompatibility. After many years of clinical use, it was found that metallic materials are well-suited for skeletal repair, but their lifespan is limited due to their inability to form a sufficient bond with bone [7,8]. There are also continued concerns of toxic metal ion release due to implant corrosion and generation of wear particles at the interface of the femoral head and acetabular cup [9,10].

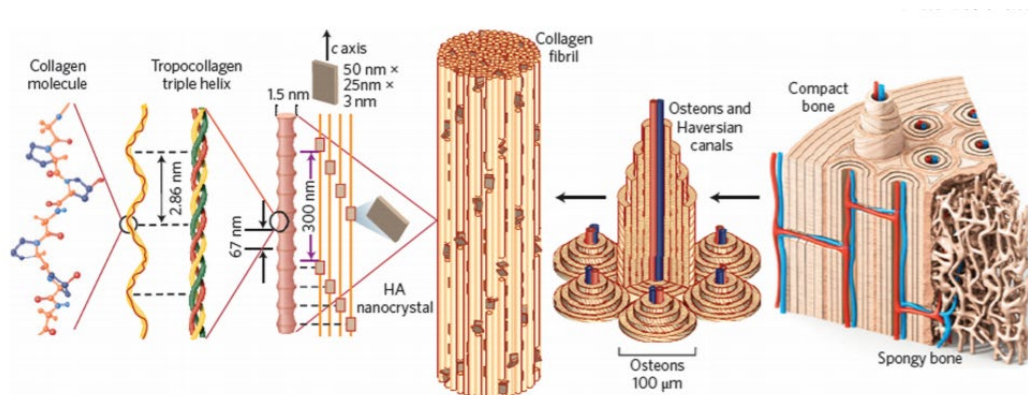


Figure 1-1: Hierarchical structure of bone from the nanoscale (left) to the mesoscale (right) [5]. Copyright © 2014, Springer Nature.

It is believed that the key to increasing orthopaedic implant lifespan may be to imitate the structure of natural bone through use of organic-inorganic composite coatings, which contain an organic component that mimics natural collagen and a mineral inorganic component, which is chemically similar to the inorganic constituent of bone. It is believed that the use of such coatings will simultaneously prevent the formation of fibrous scar tissue [11] and strengthen the chemical and mechanical bond at the bone-implant interface, a process termed osseointegration [8]. Other surface characteristics that may be tailored to affect osseointegration at the bone-implant interface include surface roughness, wettability and the presence of both micro- and nano-scale features in the surface topography [12–14]. In addition to tailoring implant surface chemistry and topography, bacterial infection has an adverse effect on the quality of the bond formed at the bone-tissue implant interface, as inflammation affects the healing cascade of bone [24]. As such, preventing infection is one of the biggest challenges surrounding biomedical device implantation. One potential

solution is to incorporate antibiotic drugs, nanoparticles and morphogenic proteins into the implant coating [24].

The primary challenge to the incorporation of such functional organic materials into implant coatings is the use of traditional high-temperature processing techniques, which can denature or structurally deform the organic components of the coating. For instance, the current processing method used clinically for the application of hydroxyapatite (HA) on orthopaedic and dental implants is plasma-spraying, which prevents the incorporation of drugs and enzymes, as they become denatured at elevated temperatures. Plasma-spraying as a processing technique has several other disadvantages, including poor control over coating thickness, uniformity, crystallinity and coating adhesion. In addition to the aforementioned disadvantages, the resulting coatings lack optimal surface topography. This has generated the need for new low temperature techniques with increased control over chemical composition, coating thickness, uniformity, topography and adhesion.

EPD is a low temperature coating technique which utilizes electrophoresis for the deposition of charged polymers, molecules and particles [15]. EPD has been used previously for the fabrication of organic-inorganic composite biomaterials that include functional biopolymers such as CHIT [16,17], ALG [18,19], HLA [20], and PLL [21], combined with advanced bioceramics and glasses, such as BG [17,22], HA [16,21], and TiO<sub>2</sub> [17,23]. Proteins and enzymes such as AT [24], BSA [25] and GOx [26] have also been incorporated. The use of organic-inorganic nanocomposite coatings on metallic implants, manufactured using EPD, has the potential to meet the complex requirements essential for implant viability. The primary challenge encountered during organic-inorganic

coating development is prevention of agglomeration and sufficient dispersion of inorganic nanoparticles within the organic matrix. An additional challenge to the fabrication of advanced coatings for biomedical implant applications is the incorporation of anti-biotic and anti-inflammatory drugs into the coating matrix. Incorporation of such drugs is challenging due to the reality that ninety percent of drugs currently under investigation and almost half of all drugs used clinically exhibit poor aqueous solubility [25].

Although organic-inorganic nanocomposite biomaterials have been previously fabricated using EPD, coating adhesion in the presence of body fluid must be improved. Based off biomimetic inspiration from the mussel's ability to successfully attach to the seawall in aggressive marine conditions [27,28], biopolymers, such as CHIT, ALG and HLA have been functionalized with catechol (a functional group found in the mussels byssal plaque) to improve coating adhesion to inorganic surfaces, nanoparticles, and the mucosal layer in mammals [12]. However, the previous chemical and electrochemical techniques used to functionalize the biopolymer chitosan with catechol in the literature [13] involve complicated chemical synthesis and multiple fabrication steps.

Thus, it is of paramount importance to develop a new generation of nanocomposite biomedical implant coatings that contain advanced functional materials such as biopolymers, bioceramics, anti-bacterial agents, morphogenic proteins and enzymes. New developments in this field will result in prevention of costly and painful revision surgeries, and will extend the lifespan of orthopaedic implants. In addition to offering a solution for biomedical implant coatings, organic-inorganic nanocomposite coatings are multi-functional and may also be used as thin-film biosensors, due to the incorporation of

advanced nanomaterials and biological molecules. As such, my work describes novel techniques that have allowed for the fabrication of new organic-inorganic nanocomposite biomaterials, as well as advanced colloidal-electrochemical strategies for the deposition of multi-functional coatings for biomedical applications. My scientific methodology and approach have allowed for innovation in the fields of electrochemistry, colloidal science, biomaterials and nanotechnology, and as such addresses the need for advanced materials and coatings in medicine.

## **1.2 Thesis Overview**

A summary of the remaining chapters contained in this thesis are as follows:

Chapter 2 contains a thorough review of the strengths and limitations of current orthopaedic implant materials and coatings used clinically. The impact of material composition and surface topography on implant osseointegration are also reviewed. Finally, an overview of the fundamental colloidal science and advantages of electrophoretic deposition as a coating fabrication technique and biomimetic dispersing agents is provided.

Chapter 3 presents a facile approach for the functionalization of CHIT with catechol, utilizing a CAT-containing aldehyde molecule and a Schiff base reaction. FTIR was used to characterize CHIT functionalization, and it was confirmed that catechol was attached to the CHIT monomer by the formation of an imine bond between the amine group of CHIT and the aldehyde of the CAT-containing molecule, 3,4-dihydroxybenzylaldehyde (DHBA), post-Schiff base reaction. We discovered the electrochemical behaviour of our

CHIT films was altered upon chemical modification with CAT. Electrochemical characterization using CV revealed the redox activity of the film significantly increased due to the pseudo-capacitive contribution of the CAT molecule. To test our films for possible voltammetric sensing applications  $\text{Ru}(\text{NH}_3)_6\text{Cl}_3$  was introduced as a mediator and it was found that our films amplified the redox currents, in particular the reduction current. Building upon this discovery, we utilized the enhanced redox-activity of the coating for the *in-situ* reduction and dispersion of Ag NPs, followed by fabrication of composite Ag-CAT-CHIT films using cathodic EPD. Chemical composition of the Ag nanoparticles was determined using XRD and CV, while TEM and SEM were used to characterize the size and distribution of the Ag NPs fabricated *in-situ*. Composite films containing bioactive nanoparticles such as HA,  $\text{TiO}_2$  and HA co-deposited with  $\text{TiO}_2$  were fabricated using cathodic EPD combined with CAT-CHIT, which acted as a charging, dispersing and film forming agent. XRD and SEM were used for characterization of resulting CAT-CHIT- $\text{TiO}_2$ , CAT-CHIT-HA, and CAT-CHIT-HA- $\text{TiO}_2$  films.

Chapter 4 describes the development of a conceptually new approach for the synthesis and extraction of HA nanorods using two novel biomimetic extracting agents. LG and HDPA were used for the extraction of as-synthesized HA nanorods from the aqueous phase into a solvent phase, against the force of gravity. FTIR was used to characterize particles extracted from the solvent phase, and the mechanism of extraction was confirmed due to the presence of characteristic absorbances from LG and HDPA in the acquired spectra. Our method eliminates the drying phase in nanoparticle processing, and as such avoids the formation of large agglomerates. Extracted particles were then

used for the fabrication and subsequent characterization of nanocomposite films using SEM, which revealed the films contained well-dispersed HA nanorods within a PMMA matrix.

Chapter 5 builds upon the work presented in Chapter 3 and utilizes the Schiff base functionalization method for monomer modification of PLL with CAT. UV-vis and FTIR were used to characterize the functionalized PLL monomer and CAT functionalization was confirmed. CAT-PLL was then used for the fabrication of nanocomposite films containing HA, TiO<sub>2</sub> or HA co-deposited with TiO<sub>2</sub> using cathodic EPD. Comprehensive surface characterization was performed on the resulting coatings, including contact angle measurements, coating adhesion measurements, AFM, SEM, XRD and an *in vitro* cell culture experiment. Coating characterization revealed that our films were hydrophilic, exhibited ultra-strong adhesion, micron-scale surface roughness and surface features on both the nano- and micron-scale, and *In vitro* testing revealed that all coatings supported cell viability with statistical significance.

Chapter 6 describes the development of a new method for solubilizing water insoluble drugs and fabricating composite coatings, using BAS. In this technique, BAS are combined with model water-insoluble drugs, IB and TC. Charged, mixed micelles containing either IB or TC were formed upon mixing, due to the unique concave-convex amphiphilic structure of the BAS. Both CV and anionic EPD were used for the deposition of composite gel films, and co-deposition of IB or TC with the BAS

was confirmed using XRD. SEM was used for film characterization, and it was revealed that some BAS self-assemble to form unique porous gel structures.

Chapter 7 reports the exploration of CAT-CHIT for development of a transducing element, towards photoelectrochemical (PEC) sensing of biological macromolecules. Based on previous reports of CATs ability to modify the optical and electronic structure of semiconducting nanoparticles, we used CAT-CHIT for ligand modification of TiO<sub>2</sub> nanoparticles, to increase base current output and reduce issues related to low signal-to-noise ratios. Colloidal suspensions containing TiO<sub>2</sub> nanoparticles functionalized with either unmodified CHIT, DHBA, or CAT-CHIT, were used to fabricate composite films on an ITO/PET substrate using a drop-casting technique. FTIR, Raman Spectroscopy, UV-Vis Spectroscopy, IPCE, SEM and PEC measurements were used to thoroughly characterize the films. Characterization revealed that CAT-CHIT functionalization of TiO<sub>2</sub> resulted in the largest PEC output, compared to unmodified TiO<sub>2</sub>, CHIT-TiO<sub>2</sub> and DHBA-TiO<sub>2</sub> films. The ratio of CAT to CHIT, as well as TiO<sub>2</sub> concentration was then optimized to ensure the highest current density output prior to DNA probe functionalization. Preliminary DNA hybridization assays were conducted, and initial results confirmed that CAT-CHIT-TiO<sub>2</sub> films show great promise for use as transduction elements for signal-off biosensing applications.

Chapter 8 summarizes the significant findings of this work and major contributions to the field, as well as future work.

Chapter 9 contains a list of peer-reviewed publications and other academic contributions that were prepared throughout the duration of my doctorate degree, including patents and conference publications.



### 1.3 References

- [1] K. Grandfield, V. Vuong, H.P. Schwarcz, Ultrastructure of Bone: Hierarchical Features from Nanometer to Micrometer Scale Revealed in Focused Ion Beam Sections in the TEM, *Calcif. Tissue Int.* 103 (2018) 606–616. doi:10.1007/s00223-018-0454-9.
- [2] N. Reznikov, R. Shahar, S. Weiner, Bone hierarchical structure in three dimensions, *Acta Biomater.* 10 (2014) 3815–3826. doi:10.1016/j.actbio.2014.05.024.
- [3] S.M. Best, A.E. Porter, E.S. Thian, J. Huang, Bioceramics: Past, present and for the future, *J. Eur. Ceram. Soc.* 28 (2008) 1319–1327. doi:10.1016/j.jeurceramsoc.2007.12.001.
- [4] S.B. Goodman, Z. Yao, M. Keeney, F. Yang, The future of biologic coatings for orthopaedic implants, *Biomaterials.* 34 (2013) 3174–3183. doi:10.1016/j.biomaterials.2013.01.074.
- [5] Y. Liu, D. Luo, T. Wang, Hierarchical Structures of Bone and Bioinspired Bone Tissue Engineering, *Small.* 12 (2016) 4611–4632. doi:10.1002/smll.201600626.
- [6] M.Z. Ibrahim, A.A.D. Sarhan, F. Yusuf, M. Hamdi, Biomedical materials and techniques to improve the tribological, mechanical and biomedical properties of orthopedic implants – A review article, *J. Alloys Compd.* 714 (2017) 636–667. doi:10.1016/j.jallcom.2017.04.231.
- [7] K. Grandfield, Bone, implants, and their interfaces, *Phys. Today.* 68 (2015) 40–45. doi:10.1063/PT.3.2748.
- [8] G.O. Alrabeah, P. Brett, J.C. Knowles, H. Petridis, The effect of metal ions released from different dental implant-abutment couples on osteoblast function and secretion of bone resorbing mediators, *J. Dent.* 66 (2017) 91–101. doi:10.1016/j.jdent.2017.08.002.
- [9] D.M. Vasconcelos, S.G. Santos, M. Lamghari, M.A. Barbosa, The two faces of metal ions: From implants rejection to tissue repair/regeneration, *Biomaterials.* 84 (2016) 262–275. doi:10.1016/j.biomaterials.2016.01.046.
- [10] C.N. Elias, Y. Oshida, J.H.C. Lima, C.A. Muller, Relationship between surface

- properties (roughness, wettability and morphology) of titanium and dental implant removal torque, *J. Mech. Behav. Biomed. Mater.* 1 (2008) 234–242. doi:10.1016/j.jmbbm.2007.12.002.
- [11] B.E.J. Lee, H. Exir, A. Weck, K. Grandfield, Characterization and evaluation of femtosecond laser-induced sub-micron periodic structures generated on titanium to improve osseointegration of implants, *Appl. Surf. Sci.* 441 (2018) 1034–1042. doi:10.1016/j.apsusc.2018.02.119.
- [12] K. Gulati, M. Prideaux, M. Kogawa, L. Lima-Marques, G.J. Atkins, D.M. Findlay, D. Losic, Anodized 3D–printed titanium implants with dual micro- and nano-scale topography promote interaction with human osteoblasts and osteocyte-like cells, *J. Tissue Eng. Regen. Med.* 11 (2017) 3313–3325. doi:10.1002/term.2239.
- [13] A.R. Boccaccini, S. Keim, R. Ma, Y. Li, I. Zhitomirsky, Electrophoretic deposition of biomaterials, *J. R. Soc. Interface.* 7 (2010) S581–S613. doi:10.1098/rsif.2010.0156.focus.
- [14] X. Pang, I. Zhitomirsky, Electrodeposition of composite hydroxyapatite-chitosan films, *Mater. Chem. Phys.* 94 (2005) 245–251. doi:10.1016/j.matchemphys.2005.04.040.
- [15] S. Clavijo, F. Membrives, G. Quiroga, A.R. Boccaccini, M.J. Santillán, Electrophoretic deposition of chitosan/Bioglass® and chitosan/Bioglass®/TiO<sub>2</sub> composite coatings for bioimplants, *Ceram. Int.* 42 (2016) 14206–14213. doi:10.1016/j.ceramint.2016.05.178.
- [16] M. Cheong, I. Zhitomirsky, Colloids and Surfaces A: Physicochemical and Engineering Aspects Electrodeposition of alginic acid and composite films, 328 (2008) 73–78. doi:10.1016/j.colsurfa.2008.06.019.
- [17] Q. Chen, L. Cordero-arias, J.A. Roether, S. Cabanas-polo, S. Virtanen, A.R. Boccaccini, Alginate / Bioglass® composite coatings on stainless steel deposited by direct current and alternating current electrophoretic deposition, *Surf. Coat. Technol.* 233 (2013) 49–56. doi:10.1016/j.surfcoat.2013.01.042.
- [18] R. Ma, I. Zhitomirsky, Electrophoretic deposition of silica-hyaluronic acid and

- titania-hyaluronic acid nanocomposites, in: *J. Alloys Compd.*, 2011: pp. 510–513. doi:10.1016/j.jallcom.2010.10.111.
- [19] Y. Wang, X. Pang, I. Zhitomirsky, Electrophoretic deposition of chiral polymers and composites, *Colloids Surfaces B Biointerfaces*. 87 (2011) 505–509. doi:10.1016/j.colsurfb.2011.05.043.
- [20] K.D. Patel, A. El-Fiqi, H.-Y. Lee, R.K. Singh, D.-A. Kim, H.-H. Lee, H.-W. Kim, Chitosan–nanobioactive glass electrophoretic coatings with bone regenerative and drug delivering potential, *J. Mater. Chem.* 22 (2012) 24945. doi:10.1039/c2jm33830k.
- [21] L. Mohan, D. Durgalakshmi, M. Geetha, T.S.N. Sankara Narayanan, R. Asokamani, Electrophoretic deposition of nanocomposite (HAp + TiO<sub>2</sub>) on titanium alloy for biomedical applications, *Ceram. Int.* 38 (2012) 3435–3443. doi:10.1016/j.ceramint.2011.12.056.
- [22] K.N. Sank, I. Zhitomirsky, L.R. Berry, A.K.C. Chan, J.L. Brash, Surface modification with an antithrombin-heparin complex for anticoagulation: Studies on a model surface with gold as substrate, *Acta Biomater.* 6 (2010) 2911–2919. doi:10.1016/j.actbio.2010.02.043.
- [23] R. Ma, I. Zhitomirsky, Electrophoretic deposition of chitosan–albumin and alginate–albumin films, *Surf. Eng.* 27 (2011) 51–56. doi:10.1179/026708410X12506870724271.
- [24] S. Seuss, A.R. Boccaccini, Electrophoretic deposition of biological macromolecules, drugs, and cells, *Biomacromolecules*. 14 (2013) 3355–3369. doi:10.1021/bm401021b.
- [25] L. Li, H. Zeng, Marine mussel adhesion and bio-inspired wet adhesives, *Biotribology*. 5 (2016) 44–51. doi:10.1016/j.biotri.2015.09.004.
- [26] J.H. Waite, N.H. Andersen, S. Jewhurst, C. Sun, Mussel Adhesion: Finding the Tricks Worth Mimicking, *J. Adhes.* 81 (2005) 297–317. doi:10.1080/00218460590944602.

## **Chapter 2: Literature Review**

### **2.1 Orthopaedic Implant Materials**

#### **2.1.1 Bioactivity of Materials**

Metallic, ceramic and polymeric materials have all been used for various aspects of hard tissue repair and skeletal reconstruction. They have different degrees of bioactivity, which in terms of materials used for orthopaedic and dental applications, is defined as the degree to which new CaP and hard tissue growth is stimulated [1]. Materials that facilitate CaP and hard tissue growth may also be further divided into two categories: osteoconductive and osteoinductive. Osteoconductive materials conduct bone growth along the implant/bone tissue interface, while osteoinductive materials induce osteogenesis (formation of new hard tissue) [2,3]. Bioinert materials are defined as materials that form a physical bond with the osseous tissue but do not illicit fibrous tissue formation [1], although it should be noted that no biomaterial is truly inert-as the presence of a foreign object will always illicit an immune response [4]. Examples of bioinert materials include stainless steels, pure titanium,  $\text{Al}_2\text{O}_3$  and  $\text{ZrO}_2$  [5], and in general they are osteoconductive. Although bioinert materials directly contact the osseous tissue and form a physical bond, this does not necessarily constitute osseointegration [2,6], which requires the implant to be securely anchored to the bone tissue in addition to having physical contact [2,3]. Osseointegration is traditionally measured using visual confirmation of contact between the implant and bone tissue using light microscopy [7], but this measurement has been

considered to be insufficient due to other important considerations: anchorage of implant, quality of new osseous tissue, and characterization of the implant at smaller length scales using electron microscopy [7]. A visual representation of osseointegration at the nanoscale can be seen in Figure 2-1.

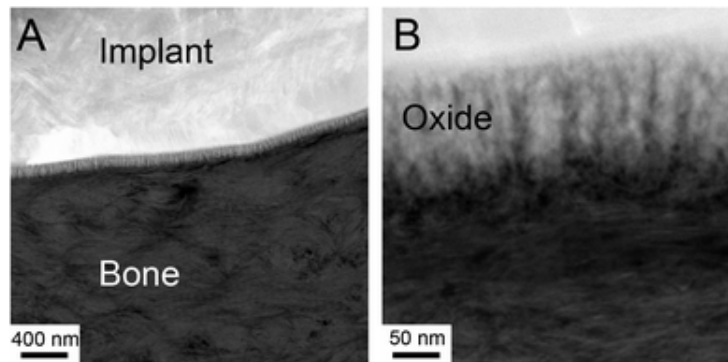


Figure 2-1: Osseointegration confirmed at (A) low magnification and (B) high magnification by direct contact between bone tissue at the nanoscale using STEM HAADF TEM. Reproduced from Ref. 8 with permission from The Royal Society of Chemistry.

The original selection criteria when selecting materials for hard tissue reconstruction was to minimize adverse response from the immune system upon implantation, and as such bioinert materials were the first materials selected for clinical use [4]. The next generation of biomaterials development involved the use of bioactive materials: to not only avoid a toxic response but also stimulate a robust healing reaction and thus enhance implant fixation. Bioactive materials are different from bioinert materials in that they not only form physical bond with the bone tissue at the interface, but also form a strong chemical bond [1]. Examples of bioactive materials include HA, calcium phosphate ceramics, and bioactive glasses such as Bioglass® 45S5. Bioactive materials can

be further categorized into resorbable and non-resorbable [4]. Ability to resorb does not indicate the materials ability to promote osteogenesis, and as a result, resorbable or non-resorbable materials can be either osteoconductive or osteoinductive.

## **2.1.2 Metallic Materials for Orthopaedic Applications**

### **2.1.2.1 Stainless Steels and Cobalt-Chromium Alloys**

Although alternatives are being continuously explored, metallic materials are still the superior choice for biomedical implants due to their reasonable degree of biocompatibility and ability to sustain the range of mechanical stresses they will be subjected to during implant lifespan [9–11]. SS was the first metallic material used clinically for THA, and AISI 316 and 316L SS in particular were commonly used as a biomedical material due to their ductility, strength, corrosion resistance, ease of manufacture and low cost [10,12,13]. Compared to other SS, the ASTM recommends stainless steels from the 316 family for biomedical implant applications because of their lower carbon content and thus increased protection against corrosion in physiological fluid [14]. AISI 316 and 316L SS are still widely used for both short-term orthopaedic applications, such as bone plates and surgical screws, and long-term applications such as total-hip or knee replacements [15]. Wear resistance of SS alloys is low compared to other metals, which is essential for THA applications to prevent generation of toxic wear particles, and thus subsequent inflammation, osteolysis and aseptic loosening [14]. Release of toxic nickel ions as a result of corrosion or wear particle generation is the primary concern associated

with the use of 316L SS, since they have shown to cause inflammation, allergic reactions, and are considered mutagenic and genotoxic [12,14]. Furthermore, long-term exposure to nickel may cause cancer, kidney and cardiovascular disease [12]. To ease concerns regarding toxic nickel ion release from 316L SS, Ni-free stainless steel (ASTM F2229) was developed, which replaced nickel with nitrogen [13]. Although nitrogen addition prevented Ni ion release, Ni-free stainless-steel alloys exhibit poor corrosion resistance and reduced fatigue behaviour in physiological conditions, and poor bioactivity compared to other metallic biomaterials [13].

To reduce generation of toxic wear particles in hopes of increasing orthopaedic implant lifespan, cobalt-chromium alloys were introduced as an alternative to 316 and 316L SS due high wear resistance and mechanical strength [13,14]. In particular, two types of cobalt-chromium alloys are used clinically for orthopaedic implant applications: (i) cobalt nickel molybdenum chromium (CoNiMoCr) and (ii) cobalt molybdenum chromium (CoMoCr) alloys [14]. CoCr alloys are also more corrosion resistant than SS, as they form a protective oxide layer in physiological environments [14]. They also exhibit higher fatigue resistance compared to medical-grade SS, but are more expensive to manufacture and concerns surrounding release of harmful metal ions (including Ni) remain [13].

#### **2.1.2.2 Titanium and Ti Alloys**

Titanium and its alloys are the most commonly used metallic biomaterial for orthopaedic applications, primarily because of their superior osseointegration, low toxicity, and high corrosion resistance [13]. Osseointegration is the degree to which a

material forms a functional connection with hard tissue at the implant/bone interface [13]. Titanium exhibits a high degree of osseointegration, while SS and CoCr alloys exhibit no osseointegration [13]. Upon implantation of SS and CoCr alloys, a layer of fibrous tissue separates the implant surface from the newly formed bone and as such, both are considered biotolerant biomaterials [12]. Since the long-term outcome of the orthopaedic implant is largely dependent on the quality of the bond at the implant/tissue interface, Ti's high osseointegration makes it the premier choice compared to other metals and their alloys. Although Ti itself is not toxic to the human body, release of toxic corrosion products, such as aluminum and vanadium ions, has continually been reported [16]. Corrosion products accumulate in the lymphatic system [1] and may have adverse health effects over long term exposure [13]. In particular, release of Al and V ions in the body from Ti alloy implantation has been correlated with diagnoses of peripheral neuropathy, osteomalacia, and Alzheimer's [14,15]. Development of alternative Ti alloys with non-allergenic strengthening elements has been proposed, but would require advanced fabrication techniques and increase the overall cost [13]. Furthermore, it should be noted that all metallic implant materials are prone to failure as a result of the stress-shielding effect, which is the local bone atrophy observed due to elastic modulus mismatch between the metallic implant and human bone [2,14,15].



### **2.1.3 Bioceramics and Bioactive Glasses**

#### **2.1.3.1 Alumina and Zirconia-based Ceramics**

$\text{Al}_2\text{O}_3$  was introduced as an alternative for metallic acetabular liners and femoral heads, in an effort to increase orthopaedic implant lifespan via reduction of wear particle generation and osteolysis [5,6].  $\text{Al}_2\text{O}_3$  is well suited in terms of both biological and mechanical properties for skeletal tissue repair because of its high mechanical strength in compression, high wear resistance and hydrophilic nature [6]. As a result, pure  $\text{Al}_2\text{O}_3$  has been used clinically for hip and knee prostheses, dental implants, and as a coating for metallic dental implants and femoral stems [6]. Although the use of  $\text{Al}_2\text{O}_3$  ceramics has decreased generation of inflammatory wear particles and osteolysis, successful osseointegration has yet to be achieved due to its bioinert nature [6].  $\text{Al}_2\text{O}_3$  also exhibits poor fracture toughness compared to other bioceramics, such as YSZ, and is susceptible to brittle fracture and subsequent catastrophic failure.

$\text{ZrO}_2$ -based ceramics were introduced as an alternative to  $\text{Al}_2\text{O}_3$  for ceramic acetabular liners and femoral heads and acetabular liners, since they are both bioinert and exhibit similar mechanical properties in terms of compressive strength and wear resistance.  $\text{ZrO}_2$  undergoes a unique transformation toughening mechanism, which allows for increased fracture toughness compared to  $\text{Al}_2\text{O}_3$  ceramics [17–19]. At room temperature  $\text{ZrO}_2$  exists in a metastable tetragonal state, but under applied stress  $\text{ZrO}_2$  transforms to the monoclinic state [18,19].  $\text{Y}_2\text{O}_3$  additions are used to stabilize medical-grade  $\text{ZrO}_2$  ceramics by preventing premature phase-transformation from the tetragonal to the monoclinic phase

at room temperature [20]. Stabilization of the tetragonal phase prevents of crack propagation at localized crack tips under ambient conditions, but after clinical use it was discovered that exposure to body fluid *in vivo* resulted in premature aging and failure of YSZ femoral heads [18]. This observed phenomena is termed low temperature thermal degradation, which describes the premature transformation from the tetragonal to the monoclinic phase under physiological conditions [17]. Furthermore, this effect results in the risk of premature implant failure during manufacturing or after surface treatments to improve osseointegration [1]. ZTA composites have emerged as an alternative to YSZ femoral heads due to a high incidence of YSZ implant failure [21]. ZTA composites are employed clinically under the tradename BioloX® delta, and have increased success rates compared to pure  $\text{Al}_2\text{O}_3$  femoral heads because of their increased fracture toughness compared to pure  $\text{Al}_2\text{O}_3$  or YSZ [21]. Based on the success of ZTA, ATZ composites are being explored for femoral head applications, although it has been reported that the mechanical properties of ZTA are superior to ATZ [19].

### 2.1.3.2 Titania Ceramics

Ti and its alloys are coated a few nanometers of naturally occurring  $\text{TiO}_2$  oxide, and it is believed that the success of titanium implants and their ability to osseointegrate can be attributed to this thin bioactive layer of  $\text{TiO}_2$  [22,23]. Although this oxide layer is advantageous in terms of osseointegration, it should be noted that this thin barrier does not provide long-term corrosion protection, prevent the release of toxic Al and V ions, or result in implant longevity [24]. One strategy to increase corrosion protection and

osseointegration is through application of a  $\text{TiO}_2$  coating to the Ti alloy substrate to improve the bioactivity of the underlying titanium substrate while still acting as a physical barrier providing corrosion protection and toxic metal ion release [24]. In recent years there has been particular interest in coatings consisting of  $\text{TiO}_2$  nanotubes, due to the potential for increased osseointegration and osteogenesis via introduction of nanoscale surface features [11,25,26], and the ability to load the nanotubes with functional molecules such as anti-bacterial drugs for post-operative infection prevention [27]. Electrochemical anodization is commonly used for fabrication of  $\text{TiO}_2$ -nanotube based coatings and offers many advantages, including the possibility to coat complex shapes such as porous Ti scaffolds [11]. Advanced coatings for increased osseointegration and infection prevention have been fabricated by deposition of HA on the nanotube surface [11], loading the nanotubes with anti-biotic drugs such as vancomycin [27], or by surface functionalization with Ag NPs [28]. Although functional orthopaedic coatings using  $\text{TiO}_2$  nanotubes have been developed, their clinical use remains limited because of concerns surrounding efficacy of coatings loaded with anti-biotics due to antibiotic resistance [28]. Coatings containing Ag NPs may offer a potential solution to prevent formation of bacterial biofilms, but it was discovered that when the concentration of Ag NPs was high enough to offer an anti-bacterial effect, the coating was rendered cytotoxic to osteoblast cells [11].

### **2.1.3.3 Calcium Phosphates and Hydroxyapatite**

CaP bioceramics were introduced clinically based on their compositional similarity to the inorganic component in human bone: carbonate substituted HA ( $\text{Ca}_5(\text{PO}_4)_{3-x}(\text{OH})_{1-x}$ ).

x) [4,29]. All CaP ceramics are considered bioactive, but whether they are resorbable depends on crystallinity and the Ca/P stoichiometric ratio [30]. HA with a higher degree of crystallinity is more stable and less resorbable than HA with a lower degree of crystallinity [13]. Pure HA has a Ca/P stoichiometric ratio of 1.67 and is non-resorbable [4]. When the stoichiometric ratio is greater than 1.67, calcium oxide (CaO) forms as an impurity phase, whereas when the stoichiometric ratio is less than 1.67, the alpha- or beta- polymorphs of tricalcium phosphate (TCP) may form [4]. HA that contains CaO or polymorphs of TCP are both considered resorbable, and are used for applications where simultaneous bone resorption and hard tissue regeneration is desirable, such as osseous defect repair [4,30,31]. It should be noted that while some deviation away from a stoichiometric Ca/P ratio of 1.67 yields ceramics with desirable properties, CaP ceramics with a Ca/P ratio below 1 are too resorbable and cannot be used for implantable applications [4]. Furthermore, while CaP ceramics are generally regarded as osteoconductive in two-dimensional configurations, it has been found that they stimulate osteogenesis and are thus osteoinductive in some three-dimensional configurations [30].

The mechanical properties of HA render it unusable for load bearing applications. Its fracture toughness is significantly lower than other bioceramics (eg.  $\text{Al}_2\text{O}_3$ , YSZ) and cortical bone ( $< 1 \text{ MPa}\cdot\text{m}^{0.5}$  compared to  $2\text{-}10 \text{ MPa}\cdot\text{m}^{0.5}$ ) [4,13]. HA has been coated on metallic femoral stems to combine the mechanical properties of metallic implants with the bioactive surface properties of hydroxyapatite [4,32]. Plasma-spraying has been used to coat femoral stems with HA for over 20-years, but it has been found to have no benefit compared to uncoated femoral implant components in a systematic review [33]. It is

proposed that the unremarkable performance of HA coatings in early studies can be attributed to their thickness as a result of the coating technique. Plasma spraying produces relatively thick HA coatings (50-100 $\mu$ m), which results in poor coating adhesion, low interfacial shear strength, coating fragmentation and release *in-situ* [4,34]. To combat the processing problems associated with plasma spraying, low temperature processing methods are being investigated as an alternative towards the formation of thin, adherent calcium phosphate ceramic films such as sol-gel deposition, electrophoretic deposition, biomimetic deposition and electrochemical deposition [4,34,35].

#### **2.1.3.4 Bioactive Glasses**

Bioactive glasses are remarkable biomaterials because they are simultaneously osteoinductive, osteoconductive and resorbable [2,36,37]. These properties make them well-suited for regenerative medicine and tissue scaffold applications, since they will quickly regenerate new bone while resorbing over time [37]. Bioactive glass (specifically Bioglass® 45S5) was first discovered by Larry Hench in the late 1960s, and contained 46.1 mol% SiO<sub>2</sub>, 24.4% NaO, 26.9% CaO and 2.6% P<sub>2</sub>O<sub>5</sub> [38,39]. Hench's first bioactive glass was revolutionary because it was the first material able to bond with and promote formation of new calcified tissue [13]. The general mechanism of bonding in bioactive glass is as follows: first, exposure of the glass to physiological fluids promotes rapid corrosion and dissolution of alkali ions, which are replaced by H<sup>+</sup> or H<sub>3</sub>O<sup>+</sup> ions [36,37]. This results in a local pH increase, breaking of Si-O-Si bonds, and condensation polymerization of silanol (Si(OH)<sub>4</sub>) gel on the surface of the glass [36,37]. Ca ions and

$\text{PO}_4^{3-}$  groups diffuse towards the silanol and form an amorphous CaP layer, which gradually crystallizes and forms into carbonated HA due to incorporation of  $\text{CO}_3^{2-}$  and  $\text{OH}^-$  anions from physiological fluid [36,37].

Early bioactive glasses were unable to be used for tissue scaffolds since they were fabricated using high temperature techniques, and thus unable to introduce porosity, but in the 1990s Hench and his colleagues discovered that bioactive glass could be fabricated using the sol-gel method (named 58S Bioglass®) [38]. Fabrication of bioactive glass using the sol-gel method allowed for the fabrication of porous structures, such as tissue scaffolds, which was previously impossible using traditional melt-quench fabrication techniques [38]. Anti-bacterial bioactive glasses have also been fabricated, by doping the glass with Ag ions [40,41]. Bioactive glasses have been used clinically since the 1980s, but fewer products are available commercially compared to HA, due to FDA regulations on highly bioactive products [36]. The weak and brittle nature of bioactive glasses has limited their use in load bearing applications, but they can be used clinically if combined with polymers or metals to improve the mechanical strength and ductility [38]. Other limitations to widespread use of bioactive glass include the relatively fast resorption rate of bioactive glass has been found, in some cases, to outpace natural bone remodelling. This results in a gap at the bone/implant interface, which leads to implant detachment and failure. Finally, there are concerns about cytotoxicity due to the local pH increase as a result of initial alkali ion dissolution [37].

#### **2.1.4 Effect of Surface Properties on Osseointegration**

Initial attempts at surface modification of metallic implants focused on modifying the material composition to increase osseointegration, but more recently it was realized that surface properties also have a significant effect on implant success *in vivo* [42]. Surface morphology, roughness and wettability have been identified as key parameters that influence bonding at the bone tissue/implant interface [23,42,43]. In terms of surface morphology, there is robust evidence that surfaces containing topographical features on both the micro and nano scale (termed dual-scale topography) have enhanced bone growth and increased fixation at the bone tissue/implant interface [25,26,42–44]. Introduction of micro-scale surface features are hypothesized to increase mechanical interlocking between the implant and bone, due to increased surface area available for contact between the implant and osseous tissue [44]. Furthermore, incorporation of nanoscale features have been found to increase the rate of osseointegration by encouraging protein adsorption and migration of osteogenic cells [42,45]. This effect is believed to occur since nanoscale features mimic the natural environment encountered by cells *in vivo* [26,44]. An example of a surface with dual-scale topography can be found in Figure 2-2, which was fabricated using a two step process which combined 3D printing with electrochemical anodization [26].

In addition to dual scale morphology, surface wettability is an important parameter for predicting implant outcomes. Wettability is measured using contact angle measurements and surfaces with high blood wettability also increase the rate of osseointegration due to their enhanced adsorption and affinity towards proteins and cells

[23,42]. Average surface roughness ( $R_a$ ) is another important parameter, and an average roughness between 0.5 and 1.0  $\mu\text{m}$  has been found to be optimal for enhancing cell adhesion and proliferation [23].

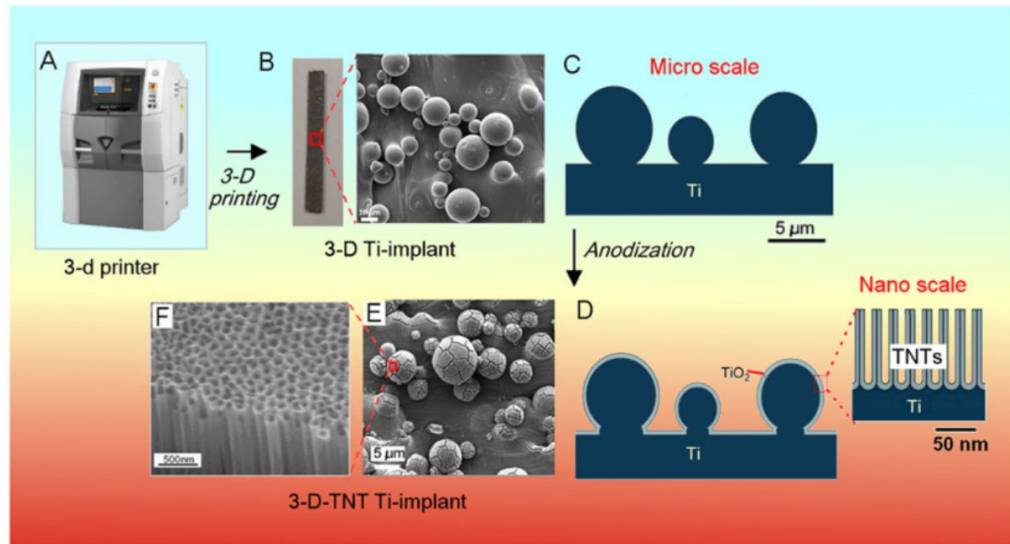


Figure 2-2: Schematic diagram illustrating dual-scale topography introduced in a two-step process. (A-C) Microscale features were introduced using 3D printing, and (F-D) nanoscale features were introduced using electrochemical anodization [26]. Copyright © 2017 WILEY-VCH Verlag GmbH & Co. KGaA, Weinheim

In summary, although many efforts have focused primarily on material composition when designing new implantable biomaterials, both surface topography *and* chemistry must be considered to enhance osseous tissue formation, implant fixation, and long-term outcomes.



## 2.2 Fundamentals of Electrophoretic Deposition

Electrophoretic deposition (EPD) is an increasingly popular and versatile coating fabrication technique. Advantages include: ability deposit a wide range of materials (e.g. ceramics, polymers, composites) on complex substrates, while providing control over coating thickness and microstructure, with simple equipment, for low cost in rapid fabrication time [46,47]. EPD can also be used to incorporate enzymes and proteins into composite coatings without damage, as it is a low temperature processing technique [48].

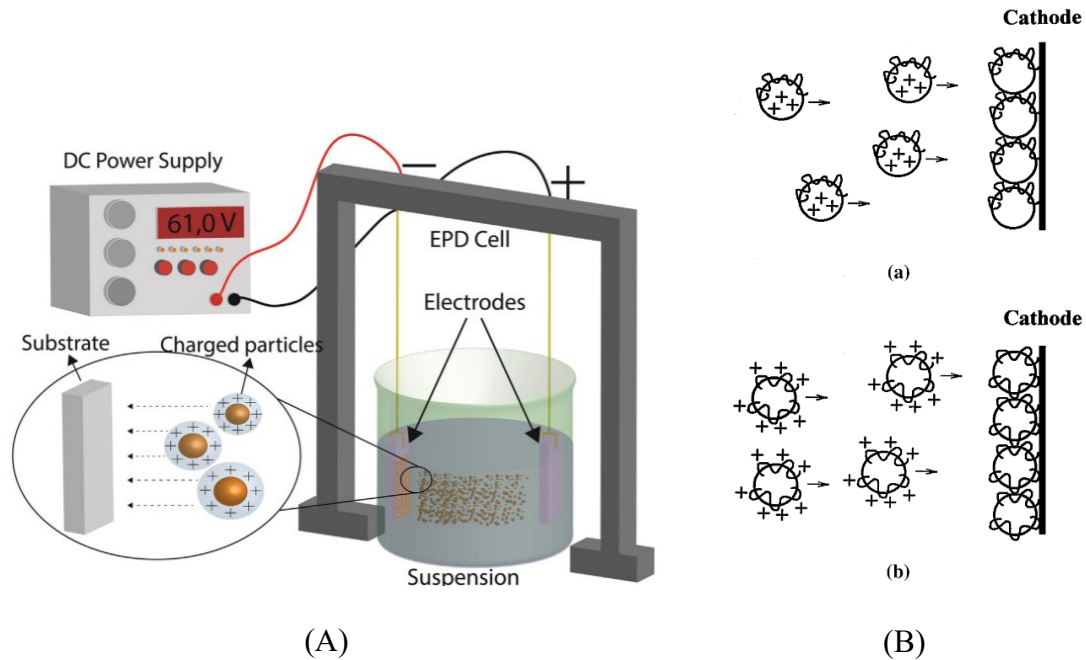


Figure 2-3: Schematic diagram of (A) cathodic EPD in a two-electrode cell [49] and (B) cathodic EPD using (a) charged particles and (b) charged molecules [50]. Figure (A) Copyright © 2019 Elsevier Science. Figure (B) Copyright © 2002 Elsevier Science B.V. All rights reserved.

The deposition mechanism of EPD is as follows: utilizing a two-electrode cell immersed within a colloidal suspension, an external electric field is applied to charged particles, which move towards the oppositely charged working electrode under the

influence of electric field (see Figure 2-3 A) [46,49,51,52]. The charged particles then coagulate to form a film on the electrode surface [46]. Only charged particles can be deposited using EPD [51], but uncharged particles can still be deposited using charged organic molecules or polymers (see Figure 2-3 B) [50]. Charged materials can be either anodically or cathodically deposited, depending on the charge of the particle or polymer in suspension [53]. It should also be noted that either DC or AC potential may be applied for EPD. Deposition with an AC potential is advantageous compared to DC potential deposition, as hydrolysis reactions and subsequent bubbling are prevented [52]. This is beneficial for situations where an aqueous suspension must be used [52].

EPD as a fabrication technique is of high interest for orthopaedic applications and biomedical applications in general, due to its ability to develop organic-inorganic coatings that mimic natural materials such as bone [46]. Of particular interest is the ability to fabricate hierarchical structures and incorporate biological macromolecules, such as nucleic acids, enzymes and proteins into composite coatings without damage because of the low temperature processing temperature [54].

EPD can be influenced by factors related to the suspension or by parameters related to processing [47,50]. Parameters related to the suspension include particle size, the dielectric constant and viscosity of the solvent, zeta potential, and electrical conductivity of the suspension. In general, to optimize parameters related to suspension stability particle size should be less than 20  $\mu\text{m}$ , and the ideal solvent should have low electrical conductivity, low viscosity and high dielectric constant [47]. Processing parameters that

can effect EPD are the applied voltage deposition time, solid concentration in the suspension and conductivity of the working electrode (substrate) [47].

### 2.2.1 Particle Interaction in a Colloid: DLVO Theory

To obtain homogenous deposition and thus final material properties, colloidal stability and agglomeration prevention are of paramount importance. The DLVO theory is the basis for developing our understanding of charged particle interactions in a colloid [50,55]. The DLVO theory was derived from Hamaker's original theory of colloidal stability, which calculated the potential energy of two particles as a function of interparticle distance [55,56]. Hamaker's theory considered that both attractive London-van der Waals and repulsive double-layer forces existed between two charged particles, but he incorrectly assumed a constant potential value for the electrical double-layer and that the double-layer contribution was repulsive at all interparticle distances [56]. The DLVO theory also uses potential energy curves, calculated using [50]:

$$V_T = V_A + V_R \quad (1)$$

Where  $V_T$  is the total energy of interaction between two separated, equivalently charged particles, and  $V_A$ , the attractive energy due to London-van der waals forces is [50]:

$$V_A = -\frac{A}{6} \left( \frac{2}{s^2-2} + \frac{2}{s^2} + \ln \frac{s^2-4}{s^2} \right) \quad (2)$$

Where the Hamaker constant is represented by  $A$ , and  $s$  is equal to [50]:

$$s = 2 + \frac{H}{a} \quad (3)$$

When the particle radius,  $a$ , is much larger than the shortest distance between the two spherical particles,  $H$ , then equation (2) becomes [50]:

$$V_A = -A \frac{a}{12H} \quad (4)$$

The energy of repulsion,  $V_R$ , attributed to the electrical double layer is equal to [50]:

$$V_R = 2\pi\epsilon\epsilon_o a \Psi^2 \ln(1 + e^{-\kappa H}) \quad (5)$$

Where the dielectric constant of the solvent is  $\epsilon$ , dielectric permittivity in vacuum is  $\epsilon_o$ , the surface potential is  $\Psi$  and the Debye-Huckel parameter is  $\kappa$ , or [50]:

$$\kappa = \left( \frac{e_o^2 \sum n_i z_i^2}{\epsilon\epsilon_o kT} \right)^{0.5} \quad (6)$$

Where charge of a single electron is  $e_o$ , the concentration of ions is  $n_i$ , the valence state of the ions is  $z_i$ , the Boltzmann constant is  $k$  and the temperature is  $T$  [50].

The advantage of the DLVO theory compared to Hamaker's original theory, is that it takes into consideration the effect of electrolyte ion valence and concentration, and thus varies the value of the electrical double layer potential, to more accurately predict stability of a colloidal suspension [47,50,56]. Using the potential energy curves (see Figure 2-4) derived from this theory, it was discovered that for low electrolyte concentration, the electrical double-layer thickness and potential increases, which results in greater contribution from the repulsive energy compared to the attractive London-van der Waals forces. This results in the formation of an energy barrier (Figure 2-4a), which prevents flocculation and results in a well-dispersed, stable colloid [47,50,56].

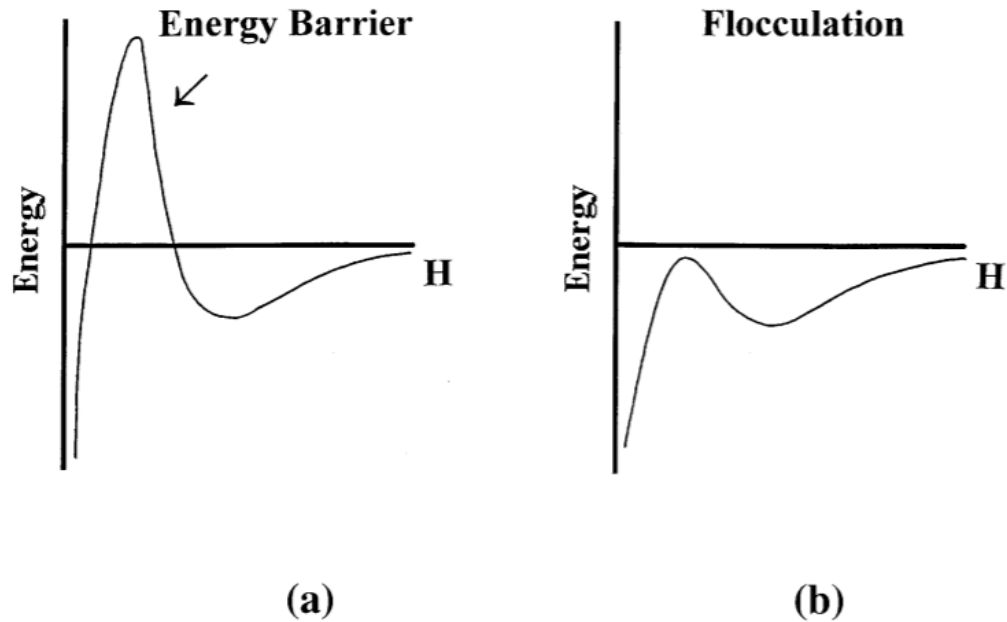


Figure 2-4: Potential energy curves as a function of interparticle distance,  $H$ , for (a) a stable colloidal suspension and a (b) unstable colloidal suspension containing flocculated particles [50]. Copyright © 2002 Elsevier Science B.V. All rights reserved.

For systems with high electrolyte concentrations, the thickness and electrical potential of the double-layer decreases, which results in greater potential energy contribution from the attractive London-van der Waals force. In this scenario, the energy barrier greatly decreases (see Figure 2-4b) and particles will flocculate as a result [47,50,56]. As such, the DLVO theory proposes that there exists a flocculation value—a critical value of electrolyte concentration, with opposite charge to that of the particles in the colloids, that will induce flocculation [50]. The flocculation value is both influenced by valence and ion size.

### **2.2.2 Limitations to DLVO Theory**

The DLVO theory has been critical for advances in electrodeposition-based fabrication techniques, since successful EPD is dependent on use of a stable colloidal precursor. Although the DLVO theory has proved to be a successful method for predicting colloidal stability [46], there have been discussions regarding its accuracy and limitations [50]. For example, one factor that affects the accuracy of the theory is that it is based on the assumption that the system is very dilute, with only two identical, isolated spheres interacting in the medium [50]. In addition, the DLVO theory does not account for the affect of organic macromolecules bonded or adsorbed on the particle surface. Macromolecule adsorption can greatly affect colloidal stability, either introducing an additional attractive or repulsive force [55]. Adsorbed charge-neutral macromolecules or polymers result in formation of a stable colloid, by offering a physical barrier between particles to prevent coagulation (see Figure 2-5b) [55]. This dispersion technique is called steric stabilization and can be achieved with relatively high concentrations of polymers. If the polymer concentration adsorbed on the particle surface is too low, coagulation will occur through a phenomenon known as “bridging flocculation”, which occurs when unoccupied sites for particle adsorption on the polymer bind with other unoccupied sites and form so-called bridges [55]. Electrosteric stabilization is another dispersion technique, which utilizes adsorption of a charged polymer or macromolecule to prevent particle flocculation and provide colloidal stability. The stabilization mechanism in this technique is two-fold: (i) the molecule acts as a physical barrier for coagulation and (ii) the charge

provides an electrostatic barrier through same-charge repulsion [55].

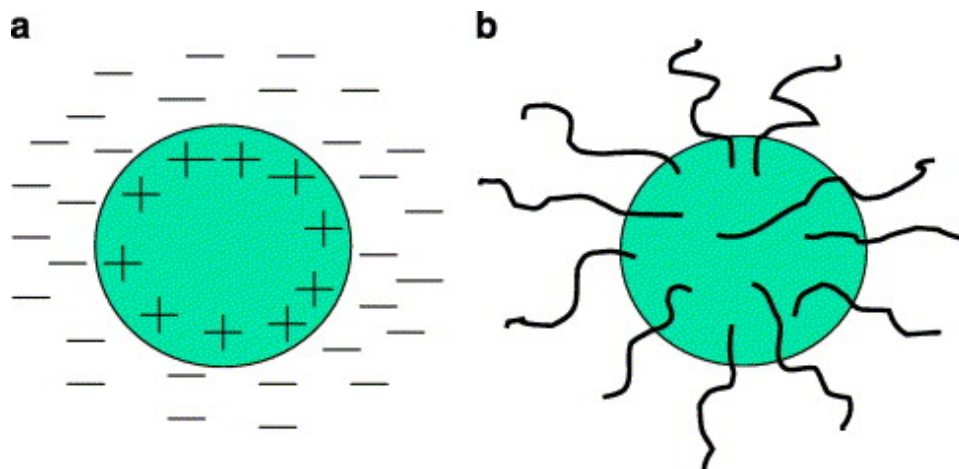


Figure 2-5: Schematic diagram of the various mechanisms of particle stabilization in a colloid, including (a) electrostatic stabilization and (b) steric stabilization [47]. Copyright © 2006 Elsevier Ltd. All rights reserved.

Dispersing agents that impart steric or electrosteric stabilization are advantageous for fabrication of organic-inorganic composite materials, since the organic component can serve multiple functions including acting as charging, dispersing and/or film-forming agents.

### 2.2.3 Particle Charging and Electrophoretic Mobility

When brought into contact with an aqueous or polar solvent, most inorganic particles and organic molecules become electrically charged [47]. Electrical charge develops on the surface of materials within a colloid by one of four different mechanisms: i) ion adsorption, ii) dissociation of functional groups, iii) cation exchange within the lattice or iv) polyelectrolyte adsorption [47,50,55]. Ion distribution within the polar solvent is influenced by the surface charge of a dispersed substance in a colloid [47], and is modeled using the widely accepted “diffuse double layer” (see Figure 2-6). The relationship between electrical potential,  $\psi$ , and distance from the Stern plane,  $x$ , can be approximated using [47]:

$$\psi = \psi_{\delta} \exp(-\kappa x) \quad (7)$$

Where  $\psi_{\delta}$  is equal to the electric potential at the interface of the Stern and diffuse layers and  $\kappa$  is the Debye-Huckel parameter (see equation (6)) [47].



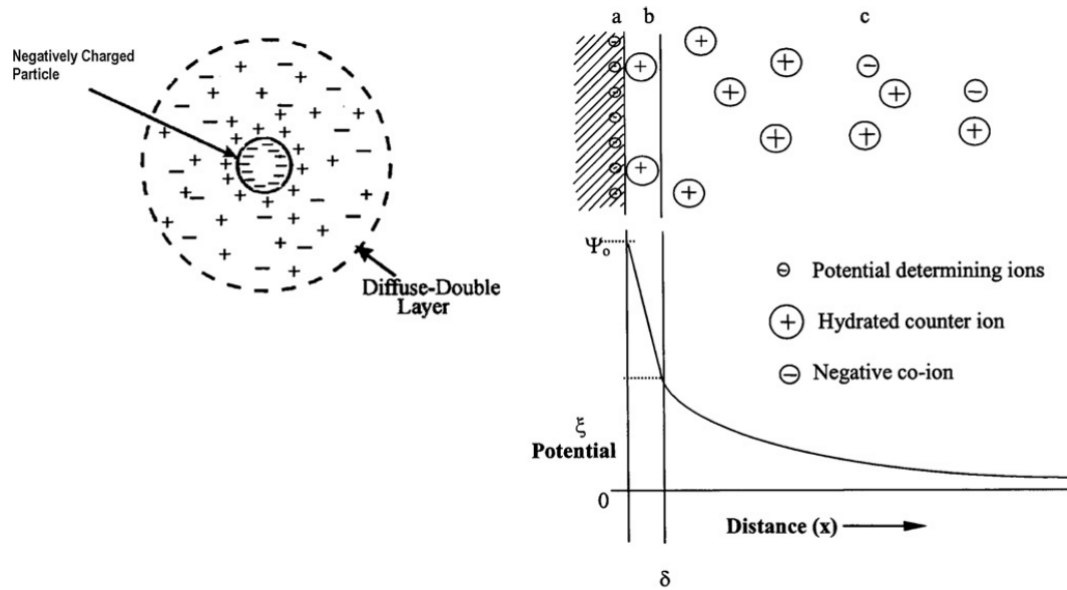


Figure 2-6: Schematic diagram of the diffuse or electrical double layer and electric potential as a function of distance, where (a) is the surface charge, (b) Stern layer and (c) diffuse-layer of oppositely charged ions [47]. Copyright © 2006 Elsevier Ltd. All rights reserved.

Zeta-potential is another important parameter related to colloidal stability, and is defined as the potential difference between the charge at the surface ( $\psi_0$ ) and the charge at the slip-plane, located between the Stern and diffuse layer ( $\psi_\delta$ ). Zeta-potential varies with pH (see Figure 2-7) if adsorbed  $H^+$  and  $OH^-$  are the charge determining ions [50]. As such, charged ceramic particles may be either cationic, anionic, or uncharged depending on the pH of the polar solvent [47,50].

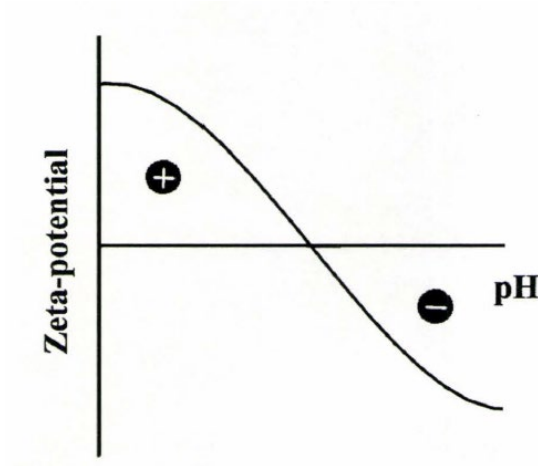


Figure 2-7: Zeta potential as a function of pH for charged ceramic particles dispersed in an aqueous medium [50]. Copyright © 2002 Elsevier Science B.V. All rights reserved.

Zeta-potential not only affects colloidal stability but also the electrophoretic mobility,  $\mu$ , of a rigid particle in suspension [47,50]. Electrophoretic mobility is calculated by dividing the particle velocity,  $v$ , by the strength of the applied electric field,  $E$  [47,50]:

$$\mu = \frac{v}{E} \quad (8)$$

And electrophoretic mobility is determined by [47,50]:

$$\mu = \frac{2}{3} \frac{\epsilon_o \epsilon_r \xi}{\eta} f(\kappa a) \quad (9)$$

Where vacuum permittivity is  $\epsilon_o$ , solvent permittivity is  $\epsilon_r$ , zeta potential is  $\xi$ , viscosity of the solvent is  $\eta$ , and the Henry coefficient is  $(\kappa a)$ , which is determined using electrical-double layer thickness and the radius of the rigid particle [47,50]. For particles that have a small double-layer thickness in comparison to their size, electrophoretic mobility is determined using the Smoluchowski equation [47,50]:

$$\mu = \frac{\epsilon_o \epsilon_r \xi}{\eta} \quad (10)$$

For particles with a thick double-layer compared to their size, electrophoretic mobility is determined using the Huckel equation [47,50]:

$$\mu = \frac{2\varepsilon_0\varepsilon_r\xi}{3\eta} \quad (11)$$

To model electrophoretic mobility of polyelectrolyte, a spherical shape and uniform charge distribution is assumed. Unlike a rigid particle, zeta-potential does not influence the electrophoretic mobility of a polyelectrolyte, since there is no well-defined slipping plane.

Mobility of a polyelectrolyte is modeled using the following equation [50]:

$$\mu = \frac{\rho_{fix}}{\eta\lambda^2} \left[ 1 + \frac{2}{3} \left( \frac{\lambda}{\kappa} \right)^2 \frac{1+\lambda/2\kappa}{1+\lambda/\kappa} \right] \quad (12)$$

Where  $\rho$  is the fixed, uniformly dense charge on the polyelectrolyte sphere,  $\lambda$  is a parameter that is influenced by both the frictional coefficient of the polyelectrolyte and the solvent viscosity, and is the Debye-Huckel parameter [47,50].

## 2.2.4 Deposition Yield and Mechanism of Deposition

Hamaker's law was the first theory that attempted to calculate the weight of deposited particles deposited on a substrate using EPD [46,47,50]. It proposed that the concentration of particles in the colloid,  $C$ , surface area of the working electrode,  $A$ , the electric field strength,  $E$ , and electrophoretic mobility,  $\mu$ , were all related to the final amount of material deposited on the electrode, represented using  $w$  [47]:

$$w = \int_{t_1}^{t_2} \mu E A C dt \quad (13)$$

This primary theory has been updated to account for true processing conditions [49]. One contemporary model has been developed by Biesheuvel and Verveij, and accounts for the

mass concentration of deposited particles ( $C_d$ ), as well as the volume concentration of particles both in the deposit ( $\phi_d$ ) and the suspension ( $\phi_s$ ) [47,49]:

$$w = \int_{t_1}^{t_2} \mu C_c \frac{\phi_c}{\phi_c - \phi_s} EA dt \quad (14)$$

EPD has been used with great success for the fabrication of a wide variety of materials, but still the precise mechanism of deposition is not known [47,50]. Hamaker and Verwey first theorized that deposition was a result of a similar mechanism to sediment formation due to the force of gravity [57]. They proposed that mutual repulsion of particles could be overcome with a sufficiently large applied electric field [57]. Later it was realized that this theory is not plausible, as it does not account for low applied electric field strength, which is typically used for electrodeposition [56]. Another theory proposed that deposition occurs due to flocculation as a result of electrode reactions and an increase in electrolyte concentration at the electrode surface [58]. This theory is only valid for deposition conditions which utilize an aqueous solvent and generate hydroxyl ions [47]. Finally, it was proposed that in situations where the electrolyte concentration did not increase near the electrode, deposition could be facilitated by considering distortion of the electrical double layer during electrophoresis [59]. This theory takes into account fluid mechanics, which would result in the double-layer becoming distorted to be wider behind the particle and thinner ahead of the particle during travel to the electrode surface [47]. The layer ahead of the particle would be sufficiently thin so that dominant force would be London-van der Waals and promote flocculation and coagulation at the electrode surface [47].

### **2.2.5 Biomimetic Dispersing Agents**

Dispersing agents are charged or uncharged organic molecules or polymers used to increase the overall stability of a colloid [60]. They are used widely for many applications in a variety of industries, including paint, personal cosmetics and household cleaners. Use of dispersing agents has been crucial to advances made in EPD processing over the last decade, but in recent years there has been increasing interest to discover new organic molecules that are capable of charging and dispersing many different inorganic particles or functional organic materials [61]. Development of new dispersants for biomedical applications can prove challenging, since many additional constraints must be considered compared to conventional applications, such as toxicity and biocompatibility. One approach looks to mother nature for inspiration and uses natural or biomimetic surfactants. Two such biomimetic dispersing agents are molecules from the catechol family, and bile acids and their salts. Utilizing a biomimetic approach is advantageous when designing new biomaterials, since the molecules often circumvent the restraints imposed during materials selection, and have interesting properties such as ultra-high adhesion or ability to self-assemble into intricate structures only found in nature.

#### **2.2.5.1 Catecholic Molecules**

Catecholic molecules naturally occurring phenolic compounds, abundant across both the plant and animal kingdoms [62]. They are characterized by a molecular structure that contains a benzene ring with two adjacent hydroxyl groups attached (see Figure 2-8A). Catecholic molecules play an important role in physiological and biological processes

[61,62]. For example, neurotransmitters epinephrine (adrenaline) and dopamine are catecholamines, both of which are crucial for proper functioning of the human brain [61]. Melanin is another molecule from the catechol family, that gives human hair and skin its pigment [63]. Catechol-containing moieties are also found abundantly found in plant-based food and drink, and aid in human health by acting as dietary antioxidants [64]. Perhaps the most famous catecholic molecule is L-3,4-dihydroxyphenylalanine (L-DOPA), which has gained widespread recognition for its role in the marine mussels ability to exhibit the strongest interfacial adhesion found in nature, even in aggressive marine conditions [65].

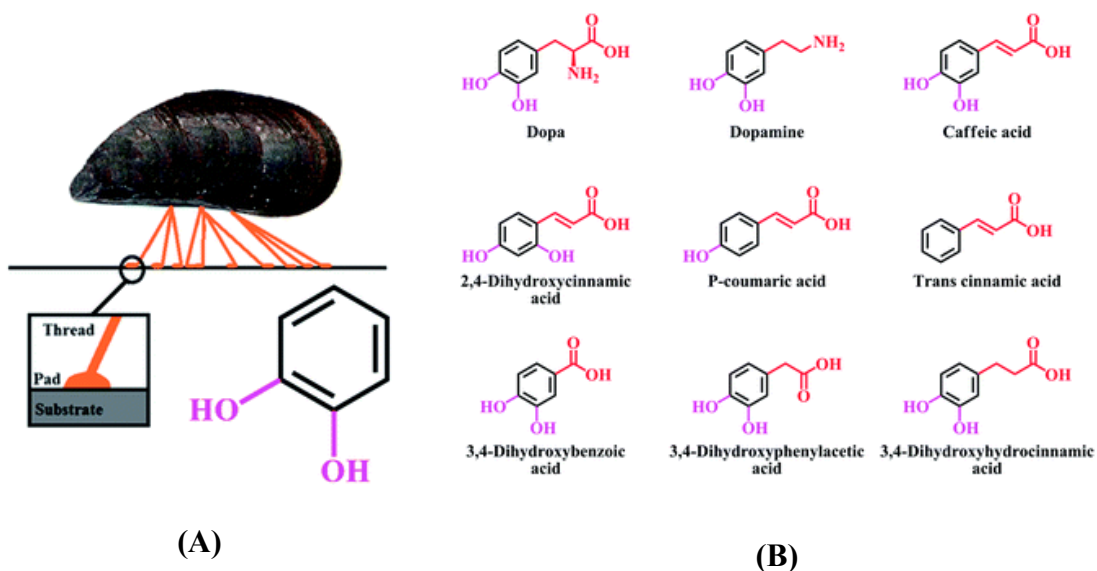


Figure 2-8: Chemical structure of catechol molecule and diagram of mechanism of mussel surface adhesion. (B) chemical structures of catechol-family molecules. Reproduced from Ref. 61 with permission from The Royal Society of Chemistry.

When developing novel dispersing agents, adhesion to the metal oxide particle surface is of paramount importance for stable colloidal precursors and efficient deposition [61]. Ionic dispersing agents that are not adsorbed to the surface will act as electrolyte,

which will decrease the electrical double layer thickness and result in colloidal instability and agglomeration [61]. Due to catechols remarkable adhesion and stability across a wide pH range, as well as its ability to form complexes with metal ions, many molecules from the catechol family (see Figure 2-8B) are being explored for use as dual charging and dispersing agents for MOx particles [61]. There are three different proposed mechanisms of adsorption of catecholic molecules on a MOx particle surface (see figure 2-9A), which involve bonding between the particle and phenolic functional groups [61]. Other functional groups may play a role in adsorption [61]. For example, caffeic acid, a molecule in the catechol family, may bond by one of the three phenolic configurations: bidentate chelating, or inner sphere or outer sphere bidentate bridging (see Figure 2-9A a-c). The MOx particle may also bond to the carboxyl group (see Figure 2-9A d) [61]. Furthermore, catecholic molecules not only show increased adhesion to inorganic surfaces, but also organic surfaces and animal tissue [66,67]. For example, they have been shown to increase stability and decrease long-term degradation of polysaccharide hydrogels, such as CHIT and ALG in aqueous or physiological environments [68,69].

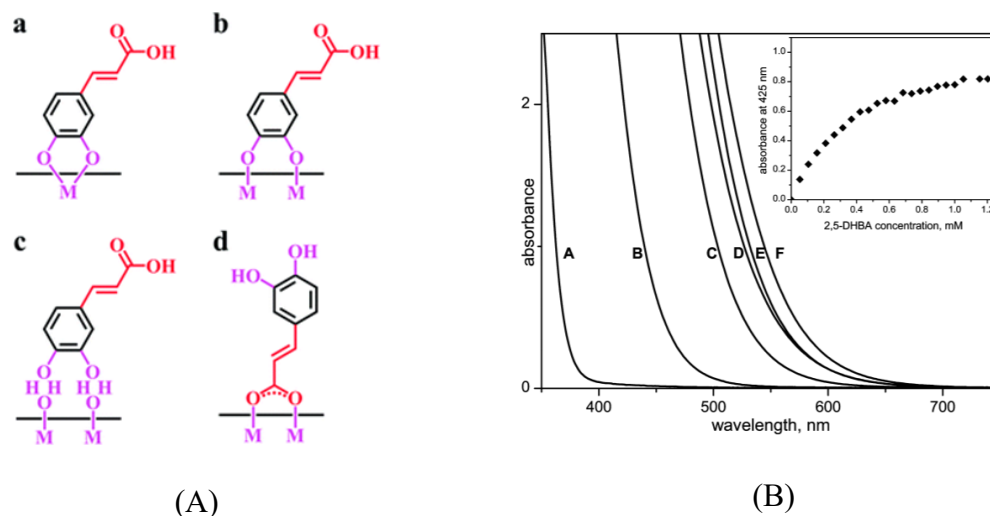


Figure 2-9: (A) Schematic diagram of various configurations of catecholic bonding with metal oxides, including (a) chelating, (b) inner sphere bridging, (c) outer sphere bridging and (d) carboxylic adsorption, using caffeic acid as a model catecholic molecule. Reproduced from Ref. 61 with permission from The Royal Society of Chemistry. (B) UV-vis spectra of unmodified TiO<sub>2</sub> nanoparticles (A) compared to catechol-modified TiO<sub>2</sub> nanoparticles (B-F), indicating absorption spectra shifting to longer wavelengths [70]. Copyright © 2009, American Chemical Society.

In addition to exhibiting robust adhesion, molecules in the catechol family have other unique properties, such as pseudo-capacitance, which can be utilized to create materials for environmental, energy storage and electrochemical sensing applications [62,66,71]. Finally, the possibility of electronic structure modification of MOx particles has been discovered using molecules from the catechol family [72,73]. Jankovic et al. compared TiO<sub>2</sub> nanoparticles modified with pure catechol and four other different molecules from the catechol family, and found that while it did not make a significant difference in the band gap energy, it did alter its absorption spectra when measured using UV-vis spectroscopy (see Figure 2-9B) [70]. Shifting adsorption of TiO<sub>2</sub> nanoparticles



from the ultra-violet towards the visible has use in many important applications, such as photovoltaics with increased efficiency.

### **2.2.5.2 Catechol-Modified Polysaccharides**

In the same way that information is processed, and operations are performed through the transfer of chemicals ions in biology, electronic devices receive information and convert it to energy with electrons [74]. There is potential to couple biology with electronic devices for applications such as enzymatic fuel cells or biosensors, but currently electrons cannot transduce chemical information released from biological systems [74]. Pseudo-capacitors (also known as redox-capacitors) store energy through reversible redox reactions, and can be used to transduce energy and process signals [74]. The redox activity of biological materials has been investigated in recent years with hopes of establishing bio-device pairing [71,74]. Naturally-occurring catechol-modified polysaccharide films have been fabricated, and have been found to be redox-active but non-conducting [74]. Although these films are non-conductive, they are capable of electron storage, donation, and acceptance. They also facilitate electron flow in a mechanism similar to electron transfer reactions in biology: through intermediate steps [75]. This is distinctly different from the mechanism of electron flow in metallic and conductive materials, in which valence electrons flow due to their existence in a delocalized “sea”. This unique behaviour allows for direct signal conversion of a biological event into an electrical signal [76].

To enable the detection of low concentrations of biological analyte using electrochemical sensing techniques, signal transduction must be amplified, for which both redox and nanoparticle-based techniques have been employed [59]. Naturally occurring phenolic molecules, such as catechol and galloyl, have been found to have unique redox properties which may be utilized for the development of novel hydrogel films for electrochemical biosensing [57,60]. CAT-functionalization of CHIT, a polysaccharide derived from the exoskeleton of crustaceans, resulted in imparting redox-capacitive behaviour to the non-conductive polymeric film [56,57,61]. CAT-CHIT films have been used for electrochemical monitoring of *p*-aminophenol [59], bacterial metabolites such as pyocyanin (PYO) [75], and the antipsychotic clozapine, utilizing redox-based amplification of peak currents in the presence of analyte [68]. In addition to being used for voltammetric based sensing, CAT-CHIT films may also be used for photoelectrochemical detection of biological analytes, due to catecholic molecules ability to modify the electronic properties of semiconducting particles [73].

Polysaccharide monomers may be functionalized with catechol groups using chemical, enzymatic, or electrochemical synthesis techniques [68]. Electrochemical synthesis techniques, including EPD are advantageous for catechol functionalization of polysaccharides, compared to other methods, because of the aforementioned benefits described in section 2.2. A schematic diagram of the current electrochemical modification technique, for the modification of CHIT, can be found in Figure 2-10. This method utilizes a two-step technique, in which CHIT is first deposited using cathodic EPD, followed by anodic grafting of the CAT molecule [68,75,76]. Although this technique has allowed for

successful fabrication of CAT-CHIT, it could be improved by removing the anodic grafting step, since during anodic deposition changes in the local pH create conditions for dissolution of the underlying CHIT film.

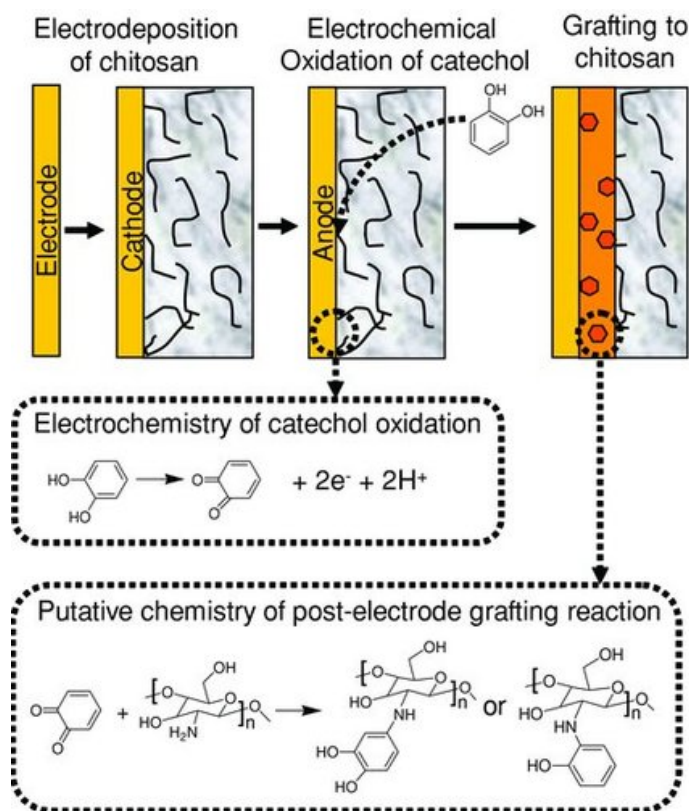


Figure 2-10: Current electrochemical method for catechol functionalization of chitosan [71]. Copyright © 2010 WILEY-VCH Verlag GmbH & Co. KGaA, Weinheim

### 2.2.5.3 Bile Acids and Bile Acid Salts

Bile acids and their salts are naturally occurring anionic surfactants found in human bile that are used in the mammalian digestive system to solubilize fatty acids, fat soluble vitamins and lipids [77]. Their solubilization ability is remarkable, and it has been reported

that they can solubilize hydrophobic molecules, such as cholesterol, over one million times [78]. Bile acids and their salts self-assemble to form porous gel networks [79]. Bile acid salts, in particular, easily become anionic via dissociation of the COOH group when dissolved in water. As such, they have been used as charging and dispersing agents for the dispersion and fabrication of composite gel films, containing multi-walled carbon nanotubes (MWCNTs) [80].

The steroid backbone of bile salt surfactants allows for a unique amphiphilic chemical structure, that contains a hydrophobic concave side and a hydrophilic convex side [81,82]. This structure is vastly different from traditional head-tail surfactants and allows for dispersion of functional materials without disrupting their intrinsic properties. For example, bile acid salts preserve the conductivity of MWCNTs by forming a ring around MWCNTs in suspension, without creating an insulating layer or damaging the  $sp^2$  carbon-carbon bond [81,82]. In addition to dispersing high concentrations of MWCNTs, bile salts are able to separate individual nanotubes from MWCNT bundles without damage to the structure [77,82].

Based on the success of bile acid salts for the dispersion and fabrication of composite films with MWCNTs, they are of high interest for use as charging, dispersing and film-forming agents for other hydrophobic molecules. For biomedical applications, use of these powerful natural surfactants is of particular interest for fabrication of composite gels, containing drugs for the fabrication of anti-bacterial coatings to prevent post-operative infection.

## 2.3 Research Objectives

Based on review of the literature provided above, the overarching objective of this work is to fabricate novel multi-component biomedical materials, while utilizing biomimetic materials and inspiration, that may serve multiple functions: for example, organic-inorganic nanocomposite films that may act as either a biomedical implant coating, or as an electrochemical biosensor. Within this overarching long-term objective, the following short-term objectives of this work have been formulated and can be summarized as follows:

1. Development of new colloidal and electrochemical processing techniques for the fabrication of multi-functional coatings for biomedical applications
2. Fabrication of biomimetic organic-inorganic nanocomposite coatings with topographical features across multiple length scales for increased osseointegration
3. Design of advanced synthesis methods that prevent agglomeration and control the size of inorganic nanoparticles
4. Facile catechol functionalization of biopolymers and polymeric hydrogels for the fabrication of novel biomaterials for both orthopaedic and electrochemical sensing applications
5. Development of advanced solubilization and deposition methods for commercially available water-insoluble drugs for the fabrication of drug-containing coatings to prevent surgical infection

## 2.4 References

- [1] J. Moritz, A. Abram, M. Čekada, U. Gabor, M. Garvas, I. Zdovc, A. Daksobler, J. Cotič, K. Ivičak-Kocjan, A. Kocjan, Nanoroughening of sandblasted 3Y-TZP surface by alumina coating deposition for improved osseointegration and bacteria reduction, *J. Eur. Ceram. Soc.* 39 (2019) 4347–4357.  
doi:10.1016/j.jeurceramsoc.2019.05.051.
- [2] X. Fan, B. Feng, Z. Liu, J. Tan, W. Zhi, X. Lu, J. Wang, J. Weng, Fabrication of TiO<sub>2</sub> nanotubes on porous titanium scaffold and biocompatibility evaluation in vitro and in vivo, *J. Biomed. Mater. Res. - Part A*. 100 A (2012) 3422–3427.  
doi:10.1002/jbm.a.34268.
- [3] T. Albrektsson, C. Johansson, Osteoinduction, osteoconduction and osseointegration, *Eur. Spine J.* 10 (2001) S96–S101. doi:10.1007/s005860100282.
- [4] S.M. Best, A.E. Porter, E.S. Thian, J. Huang, Bioceramics: Past, present and for the future, *J. Eur. Ceram. Soc.* 28 (2008) 1319–1327.  
doi:10.1016/j.jeurceramsoc.2007.12.001.
- [5] L. Rony, P. de Sainte Hermine, V. Steiger, R. Mallet, L. Hubert, D. Chappard, Characterization of wear debris released from alumina-on-alumina hip prostheses: Analysis of retrieved femoral heads and peri-prosthetic tissues, *Micron*. 104 (2018) 89–94. doi:10.1016/j.micron.2017.11.002.
- [6] B. Ben-Nissan, A.H. Choi, R. Cordingley, Alumina Ceramics, in: *Bioceram. Their Clin. Appl.*, Woodhead Publishing and Maney Publishing, 2008: pp. 223–242.
- [7] F.A. Shah, P. Thomsen, A. Palmquist, Osseointegration and current interpretations of the bone-implant interface, *Acta Biomater.* 84 (2019) 1–15.  
doi:10.1016/j.actbio.2018.11.018.
- [8] K. Grandfield, S. Gustafsson, A. Palmquist, Where bone meets implant: The characterization of nano-osseointegration, *Nanoscale*. 5 (2013) 4302–4308.  
doi:10.1039/c3nr00826f.
- [9] M. Aslam, F. Ahmad, P.S.M.B.M. Yusoff, K. Altaf, M.A. Omar, R.M. German, Powder injection molding of biocompatible stainless steel biodevices, *Powder*

- Technol. 295 (2016) 84–95. doi:10.1016/j.powtec.2016.03.039.
- [10] M. Talha, Y. Ma, Y. Lin, Y. Pan, X. Kong, O.P. Sinha, C.K. Behera, Corrosion performance of cold deformed austenitic stainless steels for biomedical applications, *Corros. Rev.* 0 (2019). doi:10.1515/correv-2019-0004.
- [11] N.K. Awad, S.L. Edwards, Y.S. Morsi, A review of TiO<sub>2</sub> NTs on Ti metal: Electrochemical synthesis, functionalization and potential use as bone implants, *Mater. Sci. Eng. C.* 76 (2017) 1401–1412. doi:10.1016/j.msec.2017.02.150.
- [12] M. Talha, C.K. Behera, O.P. Sinha, A review on nickel-free nitrogen containing austenitic stainless steels for biomedical applications, *Mater. Sci. Eng. C.* 33 (2013) 3563–3575. doi:10.1016/j.msec.2013.06.002.
- [13] M.Z. Ibrahim, A.A.D. Sarhan, F. Yusuf, M. Hamdi, Biomedical materials and techniques to improve the tribological, mechanical and biomedical properties of orthopedic implants – A review article, *J. Alloys Compd.* 714 (2017) 636–667. doi:10.1016/j.jallcom.2017.04.231.
- [14] N.S. Manam, W.S.W. Harun, D.N.A. Shri, S.A.C. Ghani, T. Kurniawan, M.H. Ismail, M.H.I. Ibrahim, Study of corrosion in biocompatible metals for implants: A review, *J. Alloys Compd.* 701 (2017) 698–715. doi:10.1016/j.jallcom.2017.01.196.
- [15] Q. Chen, G.A. Thouas, Metallic implant biomaterials, *Mater. Sci. Eng. R Reports.* 87 (2015) 1–57. doi:10.1016/j.mser.2014.10.001.
- [16] S. Wu, S. Wang, W. Liu, X. Yu, G. Wang, Z. Chang, D. Wen, Microstructure and properties of TiO<sub>2</sub> nanotube coatings on bone plate surface fabrication by anodic oxidation, *Surf. Coatings Technol.* 374 (2019) 362–373. doi:10.1016/j.surfcoat.2019.06.019.
- [17] B.J. Mcentire, B.S. Bal, M.N. Rahaman, J. Chevalier, G. Pezzotti, Journal of the European Ceramic Society Ceramics and ceramic coatings in orthopaedics, *J. Eur. Ceram. Soc.* 35 (2015) 4327–4369. doi:10.1016/j.jeurceramsoc.2015.07.034.
- [18] J. Chevalier, L. Gremillard, Zirconia Ceramics, in: *Bioceram. Their Clin. Appl.*, Woodhead Publishing and Maney Publishing, 2008: pp. 243–265.
- [19] M.C. Aragón-Duarte, A. Nevarez-Rascón, H.E. Esparza-Ponce, M.M. Nevarez-

- Rascón, R.P. Talamantes, C. Ornelas, J. Mendez-Nonell, J. González-Hernández, M.J. Yacamán, A. Hurtado-Macías, Nanomechanical properties of zirconia- yttria and alumina zirconia- yttria biomedical ceramics, subjected to low temperature aging, *Ceram. Int.* 43 (2017) 3931–3939. doi:10.1016/j.ceramint.2016.12.033.
- [20] M. V Swain, L.E. He, Mechanical properties of Bioceramics, in: *Bioceram. Their Clin. Appl.*, Woodhead Publishing and Maney Publishing, 2008: pp. 78–105.
- [21] G.C. Lee, R.H. Kim, Incidence of Modern Alumina Ceramic and Alumina Matrix Composite Femoral Head Failures in Nearly 6 Million Hip Implants, *J. Arthroplasty.* 32 (2017) 546–551. doi:10.1016/j.arth.2016.08.011.
- [22] K. Almas, What is the Best Micro and Macro Dental Implant Topography?, 63 (2019) 447–460. doi:10.1016/j.cden.2019.02.010.
- [23] C.N. Elias, Y. Oshida, J.H.C. Lima, C.A. Muller, Relationship between surface properties (roughness, wettability and morphology) of titanium and dental implant removal torque, *J. Mech. Behav. Biomed. Mater.* 1 (2008) 234–242. doi:10.1016/j.jmbbm.2007.12.002.
- [24] N. Drnovšek, K. Rade, R. Milačič, J. Štrancar, S. Novak, The properties of bioactive TiO<sub>2</sub> coatings on Ti-based implants, *Surf. Coatings Technol.* 209 (2012) 177–183. doi:10.1016/j.surfcoat.2012.08.037.
- [25] B.E.J. Lee, H. Exir, A. Weck, K. Grandfield, Characterization and evaluation of femtosecond laser-induced sub-micron periodic structures generated on titanium to improve osseointegration of implants, *Appl. Surf. Sci.* 441 (2018) 1034–1042. doi:10.1016/j.apsusc.2018.02.119.
- [26] K. Gulati, M. Prideaux, M. Kogawa, L. Lima-Marques, G.J. Atkins, D.M. Findlay, D. Losic, Anodized 3D–printed titanium implants with dual micro- and nano-scale topography promote interaction with human osteoblasts and osteocyte-like cells, *J. Tissue Eng. Regen. Med.* 11 (2017) 3313–3325. doi:10.1002/term.2239.
- [27] X.B. Hangzhou Zhang, Yu Sun, Ang Tian, Xiang Xin Xue, Lin Wang, Ali Alquhali, Improved antibacterial activity and biocompatibility on vancomycin-loaded TiO<sub>2</sub> nanotubes: in vivo and in vitro studies, *Int. J. Nanomedicine.* 8 (2013)



4379–4389.

- [28] U.F. Gunpath, H. Le, R.D. Handy, C. Tredwin, Anodised TiO<sub>2</sub> nanotubes as a scaffold for antibacterial silver nanoparticles on titanium implants, *Mater. Sci. Eng. C*. 91 (2018) 638–644. doi:10.1016/j.msec.2018.05.074.
- [29] Y. Takana, K. Yamashita, Fabrication processes for bioceramics, in: *Bioceram. Their Clin. Appl.*, Woodhead Publishing and Maney Publishing, 2008: pp. 28–52.
- [30] H. Oonishi, H.J. Oonishi, S.C. Kim, L.L. Hench, J. Wilson, E. Tsuji, H. Fujita, H. Oohashi, K. Oomamiuda, Clinical Applications of Hydroxyapatite, in: *Bioceram. Their Clin. Appl.*, Woodhead Publishing and Maney Publishing, 2008: pp. 606–687.
- [31] R.G. Carrodeguas, S. De Aza,  $\alpha$ -Tricalcium phosphate: Synthesis, properties and biomedical applications, *Acta Biomater.* 7 (2011) 3536–3546. doi:10.1016/j.actbio.2011.06.019.
- [32] E.C.S. Rigo, A.O. Boschi, M. Yoshimoto, S.A. Jr, B.K. Jr, M.J. Carbonari, Evaluation in vitro and in vivo of biomimetic hydroxyapatite coated on titanium dental implants, 24 (2004) 647–651. doi:10.1016/j.msec.2004.08.044.
- [33] J.H.M. Goosen, A.J. Kums, B.J. Kollen, C.C.P.M. Verheyen, Porous-coated femoral components with or without hydroxyapatite in primary uncemented total hip arthroplasty: A systematic review of randomized controlled trials, *Arch. Orthop. Trauma Surg.* 129 (2009) 1165–1169. doi:10.1007/s00402-008-0749-9.
- [34] S.C.G. Leeuwenburgh, J.G.C. Wolke, J.A. Jansen, K. De Groot, Calcium Phosphate Coatings, in: *Bioceram. Their Clin. Appl.*, Woodhead Publishing and Maney Publishing, 2008: pp. 464–484.
- [35] S.B. Goodman, Z. Yao, M. Keeney, F. Yang, The future of biologic coatings for orthopaedic implants, *Biomaterials*. 34 (2013) 3174–3183. doi:10.1016/j.biomaterials.2013.01.074.
- [36] J.R. Jones, Bioactive Glass, in: *Bioceram. Their Clin. Appl.*, Woodhead Publishing and Maney Publishing, 2008: pp. 266–283.
- [37] H.R. Fernandes, A. Gaddam, A. Rebelo, D. Brazete, G.E. Stan, J.M.F. Ferreira,

- Bioactive glasses and glass-ceramics for healthcare applications in bone regeneration and tissue engineering, *Materials* (Basel). 11 (2018) 1–54. doi:10.3390/ma11122530.
- [38] L.L. Hench, The story of Bioglass, (2006) 967–978. doi:10.1007/s10856-006-0432-z.
- [39] V. Krishnan, T. Lakshmi, Bioglass: A novel biocompatible innovation, *J. Adv. Pharm. Technol. Res.* 4 (2013) 78–83. doi:10.4103/2231-4040.111523.
- [40] D.. Clupper, L.L. Hench, Bioactive response of Ag-doped tape cast Bioglass® 45S5 following heat treatment, *J. Mater. Sci. Mater. Med.* 12 (2001) 917–921. doi:10.1023/A:1012836426866.
- [41] C.R. Mariappan, N. Ranga, Influence of silver on the structure, dielectric and antibacterial effect of silver doped bioglass-ceramic nanoparticles, *Ceram. Int.* 43 (2017) 2196–2201. doi:10.1016/j.ceramint.2016.11.003.
- [42] J.C.M. Souza, M.B. Sordi, M. Kanazawa, S. Ravindran, B. Henriques, F.S. Silva, C. Aparicio, L.F. Cooper, Nano-scale modification of titanium implant surfaces to enhance osseointegration, *Acta Biomater.* 94 (2019) 112–131. doi:10.1016/j.actbio.2019.05.045.
- [43] D.M. Dohan Ehrenfest, P.G. Coelho, B.S. Kang, Y.T. Sul, T. Albrektsson, Classification of osseointegrated implant surfaces: Materials, chemistry and topography, *Trends Biotechnol.* 28 (2010) 198–206. doi:10.1016/j.tibtech.2009.12.003.
- [44] G. Mendonça, D.B.S. Mendonça, F.J.L. Aragão, L.F. Cooper, Advancing dental implant surface technology - From micron- to nanotopography, *Biomaterials.* 29 (2008) 3822–3835. doi:10.1016/j.biomaterials.2008.05.012.
- [45] R. Garimella, A.E.M. Eltorai, Nanotechnology in orthopedics, *J. Orthop.* 14 (2017) 30–33. doi:10.1016/j.jor.2016.10.026.
- [46] A.R. Boccaccini, S. Keim, R. Ma, Y. Li, I. Zhitomirsky, Electrophoretic deposition of biomaterials, *J. R. Soc. Interface.* 7 (2010) S581–S613. doi:10.1098/rsif.2010.0156.focus.

- [47] L. Besra, M. Liu, A review on fundamentals and applications of electrophoretic deposition (EPD), *Prog. Mater. Sci.* 52 (2007) 1–61.  
doi:10.1016/j.pmatsci.2006.07.001.
- [48] A. Clifford, D. Luo, I. Zhitomirsky, Colloidal strategies for electrophoretic deposition of organic-inorganic composites for biomedical applications, *Colloids Surfaces A Physicochem. Eng. Asp.* 516 (2017).  
doi:10.1016/j.colsurfa.2016.12.039.
- [49] E. Avcu, F.E. Baştan, H.Z. Abdullah, M.A.U. Rehman, Y.Y. Avcu, A.R. Boccaccini, Electrophoretic deposition of chitosan-based composite coatings for biomedical applications: A review, *Prog. Mater. Sci.* 103 (2019) 69–108.  
doi:10.1016/j.pmatsci.2019.01.001.
- [50] I. Zhitomirsky, Cathodic electrodeposition of ceramic and organoceramic materials. Fundamental aspects, *Adv. Colloid Interface Sci.* 97 (2002) 279–317.  
doi:10.1016/S0001-8686(01)00068-9.
- [51] O.O. Van der Biest, L.J. Vandeperre, ELECTROPHORETIC DEPOSITION OF MATERIALS, *Annu. Rev. Mater. Sci.* 1999 (1999) 327–352. doi:10.1016/S0958-2118(02)80166-5.
- [52] S. Seuss, M. Lehmann, A.R. Boccaccini, Alternating current electrophoretic deposition of antibacterial bioactive Glass-Chitosan composite coatings, *Int. J. Mol. Sci.* 15 (2014) 12231–12242. doi:10.3390/ijms150712231.
- [53] I. Zhitomirsky, Electrophoretic deposition of organic-inorganic nanocomposites, *J. Mater. Sci.* 41 (2006) 8186–8195. doi:10.1007/s10853-006-0994-7.
- [54] S. Seuss, A.R. Boccaccini, Electrophoretic deposition of biological macromolecules, drugs, and cells, *Biomacromolecules.* 14 (2013) 3355–3369.  
doi:10.1021/bm401021b.
- [55] M.N. Rahaman, *Ceramic Processing*, 2006.
- [56] E.J.W. Verwey, Theory of the stability of lyophobic colloids, *J. Phys. Colloid Chem.* 51 (1947) 631–636. doi:10.1021/j150453a001.
- [57] H. Hamaker, E.J.W. Verwey, The Role of the forces between the particles in

- electrodeposition and other phenomena, *Trans. Faraday Soc.* 36 (1940) 180–185.
- [58] H. Koelmans, J.T.G. Overbeek, Stability and electrophoretic deposition of suspensions in a non-aqueous media, *Discuss. Faraday Soc.* 18 (1954).
- [59] P. Sarkar, P.S. Nicholson, Electrophoretic deposition (EPD): mechanisms, kinetics and application to ceramics, *J. Am. Ceram. Soc.* 79 (1996) 1987–2002.
- [60] F.O.H. Pirrung, P.H. Quednau, C. Auschra, Wetting and dispersing agents, *Chimia (Aarau)*. 56 (2002) 170–176. doi:10.2533/000942902777680496.
- [61] M.S. Ata, Y. Liu, I. Zhitomirsky, A review of new methods of surface chemical modification, dispersion and electrophoretic deposition of metal oxide particles, *RSC Adv.* 4 (2014) 22716–22732. doi:10.1039/c4ra02218a.
- [62] N. Patil, C. Jérôme, C. Detrembleur, Recent advances in the synthesis of catechol-derived (bio)polymers for applications in energy storage and environment, *Prog. Polym. Sci.* 82 (2018) 34–91. doi:10.1016/j.progpolymsci.2018.04.002.
- [63] E. Kim, Y. Liu, W.T. Leverage, J.J. Yin, I.M. White, W.E. Bentley, G.F. Payne, Context-dependent redox properties of natural phenolic materials, *Biomacromolecules*. 15 (2014) 1653–1662. doi:10.1021/bm500026x.
- [64] Á. Valero-Navarro, M. Gómez-Romero, J.F. Fernández-Sánchez, P.A.G. Cormack, A. Segura-Carretero, A. Fernández-Gutiérrez, Synthesis of caffeic acid molecularly imprinted polymer microspheres and high-performance liquid chromatography evaluation of their sorption properties, *J. Chromatogr. A*. 1218 (2011) 7289–7296. doi:10.1016/j.chroma.2011.08.043.
- [65] J. Hwang, Y. Jeong, J.M. Park, K.H. Lee, J.W. Hong, J. Choi, Biomimetics: Forecasting the future of science, engineering, and medicine, *Int. J. Nanomedicine*. 10 (2015) 5701–5713. doi:10.2147/IJN.S83642.
- [66] S. Moulay, Dopa/catechol-tethered polymers: Dioadhesives and biomimetic adhesive materials, *Polym. Rev.* 54 (2014) 436–513. doi:10.1080/15583724.2014.881373.
- [67] K. Kim, K. Kim, J.H. Ryu, H. Lee, Chitosan-catechol: A polymer with long-lasting mucoadhesive properties, *Biomaterials*. 52 (2015) 161–170.

- doi:10.1016/j.biomaterials.2015.02.010.
- [68] J.H. Ryu, S. Hong, H. Lee, Bio-inspired adhesive catechol-conjugated chitosan for biomedical applications: A mini review, *Acta Biomater.* 27 (2015) 101–115. doi:10.1016/j.actbio.2015.08.043.
  - [69] H. Hong, J.H. Ryu, H. Lee, Effect of charge on in vivo adhesion stability of catechol-conjugated polysaccharides, *J. Ind. Eng. Chem.* In Press (2019). doi:doi.org/10.2016/j.jiec.2019.07.017.
  - [70] I. a. Janković, Z. V. Šaponjić, M.I. Čomor, J.M. Nedeljković, Surface Modification of Colloidal TiO<sub>2</sub> Nanoparticles with Bidentate Benzene Derivatives, *J. Phys. Chem. C.* 113 (2009) 12645–12652. doi:10.1021/jp9013338.
  - [71] E. Kim, Y. Liu, X.W. Shi, X. Yang, W.E. Bentley, G.F. Payne, Biomimetic approach to confer redox activity to thin chitosan films, *Adv. Funct. Mater.* 20 (2010) 2683–2694. doi:10.1002/adfm.200902428.
  - [72] I.A. Janković, Z. V. Šaponjić, E.S. Džunuzović, J.M. Nedeljković, New Hybrid Properties of TiO<sub>2</sub> Nanoparticles Surface Modified With Catecholate Type Ligands, *Nanoscale Res. Lett.* 5 (2010) 81–88. doi:10.1007/s11671-009-9447-y.
  - [73] G.L. Wang, J.J. Xu, H.Y. Chen, Dopamine sensitized nanoporous TiO<sub>2</sub> film on electrodes: Photoelectrochemical sensing of NADH under visible irradiation, *Biosens. Bioelectron.* 24 (2009) 2494–2498. doi:10.1016/j.bios.2008.12.031.
  - [74] E. Kim, Y. Liu, W.E. Bentley, G.F. Payne, Redox capacitor to establish bio-device redox-connectivity, *Adv. Funct. Mater.* 22 (2012) 1409–1416. doi:10.1002/adfm.201101946.
  - [75] E. Kim, Z. Liu, Y. Liu, W. Bentley, G. Payne, Catechol-Based Hydrogel for Chemical Information Processing, *Biomimetics.* 2 (2017) 11. doi:10.3390/biomimetics2030011.
  - [76] S. Wu, E. Kim, J. Li, W.E. Bentley, X.-W. Shi, G.F. Payne, Catechol-Based Capacitor for Redox-Linked Bioelectronics, *ACS Appl. Electron. Mater.* (2019) acsaelm.9b00272. doi:10.1021/acsaelm.9b00272.
  - [77] J.A. Fagan, M. Zheng, V. Rastogi, J.R. Simpson, C.Y. Khripin, C.A. Silvera

- Batista, A.R. Hight Walker, Analyzing surfactant structures on length and chirality resolved (6,5) single-wall carbon nanotubes by analytical ultracentrifugation, *ACS Nano*. 7 (2013) 3373–3387. doi:10.1021/nn4002165.
- [78] S. Mukhopadhyay, U. Maitra, Chemistry and Biology of Bile Acids, *Curr. Sci.* 87 (2004) 1666–1683.
- [79] L. Galantini, M.C. di Gregorio, M. Gubitosi, L. Travaglini, J.V. Tato, A. Jover, F. Meijide, V.H. Soto Tellini, N. V. Pavel, Bile salts and derivatives: Rigid unconventional amphiphiles as dispersants, carriers and superstructure building blocks, *Curr. Opin. Colloid Interface Sci.* 20 (2015) 170–182. doi:10.1016/j.cocis.2015.08.004.
- [80] K.S. Munir, C. Wen, Deterioration of the Strong  $sp^2$  Carbon Network in Carbon Nanotubes during the Mechanical Dispersion Processing—A Review, *Crit. Rev. Solid State Mater. Sci.* 41 (2016) 347–366. doi:10.1080/10408436.2015.1127205.
- [81] M.S. Ata, I. Zhitomirsky, Colloidal methods for the fabrication of carbon nanotube-manganese dioxide and carbon nanotube-polypyrrole composites using bile acids, *J. Colloid Interface Sci.* 454 (2015) 27–34. doi:10.1016/j.jcis.2015.05.014.
- [82] M.S. Ata, R. Poon, A.M. Syed, J. Milne, I. Zhitomirsky, New developments in non-covalent surface modification, dispersion and electrophoretic deposition of carbon nanotubes, *Carbon N. Y.* 130 (2018) 584–598. doi:10.1016/j.carbon.2018.01.066.

**Chapter 3: Biomimetically modified chitosan for electrophoretic deposition of composites**

A. Clifford, X. Pang and I. Zhitomirsky

Colloids and Surfaces A: Physicochemical and Engineering Aspects

Volume 544, pp. 28-34

5 May 2018

Reprinted with permission. © 2018 Elsevier

### 3.1 Abstract

A one-step cathodic electrophoretic deposition (EPD) method has been developed for the deposition of chitosan (CHIT) films modified with catechol. Our approach was based on the use of 3,4-dihydroxybenzaldehyde (DHBA) molecules, which contain a catechol moiety for CHIT modification using a Schiff base reaction. We discussed the deposition mechanism as well as advantages of our one-step EPD method, compared to other techniques. It was found that the EPD method allowed the fabrication of redox-active films. A conceptually new strategy has been developed based on the use of CHIT-DHBA as a reducing, capping, dispersing, charging and film forming agent for the *in-situ* reduction of  $\text{Ag}^+$  ions, followed by catecholate type bonding of CHIT-DHBA to Ag particles, their electrosteric dispersion and EPD of composite CHIT-DHBA-Ag films. Building on the processing advantages offered by one-step cathodic deposition and remarkable bonding properties of catechol we performed EPD of CHIT-DHBA-hydroxyapatite (HA) and CHIT-DHBA- $\text{TiO}_2$  films. Another major finding was the use of CHIT-DHBA for electrosteric co-dispersion and charging of HA and  $\text{TiO}_2$ , followed by EPD of composite CHIT-DHBA- $\text{TiO}_2$ -HA films. Comprehensive electrochemical characterization and electron microscopy was used to characterize the microstructure of the films, as well as the electrochemical properties. The results of this investigation pave the way for the synthesis and agglomerate-free processing of various functional inorganic materials and fabrication of organic-inorganic composites for biomedical, sensor and water purification applications.



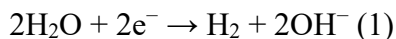
### 3.2 Introduction

Chitosan (CHIT) is a low cost, non-toxic, biodegradable and biocompatible natural polymer. It has been used for a variety of applications, such as drug delivery systems, tissue engineering, cosmetics, biosensors, wastewater treatment and in the food industry [1–4]. CHIT has previously been combined with functional organic and inorganic materials for the fabrication of advanced composites [5–7]. However, poor tissue adhesive properties of CHIT in the presence of body fluids has limited the biomedical applications of this polymer [8].

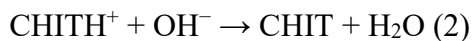
A relatively recent development was the chemical modification of CHIT with a catechol-containing moiety using chemical, electrochemical and enzymatic methods [8]. Interest in catechol modified CHIT ((CT-CHIT)) [9] was generated following the investigation of the outstanding adsorption properties of mussel adhesive proteins (MAPs) in solutions with high ionic strength. It is known [10] that MAPs contain catecholic amino acid, L-3,4-dihydroxyphenylalanine (DOPA), which allows for strong bonding to various substrates. Catechol is now considered to be an essential component of many advanced moisture resistant adhesives [10]. Adhesion of MAPs to inorganic materials is attributed to the complexation of metal atoms on material surfaces by the OH group of catechol. Catechol conjugation has been found to result in a significant increase in the mucoadhesion of CHIT [11]. It was also found that CHIT modified with DOPA exhibited enhanced mechanical properties and reduced swelling in wet conditions [12], which allows for the use of CHIT in load-bearing biomaterials.

CT-CHIT was used for the fabrication of adhesive magnetic composites [13], which facilitated immobilization of biomolecules. CT-CHIT resins [14] showed enhanced adsorption of metal ions, compared to pure chitosan. Various biomedical applications of CT-CHIT included advanced drug delivery and gene delivery systems, cancer thermotherapy, hemostatic materials, tissue engineering and biosensors [8].

Many of CHIT's applications are based on the use of films and coatings [1,15–17]. Electrophoretic deposition (EPD), as a coating technique, has generated significant interest for fabrication of CHIT films. In this method [18], the  $\text{NH}_2$  groups of water insoluble CHIT were protonated in acidic solutions to form water soluble cationic  $\text{CHITH}^+$ , which electromigrated toward cathode under the influence of an electric field. The pH increase at the cathode surface due to reaction



and deprotonation of  $\text{NH}_3^+$  groups of chitosan by the electrogenerated base (Eq. (1))



resulting in the fabrication of water insoluble CHIT films.

Many previous investigations have focused on co-deposition of CHIT with inorganic functional materials, such as ZnO [19], hydroxyapatite [18],  $\text{TiO}_2$  [20], bioglass [20,21],  $\text{SiO}_2$  [22],  $\text{CaSiO}_3$  [23,24], halloysite [25], hexagonal boron nitride [26] and Ag

[27]. Electrochemical strategies have been developed for the co-deposition of CHIT with drugs [1,21], proteins [28], enzymes [20] and antimicrobial agents [20]. Composite films have also been developed by co-deposition of CHIT with graphene [29] and carbon nanotubes [20]. EPD of chitosan has generated significant interest for the fabrication of biomedical devices [30,31].

EPD has also been utilized for the deposition of modified CT-CHIT films [32]. A two-step method has been developed, which involved cathodic EPD of pure CHIT, followed by an anodic electro-grafting process. In the electrografting step CHIT coated substrates were immersed in catechol solutions and an anodic process was utilized for to oxidize the molecule from catechol to *o*-quinone, which covalently reacted with amine groups in the CHIT monomer [32]. Despite the impressive progress [32–35] achieved in the EPD of CT-CHIT films for application in biomedical devices, further development of EPD method offers various benefits for a wide variety of medical applications.

The goal of this investigation was to develop a one-step cathodic EPD process for CHIT, modified with 3,4-dihydroxybenzaldehyde (DHBA) molecules, which contain a catechol moiety. In this approach we avoided the anodic electro-grafting of *o*-quinone and eliminated the inherent problems, which are related to anodic dissolution of CHIT films. Moreover, we avoided the oxidation of catechol in electrode reactions and its transformation to *o*-quinone. Our DHBA-CHIT films prepared by EPD were found to be electrochemically active and exhibited redox properties. This new approach allowed for better utilization of redox and bonding properties of catechol. Building on the advantages of our approach, we demonstrated various strategies for the deposition of composite films.

One strategy involved the use of DHBA-CHIT for *in situ* reduction of  $\text{Ag}^+$ , followed by the catecholate bonding of synthesized Ag particles to DHBA-CHIT and EPD of DHBA-CHIT-Ag films. In another strategy, catecholate type bonding of DHBA-CHIT to hydroxyapatite (HA) and  $\text{TiO}_2$  was used for the fabrication of stable suspensions for EPD of DHBA-CHIT films, that contained HA or/and  $\text{TiO}_2$ . We report the electrochemical properties of DHBA-CHIT and composite films, as well as discuss future applications of our new approach, which were developed in this investigation.

### 3.3 Experimental Procedures

Chitosan (CHIT, degree of deacetylation of 85%,  $M_w=200,000$ ), 3,4-dihydroxybenzaldehyde (DHBA),  $\text{Ru}(\text{NH}_3)_6\text{Cl}_3$ , phosphate buffer saline (pH=7), Hank's balanced salt solution ( $0.14 \text{ g L}^{-1} \text{ CaCl}_2$ ,  $0.40 \text{ g L}^{-1} \text{ KCl}$ ,  $0.06 \text{ g L}^{-1} \text{ KH}_2\text{PO}_4$ ,  $0.10 \text{ g L}^{-1} \text{ MgCl}_2 \cdot 6\text{H}_2\text{O}$ ,  $0.10 \text{ g L}^{-1} \text{ MgSO}_4 \cdot 7\text{H}_2\text{O}$ ,  $8.00 \text{ g L}^{-1} \text{ NaCl}$ ,  $0.35 \text{ g L}^{-1} \text{ NaHCO}_3$ ,  $0.048 \text{ g L}^{-1} \text{ Na}_2\text{HPO}_4$ ,  $1.00 \text{ g L}^{-1}$  glucose,  $0.01 \text{ g L}^{-1}$  phenol red),  $\text{TiO}_2$  (rutile,  $< 100 \text{ nm}$ ),  $\text{AgNO}_3$ , acetic acid,  $\text{Ca}(\text{NO}_3)_2 \cdot 4\text{H}_2\text{O}$ ,  $(\text{NH}_4)_2\text{HPO}_4$ , and  $\text{NH}_4\text{OH}$  were purchased from Sigma-Aldrich Canada.

Hydroxyapatite (HA) was prepared by slowly adding 0.6 M  $(\text{NH}_4)_2\text{HPO}_4$  solution into a 1.0 M  $\text{Ca}(\text{NO}_3)_2$  solution at  $70^\circ\text{C}$ . The solution pH was adjusted to 11 using  $\text{NH}_4\text{OH}$ . The resulting solution was stirred for 8 h at  $70^\circ\text{C}$  and 24 h at room temperature. The precipitate was washed with water, followed by rinsing with ethanol and then dried in air.

CHIT was modified in a solid phase with DHBA to form modified CHIT(s)-DHBA material. In this procedure, as-received CHIT particles were added to an aqueous solution

that contained DHBA. The mass ratio of CHIT: DHBA was 1:2. Obtained yellow powder was washed and dried for subsequent characterization. In another procedure, CHIT was modified in the liquid phase to form a  $\text{CHITH}^+$ -DHBA solution, which was used for EPD of CHIT-DHBA and CHIT-DHBA composite films. In a typical procedure, CHIT was dissolved in 1% acetic acid to form  $\text{CHITH}^+$ , which contained protonated  $\text{NH}_3^+$  groups. Addition of DHBA (mass ratio CHIT:DHBA=1:2) to  $\text{CHITH}^+$  resulted in the formation of yellow  $\text{CHITH}^+$ -DHBA solution. This solution was diluted with ethanol to form a solution (30% water) for EPD, which contained  $0.5 \text{ g L}^{-1}$  CHIT.

DHBA was used as a reducing agent for the synthesis of Ag. In the feasibility studies,  $\text{AgNO}_3$  was added to a solution containing DHBA, which had a final concentration of  $7.5 \text{ g L}^{-1}$  DHBA and  $1 \text{ g L}^{-1}$   $\text{AgNO}_3$ . The solution was stirred at room temperature, and within a few minutes the colour changed from clear to dark yellow and then to grey, which indicated the presence of silver nanoparticles. Formation of Ag particles was confirmed by XRD and TEM. Building on this experiment, Ag nanoparticles were synthesized using  $\text{CHITH}^+$ -DHBA solution and used for EPD of CHIT-DHBA-Ag films.

The electrochemical cell for EPD contained a cathodic substrate and Pt counter electrode. The distance between electrodes was 15 mm. Cathodic EPD was performed on different conductive substrates, such as Au wires, platinized silicon wafers, Pt and stainless steel (type 304) foils at a deposition voltage of 50 V. At lower voltages relatively low deposition yield was observed. An increase in the voltage above 50 V, resulted in enhanced gas evolution at the electrode surface. CHIT-DHBA films were deposited from  $\text{CHITH}^+$ -DHBA solutions. EPD of CHIT-DHBA-HA, CHIT-DHBA- $\text{TiO}_2$ , CHIT-DHBA-HA- $\text{TiO}_2$ ,

and CHIT-DHBA-Ag composites was performed from CHITH<sup>+</sup>-DHBA solutions that contained HA, TiO<sub>2</sub>, HA and TiO<sub>2</sub>, and AgNO<sub>3</sub>, respectively. The concentration of HA and TiO<sub>2</sub> particles in the chitosan solution was 1 g L<sup>-1</sup>. The concentration of AgNO<sub>3</sub> in the CHITH<sup>+</sup>-DHBA solution was 0.133 g L<sup>-1</sup>. The CHITH<sup>+</sup>-DHBA solution, that contained AgNO<sub>3</sub> was stirred for 1 h to form Ag particles *in-situ* before the EPD.

A Bruker Vertex 70 spectrometer was used for Fourier transform infrared spectroscopy (FTIR). A JEOL JSM-7000F microscope was used for scanning electron microscopy (SEM), and a FEI Tecnai Osiris transmission electron microscope was used for transmission electron microscopy (TEM). X-ray diffraction (XRD) experiments were carried out using a Nicolet I2 powder diffractometer, with monochromatized CuK $\alpha$  radiation.

Electrochemical investigations were performed using a PARSTAT 2273 (Princeton Applied Research) combined with the corresponding PowerSuite electrochemical software. A conventional three-electrode cell was used for the electrochemical measurements, with a platinum plate as the counter electrode and a saturated calomel electrode (SCE) as the reference electrode. Potentiodynamic polarization measurements were performed at a scan rate of 1 mV s<sup>-1</sup>, and Hank's balanced salt solution was used as the electrolyte. Cyclic voltammetry studies were performed at a scan rate of 5 mV s<sup>-1</sup> in Hank's balanced salt solution or phosphate buffer saline solution, pure or containing 50  $\mu$ M Ru(NH<sub>3</sub>)<sub>6</sub>Cl<sub>3</sub>.

### 3.4 Results and Discussion

Figure 3-1 shows the chemical structures of CHIT and DHBA. CHIT (Figure 3-1A) is a natural cationic polysaccharide that can be produced by alkaline N-deacetylation of chitin. Water soluble and positively charged CHIT was prepared by the protonation of amino groups in acidic solution. The chemical structure of DHBA (Figure 3-1B) includes a catechol group and an aldehyde group.

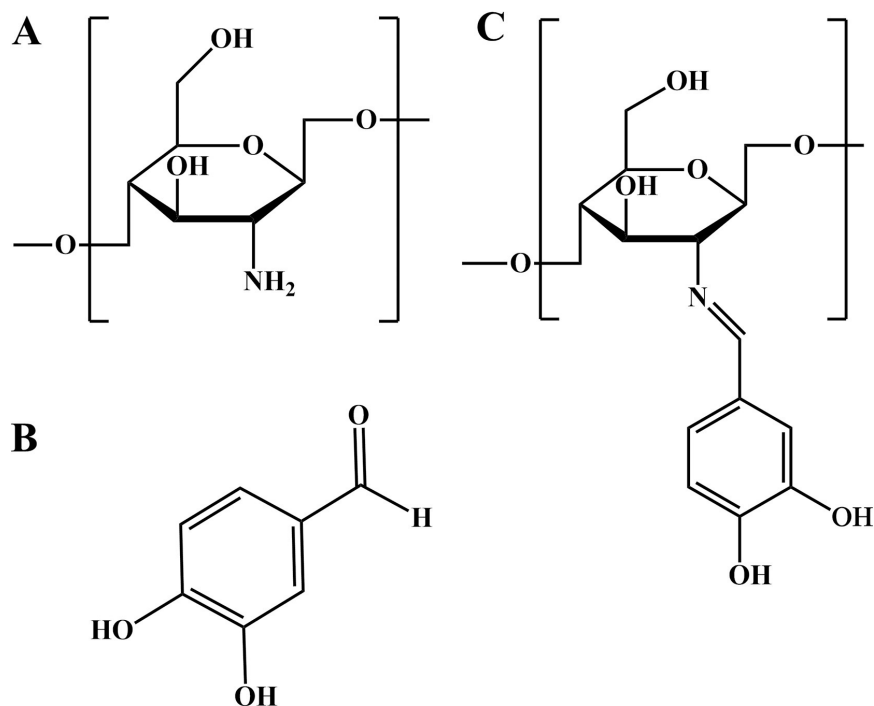


Figure 3-1: Chemical structures of (A) CHIT, (B) DHBA and (C) CHIT-DHBA.

A Schiff base [36] (Figure 3-1C) was formed by chemical interaction between the amino groups of CHIT and aldehyde group of DHBA. EPD from  $\text{CHIT}^{\text{H}^+}$ -DHBA solution resulted in the deposition of CHIT-DHBA films. The deposition mechanism involved a pH

increase at the cathode surface (reaction (1)) and precipitation of water insoluble CHIT-DHBA. Figure 3-2 shows the typical cross section of a CHIT-DHBA film. The films deposited using EPD were relatively dense and thick.

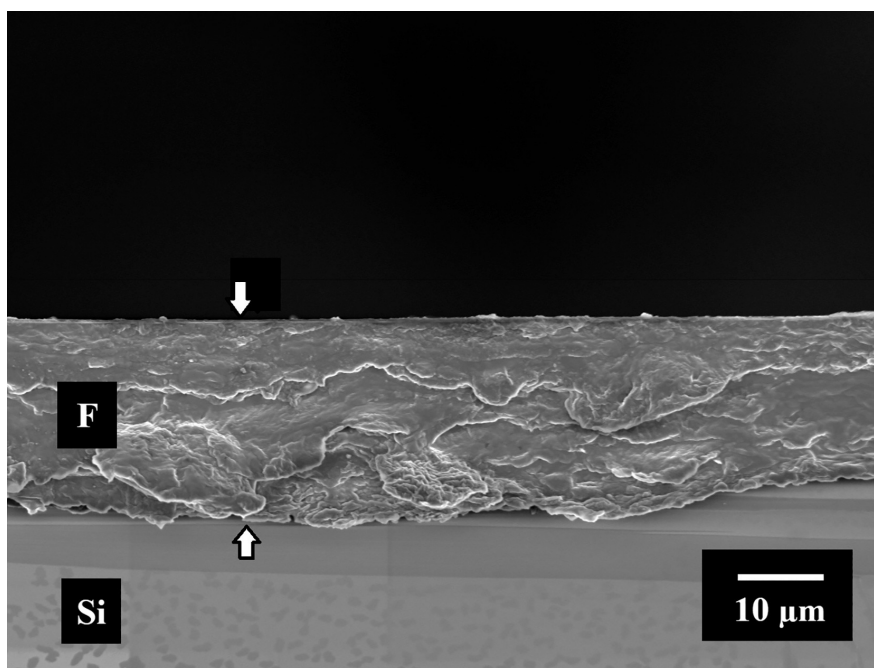


Figure 3-2: SEM image of a cross section of a CHIT-DHBA film (F) on a platinized silicon (Si) wafer substrate.

Schiff base [36,37] formation between DHBA and chitosan was confirmed using FTIR. Figure 3-3 compares the FTIR spectra of as-received DHBA and CHIT powders, DHBA modified CHIT powders (CHIT(s)-DHBA) and deposited CHIT-DHBA. The FTIR spectra of as-received DHBA and CHIT are in agreement with the data provided by the manufacturers. The spectra of CHIT(s)-DHBA and deposited CHIT-DHBA showed additional absorptions at 1290 and 1293  $\text{cm}^{-1}$ , respectively, compared to the spectrum of



pure CHIT. A similar absorption attributed to stretching vibrations of the phenolic group  $\nu(\text{C-OH})$  [38] was observed in the spectrum of pure DHBA. Moreover, the spectra of CHIT(s)-DHBA and deposited CHIT-DHBA showed additional absorptions at 1639 and 1641  $\text{cm}^{-1}$ , respectively, which resulted from vibrations corresponding to the C=N functional groups [36,37]. These absorptions are indicative of the Schiff base formation, and confirm modification of the CHIT monomer [36,37].

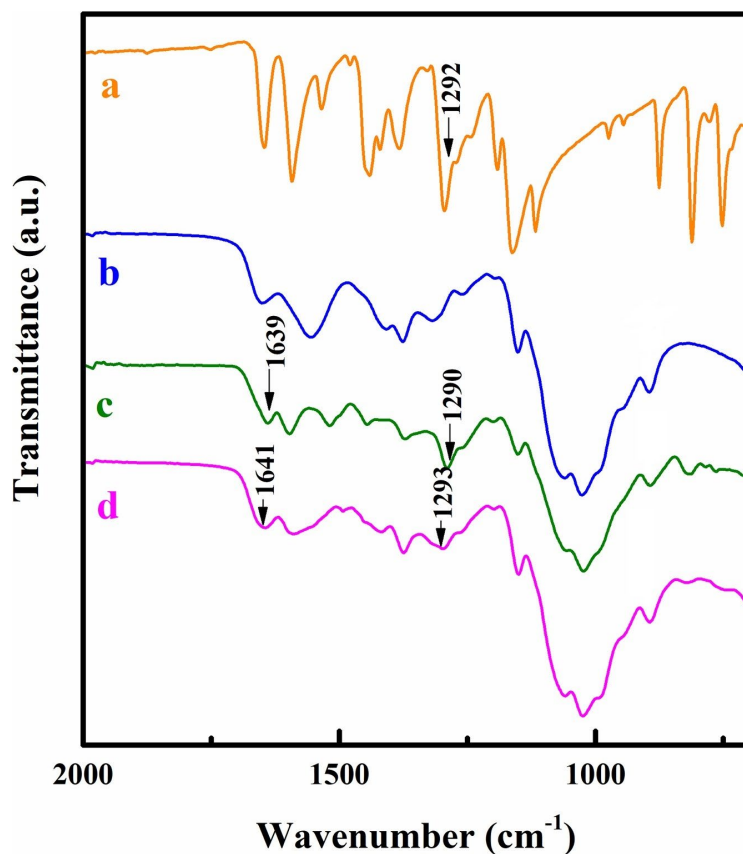


Figure 3-3: FTIR spectra of as-received (a) DHBA and (b) CHIT powders, (c) DHBA modified CHIT powders and (d) deposited CHIT-DHBA.

The CHIT-DHBA films exhibited different electrochemical behavior, compared to unmodified CHIT films. Figure 3-4 shows cyclic voltammograms (CVs) for CHIT and CHIT-DHBA films in a Hank's balanced salt solution. CVs for CHIT-DHBA films showed significantly higher currents and larger area due to the capacitive contribution of catechol. It is in this regard that catechol has a relatively high specific capacity [39,40] of  $1750 \text{ C g}^{-1}$ . The corresponding two-electron redox reaction involves oxidation of phenolic OH groups of catechol to form corresponding *o*-quinone. However, the electrochemistry of catechol is not fully understood [39]. The analysis of literature on the electrochemical oxidation of catechol indicated that the redox behavior is influenced by various factors, such as pH and composition of the electrolyte [39–46]. The CVs of catechol modified electrodes, exhibited complex shapes with several broad redox waves [39,41,42,46], resulting from two-electron processes.

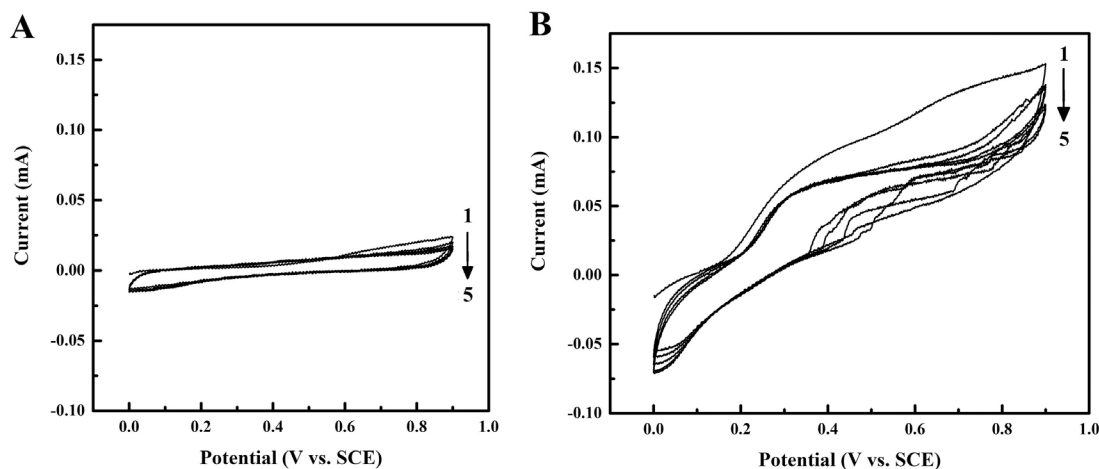


Figure 3-4: CVs for (A) pure CHIT and (B) CHIT-DHBA deposited on Pt in Hank's balanced salt solution, collected at a scan rate of  $5 \text{ mV s}^{-1}$ , the arrows show increasing cycle number.

Figure 3-5 compares CVs in phosphate buffered saline (pH=7) containing 50  $\mu\text{M}$   $\text{Ru}(\text{NH}_3)_6\text{Cl}_3$  for pure CHIT and CHIT-DHBA deposited on Au. The CHIT-DHBA film showed significant amplification of the redox currents, which confirmed the redox activity of CHIT-DHBA. This observation is in agreement with literature data, which showed that catechol modified films displayed signal amplification as a result of interaction with soluble redox active materials [34,43].

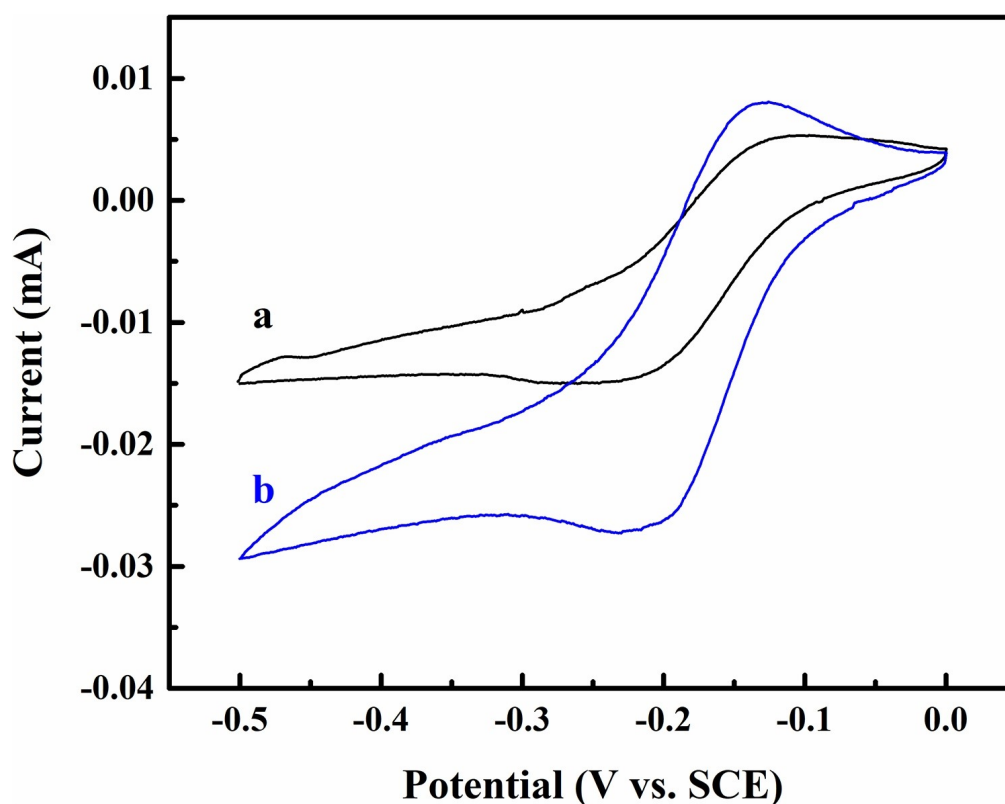


Figure 3-5: CVs for (a) pure CHIT and (b) CHIT-DHBA deposited on Au in phosphate buffered saline (pH=7) containing 50  $\mu\text{M}$   $\text{Ru}(\text{NH}_3)_6\text{Cl}_3$ , collected at a scan rate of 5  $\text{mV s}^{-1}$ .

The redox activity of immobilized DHBA was utilized for the *in-situ* synthesis of Ag nanoparticles and EPD of composite CHIT-DHBA-Ag films. It was found that DHBA can be used as a reducing agent for the synthesis of Ag nanoparticles from the  $\text{AgNO}_3$  solutions. Figure 3-6 shows a TEM image of Ag particles, prepared by reduction of  $\text{Ag}^+$  in  $\text{AgNO}_3$  solutions using DHBA as a reducing agent. The TEM characterization revealed that typical particle size was below 30 nm.

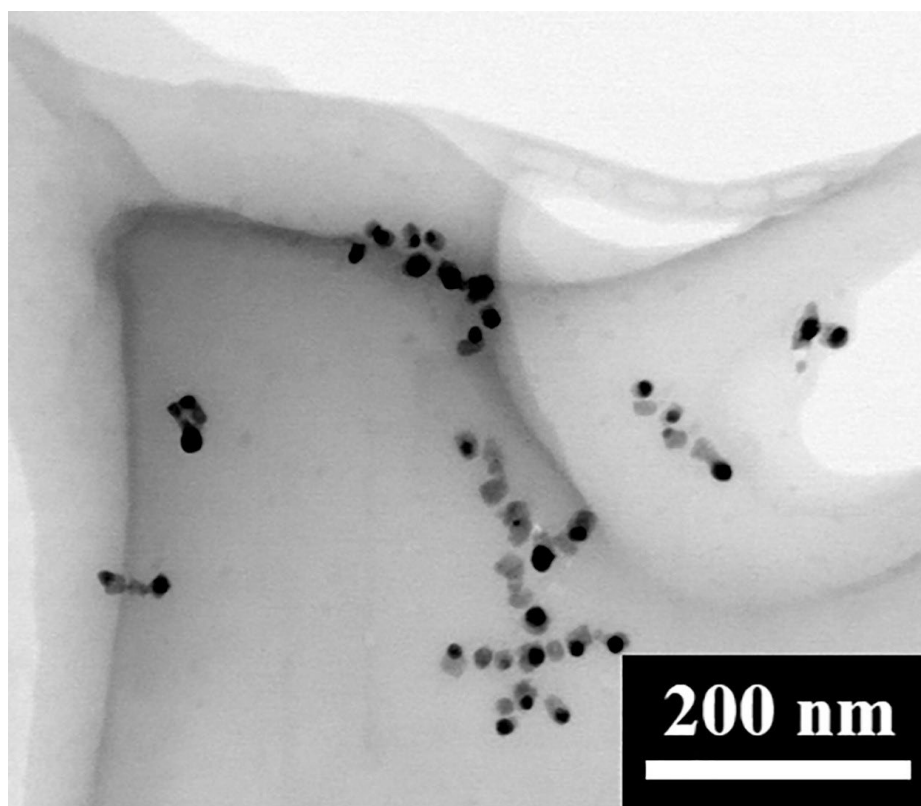


Figure 3-6: TEM image of Ag particles, prepared by reduction of  $\text{Ag}^+$  in  $\text{AgNO}_3$  solutions using DHBA as a reducing agent.

Figure 3-7a shows X-ray diffraction pattern of Ag particles, prepared by reduction of  $\text{Ag}^+$  in  $\text{AgNO}_3$  solutions using DHBA as a reducing agent. The X-ray diffraction pattern shows well defined diffraction peaks for Ag, corresponding to the JCPDS file 04-0783. The deposited material exhibited similar peaks (Figure 3-7b) and indicated the formation of CHIT-DHBA-Ag composite films.

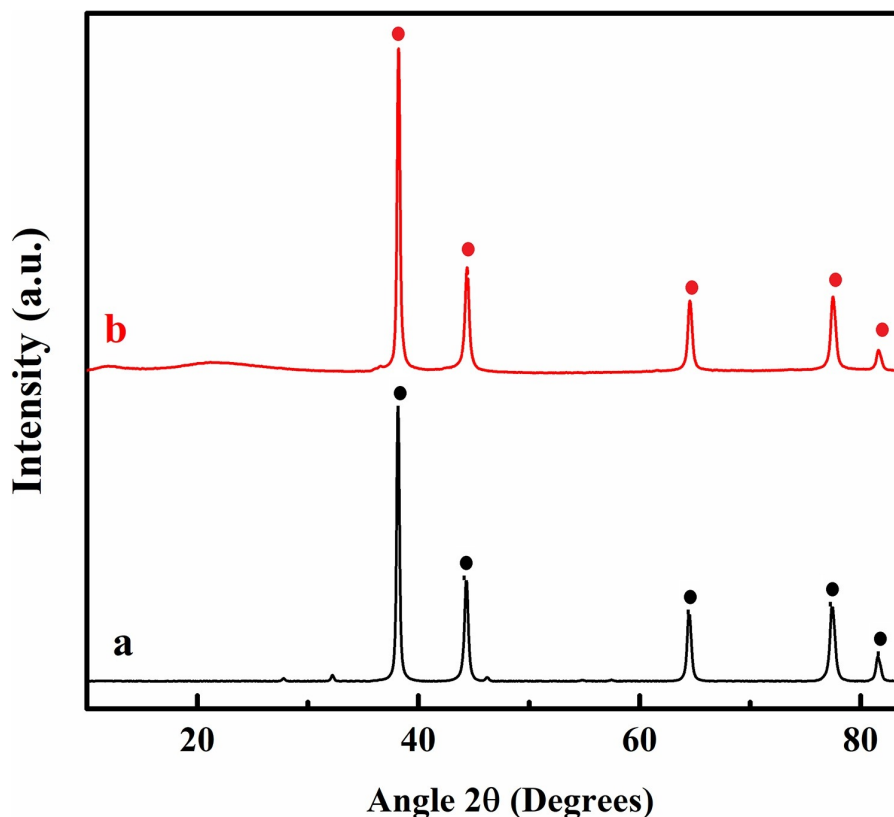


Figure 3-7: X-ray diffraction patterns of (a) Ag particles, prepared by reduction of  $\text{Ag}^+$  in  $\text{AgNO}_3$  solutions using DHBA as a reducing agent and (b) CHIT-DHBA-Ag deposit prepared by EPD (● – peaks, corresponding to JCPDS file 04-0783 for Ag).

It should be noted that previous experiments on EPD from CHIT solutions containing  $\text{AgNO}_3$  resulted in the deposition of amorphous  $\text{Ag}^+$ -chitosan complexes [27]. In contrast, the use of  $\text{CHITH}^+$ -DHBA solutions in this investigation allowed *in-situ* synthesis of crystalline Ag nanoparticles and their incorporation into the composite films. It is suggested

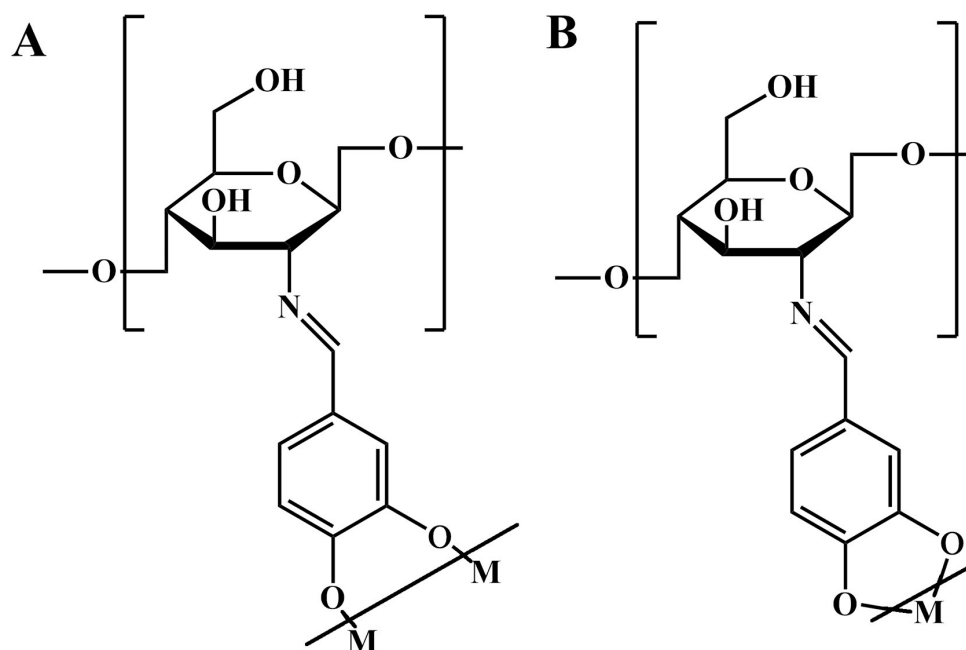


Figure 3-8: Adsorption of CHIT-DHBA on inorganic particles, involving (A) bridging and (B) chelating bonding to metal atoms (M) on the particle surface.

that  $\text{CHITH}^+$ -DHBA adsorbed on Ag particles and facilitated their dispersion and deposition. Previous investigations [10] showed that various aromatic molecules from the catechol family adsorbed on inorganic particles and allowed for them to be deposited using EPD. The adsorption mechanism involved interaction of such molecules with metal atoms on the particle surface. Similar catecholate type bonding mechanisms [10] can be suggested for the CHIT-DHBA adsorption on Ag. The adsorption can involve bridging (Figure 3-8A)

or chelation (Figure 3-8B) bonding of DHBA to the surface Ag atoms. Incorporation of Ag into the CHIT-DHBA films was also confirmed by the analysis of CV data for the composite films. The CV for the first cycle showed a strong redox peak, which is related to Ag oxidation (Figure 3-9), but the following CVs showed a significant decrease in the peak current. The peak practically disappeared after the 4th cycle. A similar peak was observed [47] for Ag-polymer composite films, prepared by layer-by-layer assembly and attributed to Ag oxidation to  $\text{Ag}_2\text{O}$ .

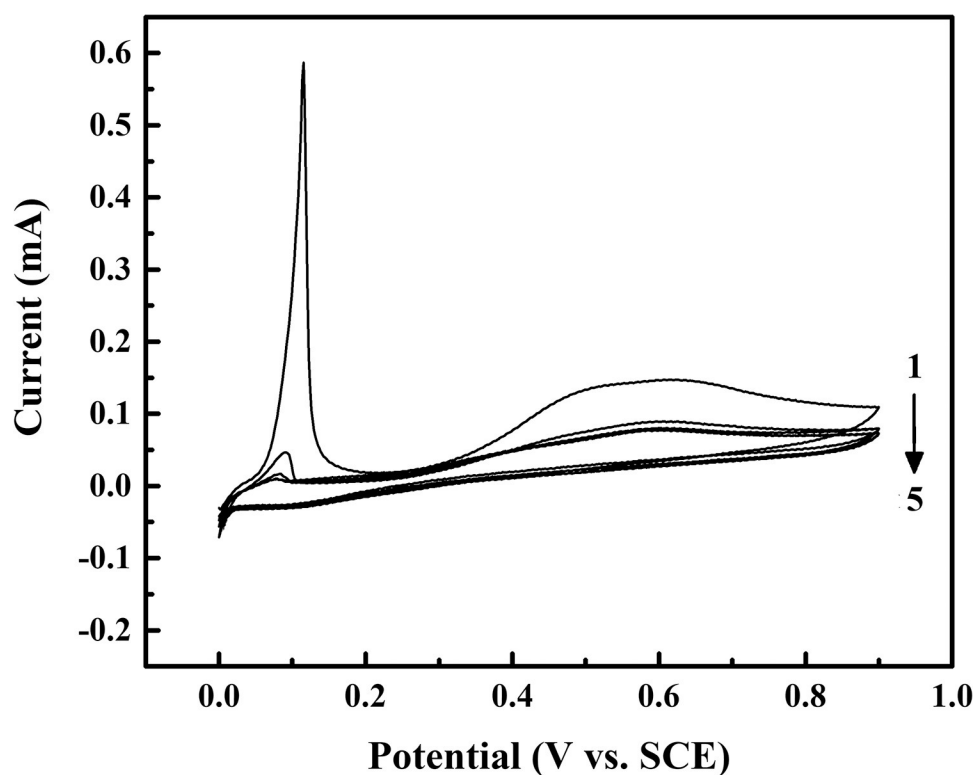


Figure 3-9: CV for CHIT-DHBA-Ag, coated on Pt in Hank's balanced salt solution, collected at a scan rate of  $5 \text{ mV s}^{-1}$ , the arrow shows increasing cycle number.

Previous investigations [10] showed that catecholate type bonding mechanisms can be used for the adsorption of various small organic molecules on particles of metals. The adsorbed molecules facilitated particle dispersion, imparted electric charge to the particles and allowed for their deposition using EPD. Use of CHIT-DHBA as a dispersing agent offers the advantage of improved particle dispersion, due to the large size of CHIT, which provides enhanced electrosteric stabilization. The results of this investigation pave the way for the in-situ synthesis of other metal particles and their incorporation into the CHIT-DHBA films by EPD. Our preliminary investigations, which are currently under way, indicate that a similar approach can be used for the *in-situ* synthesis of Au nanoparticles and deposition of CHIT-DHBA-Au nanocomposites.

It is important to note that catecholic molecules have shown ultra-strong adsorption [10] on various metal oxides and hydroxides. Therefore, it was suggested that adsorption mechanism shown in Figure 3-8 can be used for the dispersion and deposition of metal oxide and hydroxide particles. Towards this goal, we prepared stable suspensions of TiO<sub>2</sub> and HA using CHIT<sup>+</sup>-DHBA as a dispersing agent and performed EPD of CHIT-DHBA-TiO<sub>2</sub> and CHIT-DHBA-HA films. Catecholate-type bonding of DHBA to TiO<sub>2</sub> and HA allowed for strong adsorption of CHIT-DHBA on the particle surface, facilitated particle transfer to the electrode, followed by composite film formation. The CHIT-DHBA-TiO<sub>2</sub> and CHIT-DHBA-HA films are promising for potential applications as biomedical implant materials. HA is an important material for biomedical implant applications, because its chemical composition is similar to that of natural bone [20]. Rutile is known as a bioactive material, which promotes HA biomineralization [48–50]. Compared to the anatase



modification, the rutile phase of  $\text{TiO}_2$  has many advantages for implant applications, such as phase stability, chemical stability and improved corrosion protection [51].

Figure 3-10 shows SEM images of the films prepared by EPD. The EPD method resulted in the formation of smooth and crack-free films. The SEM images of composite films show inorganic particles dispersed within the CHIT-DHBA matrix and confirmed co-deposition of the particles and CHIT-DHBA.

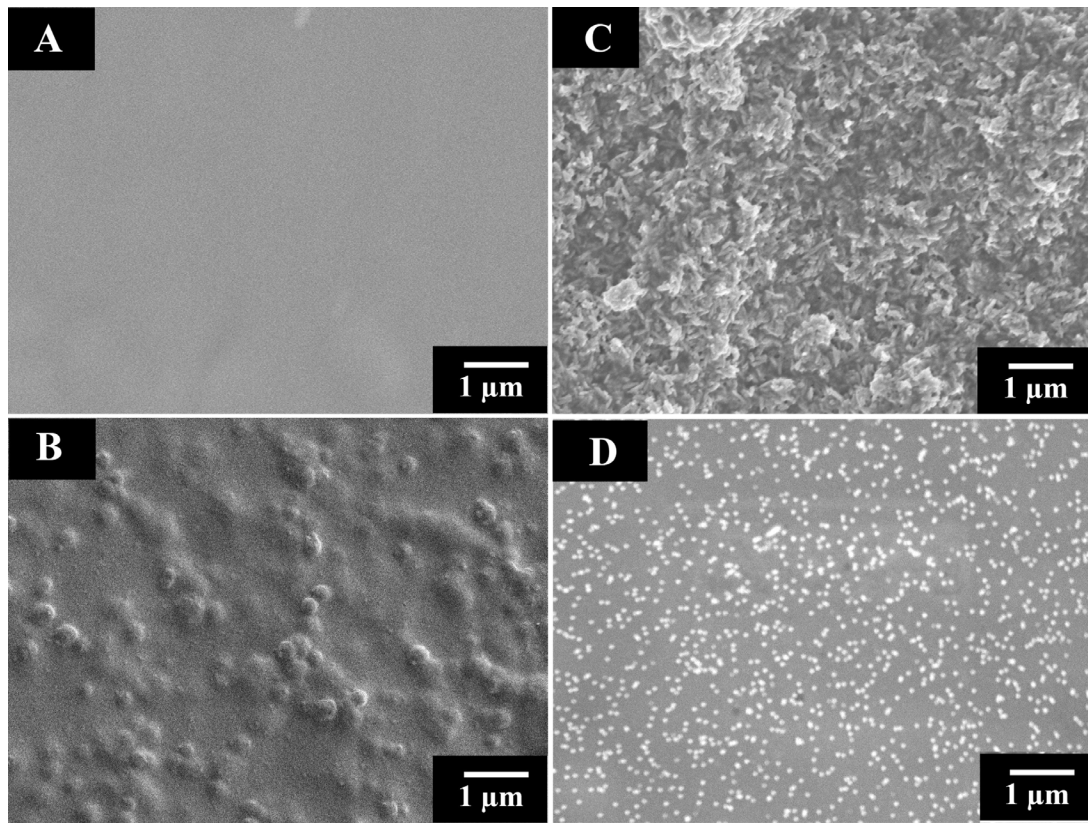


Figure 3-10: SEM images of (A) pure CHIT-DHBA, (B) CHIT-DHBA- $\text{TiO}_2$ , (C) CHIT-DHBA-HA and (D) CHIT-DHBA-Ag films, prepared by EPD.

The X-ray diffraction patterns of the CHIT-DHBA-HA and CHIT-DHBA-TiO<sub>2</sub> deposits showed peaks of HA and TiO<sub>2</sub>, respectively (Figure 3-11a and b). Therefore, the XRD data presented in Figure 3-11a and b, coupled with the data shown in Figure 3-7b provided additional evidence of the formation of composite films by EPD.

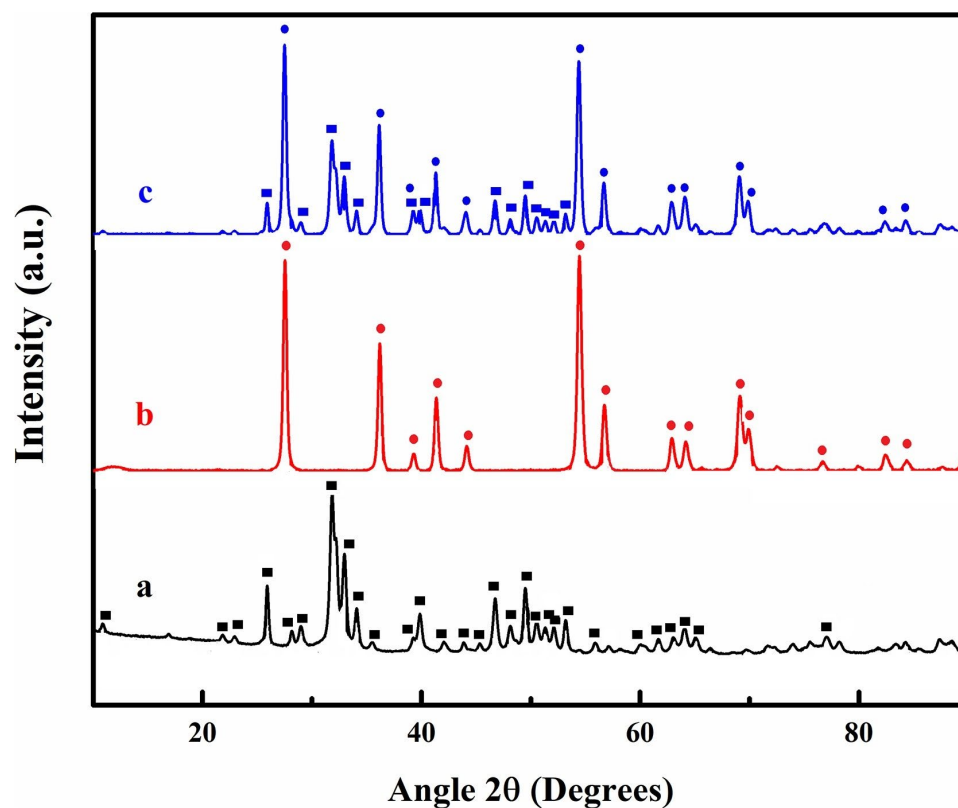


Figure 3-11: XRD patterns of (a) CHIT-DHBA-HA, (b) CHIT-DHBA-TiO<sub>2</sub> and (c) CHIT-DHBA-TiO<sub>2</sub>-HA films, prepared from 0.5 g L<sup>-1</sup> CHIT<sup>+</sup>-DHBA solutions, containing (a) 1 g L<sup>-1</sup> HA, (b) 1 g L<sup>-1</sup> TiO<sub>2</sub> and (c) 1 g L<sup>-1</sup> HA and 1 g L<sup>-1</sup> TiO<sub>2</sub>, (■ - peaks corresponding to JCPDS file 09-0432 for HA, ● - peaks corresponding to JCPDS file 021-1276 for TiO<sub>2</sub>).

Figure 3-12 shows Tafel plots for uncoated stainless steel and coated with CHIT-DHBA-TiO<sub>2</sub> film. Studies were performed in Hank's balanced salt solution, which acted as a simulated body fluid. From the Tafel plots it can be seen that film deposition allowed the corrosion current to be reduced from 4.09  $\mu\text{A cm}^{-2}$  for uncoated stainless steel to 1.17  $\mu\text{A cm}^{-2}$  for the CHIT-DHBA-TiO<sub>2</sub> coated stainless steel. Moreover, the coated substrate showed a higher corrosion potential. These results indicated that the CHIT-DHBA-TiO<sub>2</sub> acted as a protective layer and provided corrosion protection to the stainless-steel substrates.

CHIT<sup>+</sup>-DHBA has also been used as a co-dispersant and film forming agent for the co-deposition of TiO<sub>2</sub> and HA and fabrication of CHIT-DHBA-TiO<sub>2</sub>-HA films. The X-ray diffraction pattern of the composite films (Figure 3-11c) showed both peaks corresponding to HA and TiO<sub>2</sub>, which provided evidence of co-deposition of both inorganic materials. Fabrication of TiO<sub>2</sub>-HA composite coatings has many benefits, such as enhanced chemical stability, improved corrosion protection of implants, bioactivity, improved mechanical properties, enhanced osteoblast adhesion and cell growth [52–56].

As pointed out above, modification of CHIT with catechol offers many advantages for various applications. The redox properties of the CHIT-DHBA are promising for application in sensors. The metal chelating properties of DHBA offer benefits for water purification devices. Moreover, CHIT<sup>+</sup>-DHBA can potentially be used as an electrochemically active binder for advanced energy storage devices. The new strategies developed in this investigation offer benefits for synthesis and EPD of nanocomposites. Of particular importance is the use of CHIT<sup>+</sup>-DHBA as a reducing, capping, dispersing,

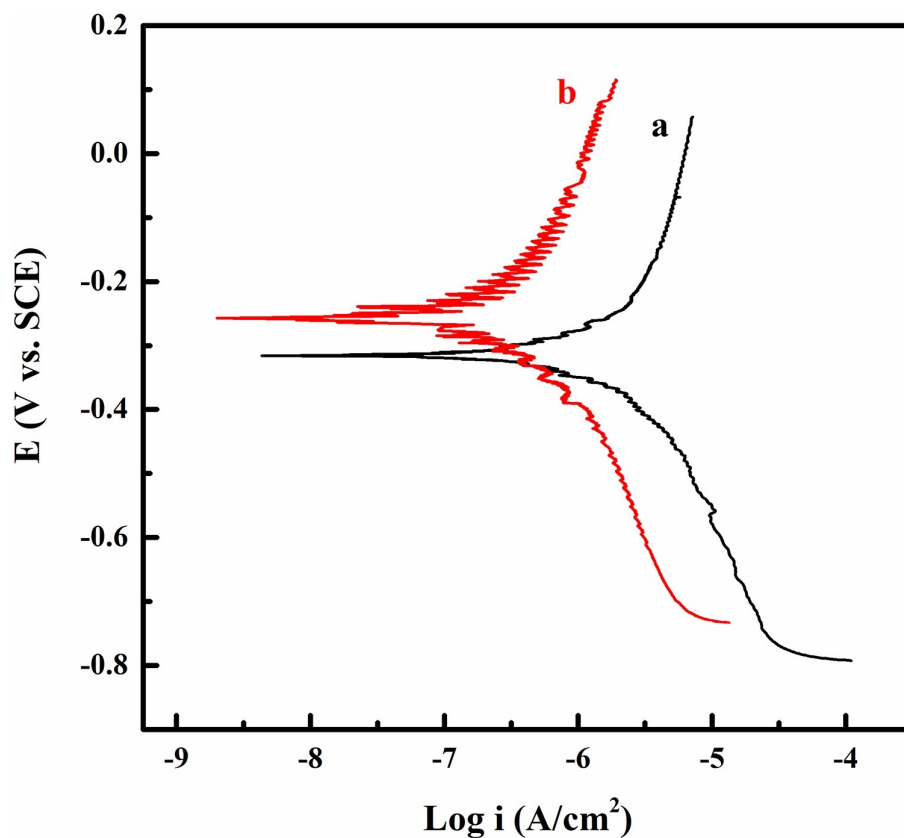


Figure 3-12: Tafel plots in Hank's solutions for (a) uncoated stainless steel and (b) coated stainless steel by deposition from  $1 \text{ g L}^{-1}$   $\text{TiO}_2$  suspension, containing  $0.5 \text{ g L}^{-1}$   $\text{CHITH}^+$ -DHBA.

charging and film forming agent for the *in-situ* synthesis of Ag nanoparticles, their electrosteric dispersion, charging and EPD of nanocomposite films. This strategy offers benefits of exceptional catecholate type bonding of  $\text{CHITH}^+$ -DHBA to the particle surface. The incorporation of Ag into the CHIT films can impart antimicrobial properties, whereas HA and  $\text{TiO}_2$  can improve biocompatibility and bioactivity of CHIT films. Expansion of these studies will result in the EPD of other nanocomposites, containing non-agglomerated

inorganic particles in a CHIT matrix. We believe that similar approach can be used for the biomimetic modification and EPD of other advanced polymers, containing amino groups, such as polyethylenimine, polyallylamine, polyvinylamine, poly-L-lysine and poly-L-ornithine. The unique ability of catechol to bond to different inorganic materials offers advantages of co-deposition of different inorganic materials using CHIT<sup>H+</sup>-DHBA as a dispersing, charging and film forming agent.

### 3.5 Conclusions

A one-step cathodic electrophoretic deposition (EPD) method has been developed for the deposition of chitosan (CHIT) films modified with DHBA molecules, which contained a catechol moiety using the Schiff base reaction. The films showed promising redox-active and bonding properties, which can potentially be used for the application in sensors, energy storage and water purification devices. A conceptually new strategy has been developed based on the use of CHIT-DHBA as a reducing, capping, dispersing, charging and film forming agent for the *in-situ* reduction of Ag<sup>+</sup> ions, followed by the catecholate type bonding of CHIT-DHBA to Ag particles, their electrosteric dispersion in suspension and EPD of composite CHIT-DHBA-Ag films. Building on the processing advantages offered by the one-step cathodic deposition and remarkable bonding properties of catechol we performed EPD of CHIT-DHBA-HA and CHIT-DHBA-TiO<sub>2</sub> films. Another major finding was the use of CHIT-DHBA for electrosteric co-dispersion and charging of HA and TiO<sub>2</sub>, followed by the EPD of composite CHIT-DHBA-TiO<sub>2</sub>-HA films. The incorporation of Ag, HA and TiO<sub>2</sub> particles can potentially improve

antimicrobial properties, biocompatibility and bioactivity for diverse applications in biomedical implants. The colloidal and surface modification strategies developed in this investigation pave the way for agglomerate free *in-situ* synthesis of nanoparticles of other metals and their incorporation in composite films by EPD. Moreover, the unique adsorption properties of catecholates, such as DHBA are promising for the deposition and co-deposition of various oxide materials and EPD of composite organic-inorganic films. The approach developed in this investigation can potentially be utilized for biomimetic modification of other functional polymers and EPD of novel composites.

### 3.6 Acknowledgements

The authors gratefully acknowledge the Natural Sciences and Engineering Research Council of Canada for the financial support.

### 3.7 References

- [1] H. Yi, L.-Q. Wu, W.E. Bentley, R. Ghodssi, G.W. Rubloff, J.N. Culver, G.F. Payne, Biofabrication with chitosan, *Biomacromolecules* 6 (2005) 2881–2894.
- [2] G.Z. Kyzas, D.N. Bikiaris, A.C. Mitropoulos, Chitosan adsorbents for dye removal: a review, *Polym. Int.* 66 (2017) 1800–1811.
- [3] R. LogithKumar, A. KeshavNarayan, S. Dhivya, A. Chawla, S. Saravanan, N. Selvamurugan, A review of chitosan and its derivatives in bone tissue engineering, *Carbohydr. Polym.* 151 (2016) 172–188.
- [4] A.R. Pandey, U.S. Singh, M. Momin, C. Bhavsar, Chitosan: application in tissue engineering and skin grafting, *J. Polym. Res.* (2017) 24.

- [5] Z. Moridi, V. Mottaghitlab, A.K. Haghi, A detailed review of recent progress in carbon nanotube/chitosan nanocomposites, *Cellul. Chem. Technol.* 45 (2011) 549–563.
- [6] V. Balan, L. Verestiuc, Strategies to improve chitosan hemocompatibility: a review, *Eur. Polym. J.* 53 (2014) 171–188.
- [7] J. Venkatesan, S.-K. Kim, Chitosan composites for bone tissue engineering—an overview, *Mar. Drugs* 8 (2010) 2252–2266.
- [8] J.H. Ryu, S. Hong, H. Lee, Bio-inspired adhesive catechol-conjugated chitosan for biomedical applications: a mini review, *Acta Biomater.* 27 (2015) 101–115.
- [9] A.I. Neto, A.C. Cibrão, C.R. Correia, R.R. Carvalho, G.M. Luz, G.G. Ferrer, G. Botelho, C. Picart, N.M. Alves, J.F. Mano, Nanostructured polymeric coatings based on chitosan and dopamine-modified hyaluronic acid for biomedical applications, *Small* 10 (2014) 2459–2469.
- [10] M. Ata, Y. Liu, I. Zhitomirsky, A review of new methods of surface chemical modification, dispersion and electrophoretic deposition of metal oxide particles, *RSC Adv.* 4 (2014) 22716–22732.
- [11] K. Kim, K. Kim, J.H. Ryu, H. Lee, Chitosan-catechol: a polymer with long-lasting mucoadhesive properties, *Biomaterials* 52 (2015) 161–170.
- [12] D.X. Oh, D.S. Hwang, A biomimetic chitosan composite with improved mechanical properties in wet conditions, *Biotechnol. Prog.* 29 (2013) 505–512.
- [13] K. Ni, X. Zhou, L. Zhao, H. Wang, Y. Ren, D. Wei, Magnetic catechol-chitosan with bioinspired adhesive surface: preparation and immobilization of  $\omega$ -transaminase, *PloS One* 7 (2012) e41101.
- [14] K. Oshita, T. Takayanagi, M. Oshima, S. Motomizu, Adsorption properties of ionic species on cross-linked chitosans modified with catechol and salicylic acid moieties, *Anal. Sci.* 24 (2008) 665–668.
- [15] I. Zhitomirsky, A. Hashambhoy, Chitosan-mediated electrosynthesis of organic–inorganic nanocomposites, *J. Mater. Process. Technol.* 191 (2007) 68–72.

- [16] V. Ambroggi, D. Pietrella, M. Nocchetti, S. Casagrande, V. Moretti, S. De Marco, M. Ricci, Montmorillonite–chitosan–chlorhexidine composite films with antibiofilm activity and improved cytotoxicity for wound dressing, *J. Colloid Interface Sci.* 491 (2017) 265–272.
- [17] H.D.M. Follmann, A.F. Naves, A.F. Martins, O. Félix, G. Decher, E.C. Muniz, R. Silva, Advanced fibroblast proliferation inhibition for biocompatible coating by electrostatic layer-by-layer assemblies of heparin and chitosan derivatives, *J. Colloid Interface Sci.* 474 (2016) 9–17.
- [18] X. Pang, I. Zhitomirsky, Electrodeposition of composite hydroxyapatite–chitosan films, *Mater. Chem. Phys.* 94 (2005) 245–251.
- [19] Y. Li, K. Wu, I. Zhitomirsky, Electrodeposition of composite zinc oxide–chitosan films, *Colloids Surf. Physicochem. Eng. Asp.* 356 (2010) 63–70.
- [20] A.R. Boccaccini, S. Keim, R. Ma, Y. Li, I. Zhitomirsky, Electrophoretic deposition of biomaterials, *J. R. Soc. Interface* 7 (2010) S581.
- [21] F. Sun, K. Sask, J. Brash, I. Zhitomirsky, Surface modifications of nitinol for biomedical applications, *Colloids Surf. B Biointerfaces* 67 (2008) 132–139.
- [22] K. Grandfield, I. Zhitomirsky, Electrophoretic deposition of composite hydroxyapatite–silica–chitosan coatings, *Mater. Charact.* 59 (2008) 61–67.
- [23] S. Sharma, V.P. Soni, J.R. Bellare, Chitosan reinforced apatite–wollastonite coating by electrophoretic deposition on titanium implants, *J. Mater. Sci. Mater. Med.* 20 (2009) 1427–1436.
- [24] X. Pang, T. Casagrande, I. Zhitomirsky, Electrophoretic deposition of hydroxyapatite–CaSiO<sub>3</sub>–chitosan composite coatings, *J. Colloid Interface Sci.* 330 (2009) 323–329.
- [25] I. Deen, X. Pang, I. Zhitomirsky, Electrophoretic deposition of composite chitosan halloysite nanotube–hydroxyapatite films, *Colloids Surf. Physicochem. Eng. Asp.* 410 (2012) 38–44.
- [26] N.S. Raddaha, L. Cordero-Arias, S. Cabanas-Polo, S. Virtanen, J.A. Roether, A.R. Boccaccini, Electrophoretic deposition of chitosan/h-BN and chitosan/h-BN/TiO<sub>2</sub>



- composite coatings on stainless steel (316L) substrates, *Materials* 7 (2014) 1814–1829.
- [27] X. Pang, I. Zhitomirsky, Electrodeposition of hydroxyapatite–silver–chitosan nanocomposite coatings, *Surf. Coat. Technol.* 202 (2008) 3815–3821.
- [28] R. Ma, I. Zhitomirsky, Electrophoretic deposition of chitosan-albumin and alginate albumin films, *Surf. Eng.* 27 (2011) 51–56.
- [29] F. Ordikhani, M. Ramezani Farani, M. Dehghani, E. Tamjid, A. Simchi, Physicochemical and biological properties of electrodeposited graphene oxide/chitosan films with drug-eluting capacity, *Carbon* 84 (2015) 91–102.
- [30] S.T. Koev, P.H. Dykstra, X. Luo, G.W. Rubloff, W.E. Bentley, G.F. Payne, R. Ghodssi, Chitosan: an integrative biomaterial for lab-on-a-chip devices, *Lab Chip* 10 (2010) 3026–3042.
- [31] M.J. Kastantin, Sheng Li, A.P. Gadre, Li-Qun Wu, W.E. Bentley, G.F. Payne, G.W. Rubloff, R. Ghodssi, Integrated fabrication of polymeric devices for biological applications, *Sens. Mater.* 15 (2003) 295–311.
- [32] E. Kim, Y. Liu, X. Shi, X. Yang, W.E. Bentley, G.F. Payne, Biomimetic approach to confer redox activity to thin chitosan films, *Adv. Funct. Mater.* 20 (2010) 2683–2694.
- [33] E. Kim, T. Gordonov, W.E. Bentley, G.F. Payne, Amplified and in situ detection of redox-active metabolite using a biobased redox capacitor, *Anal. Chem.* 85 (2013) 2102–2108.
- [34] T.E. Winkler, H. Ben-Yoav, S.E. Chocron, E. Kim, D.L. Kelly, G.F. Payne, R. Ghodssi, Electrochemical study of the catechol-modified chitosan system for clozapine treatment monitoring, *Langmuir* 30 (2014) 14686–14693.
- [35] E. Kim, Y. Liu, W.E. Bentley, G.F. Payne, Redox capacitor to establish bio-device redox-connectivity, *Adv. Funct. Mater.* 22 (2012) 1409–1416.
- [36] X. Jin, J. Wang, J. Bai, Synthesis and antimicrobial activity of the Schiff base from chitosan and citral, *Carbohydr. Res.* 344 (2009) 825–829.

- [37] T.F. Jiao, J. Zhou, J. Zhou, L. Gao, Y. Xing, X. Li, Synthesis and characterization of chitosan-based Schiff base compounds with aromatic substituent groups, *Iran. Polym. J.* 20 (2011) 123–136.
- [38] I.A. Jankovic, Z.V. Saponjic, M.I. Comor, J.M. Nedeljković, Surface modification of colloidal TiO<sub>2</sub> nanoparticles with bidentate benzene derivatives, *J. Phys. Chem. C* 113 (2009) 12645–12652.
- [39] T. Cottineau, M. Toupin, T. Delahaye, T. Brousse, D. Belanger, Nanostructured transition metal oxides for aqueous hybrid electrochemical supercapacitors, *Appl. Phys. A* 82 (2006) 599–606.
- [40] Z. Algharaibeh, P.G. Pickup, An asymmetric supercapacitor with anthraquinone and dihydroxybenzene modified carbon fabric electrodes, *Electrochem. Commun.* 13 (2011) 147–149.
- [41] N.H. Nguyen, C. Esnault, F. Gohier, D. Bélanger, C. Cougnon, Electrochemistry and reactivity of surface-confined catechol groups derived from diazonium reduction. Bias-assisted Michael addition at the solid/liquid interface, *Langmuir* 25 (2009) 3504–3508.
- [42] C.J. Meyers, S.D. Shah, S.C. Patel, R.M. Sneeringer, C.A. Bessel, N.R. Dollahon, R.A. Leising, E.S. Takeuchi, Templated synthesis of carbon materials from zeolites (Y, beta, and ZSM-5) and a montmorillonite clay (K10): physical and electrochemical characterization, *J. Phys. Chem. B* 105 (2001) 2143–2152.
- [43] G.E. Cabaniss, A.A. Diamantis, W.R. Murphy Jr, R.W. Linton, T.J. Meyer, Electrocatalysis of proton-coupled electron-transfer reactions at glassy carbon electrodes, *J. Am. Chem. Soc.* 107 (1985) 1845–1853.
- [44] S. Uchiyama, H. Watanabe, H. Yamazaki, A. Kanazawa, H. Hamana, Y. Okabe, Electrochemical introduction of amino group to a glassy carbon surface by the electrolysis of carbamic acid, *J. Electrochem. Soc.* 154 (2007) F31–F35.
- [45] A. Senthil Kumar, P. Swetha, Electrochemical-assisted encapsulation of catechol on a multiwalled carbon nanotube modified electrode, *Langmuir* 26 (2010) 6874–6877.

- [46] T. Nagaoka, T. Yoshino, Surface properties of electrochemically pretreated glassy carbon, *Anal. Chem.* 58 (1986) 1037–1042.
- [47] P. Singh, V.C. Solomon, D.A. Buttry, Electrochemistry of ATP-capped silver nanoparticles in layer-by-layer multilayer films, *J. Nanopart. Res.* 16 (2014) 2496.
- [48] Y. Cai, H. Li, M. Karlsson, K. Leifer, H. Engqvist, W. Xia, Biomineralization on single crystalline rutile: the modulated growth of hydroxyapatite by fibronectin in a simulated body fluid, *RSC Adv.* 6 (2016) 35507–35516.
- [49] C. Lindahl, P. Borchardt, J. Lausmaa, W. Xia, H. Engqvist, Studies of early growth mechanisms of hydroxyapatite on single crystalline rutile: a model system for bioactive surfaces, *J. Mater. Sci. Mater. Med.* 21 (2010) 2743–2749.
- [50] X. Lu, H. Zhang, Y. Leng, L. Fang, S. Qu, B. Feng, J. Weng, N. Huang, The effects of hydroxyl groups on Ca adsorption on rutile surfaces: a first-principles study, *J. Mater. Sci. Mater. Med.* 21 (2010) 1–10.
- [51] P. Kasemanankul, N. Witit-Anan, S. Chaiyakun, P. Limsuwan, V. Boonamnuayvitaya, Low-temperature deposition of (110) and (101) rutile TiO<sub>2</sub> thin films using dual cathode DC unbalanced magnetron sputtering for inducing hydroxyapatite, *Mater. Chem. Phys.* 117 (2009) 288–293.
- [52] X. Xiao, R. Liu, Y. Zheng, Characterization of hydroxyapatite/titania composite coatings codeposited by a hydrothermal–electrochemical method on titanium, *Surf. Coat. Technol.* 200 (2006) 4406–4413.
- [53] S.A. Ulasevich, A.I. Kulak, S.K. Poznyak, S.A. Karpushenkov, A.D. Lisenkov, E.V. Skorb, Deposition of hydroxyapatite–incorporated TiO<sub>2</sub> coating on titanium using plasma electrolytic oxidation coupled with electrophoretic deposition, *RSC Adv.* 6 (2016) 62540–62544.
- [54] R. Jaworski, L. Pawlowski, C. Pierlot, F. Roudet, S. Kozerski, F. Petit, Recent developments in suspension plasma sprayed titanium oxide and hydroxyapatite coatings, *J. Therm. Spray Technol.* 19 (2010) 240–247.

- [55] A.E. Hannora, S. Ataya, Structure and compression strength of hydroxyapatite/titania nanocomposites formed by high energy ball milling, *J. Alloys Compd.* 658 (2016) 222–233.
- [56] T.P.S. Sarao, H.S. Sidhu, H. Singh, Characterization and in vitro corrosion investigations of thermal sprayed hydroxyapatite and hydroxyapatite-titania coatings on Ti alloy, *Metall. Mater. Trans. A* (2012) 1–12.

**Chapter 4: Synthesis, liquid – liquid extraction and deposition of hydroxyapatite nanorod composites**

A. Clifford, M.S. Ata, and I. Zhitomirsky

Materials Letters

Volume 201, pp. 140-143

15 August 2017

Reprinted with permission. © 2017 Elsevier

#### **4.1 Abstract**

Hydroxyapatite (HA) nanorods were prepared using a wet chemical precipitation method. Lauryl gallate (LG) and hexadecylphosphonic acid (HDPA) showed strong adsorption on the surface of HA, which allowed for the transfer of the synthesized HA nanorods from the aqueous to the n-butanol phase at the interface of the two immiscible liquids. The extracted non-agglomerated HA particles were used for the fabrication of composite HA-polymer films. In this approach, problems related to particle agglomeration during the drying stage were avoided. Analysis of the adsorption mechanisms indicated that LG and HDPA are promising extractors for agglomerate free processing of nanomaterials using a liquid-liquid extraction method.

#### **4.2 Introduction**

Hydroxyapatite (HA)-polymer nanocomposites are important materials for biomedical and water purification applications [1,2]. One of the problems related to the synthesis of HA nanoparticles and their application for the fabrication of nanocomposites is related to its strong tendency to agglomerate. Reduction of the surface area and self-condensation of the surface OH groups during drying promotes the agglomeration of as-precipitated HA nanoparticles.

In this investigation, a liquid-liquid extraction method has been developed in an effort to avoid HA agglomeration, resulting from the drying process. Synthesized HA nanoparticles were transferred from the unstable suspension in water to an organic solvent through the interface of the two immiscible liquids. This process resulted in the formation

of stable suspensions of well dispersed HA particles in an organic solvent. We demonstrated the processing advantages of this strategy for the fabrication of HA biopolymer nanocomposite films, containing a water insoluble polymer. Our success with the liquid-liquid extraction of HA was largely the result of the use of novel extractors, such as lauryl gallate (LG) and hexadecylphosphonic acid (HDPA), which showed strong adsorption on HA particles. It was found in the literature that LG is important antibacterial [3] and antitumor [4] agent. HDPA belongs to a family of organophosphonates, which are widely used for the surface modification of biomaterials [5,6]. Furthermore, phosphonate additives promote biomineralization and improve biocompatibility and chemical stability of implant materials [7,8]. We report new applications of LG and HDPA as advanced extractors for HA, which allowed for high extraction efficiency. This approach offers a simple and efficient strategy for the synthesis other nanomaterials and composites.

#### **4.3 Experimental Procedures**

Lauryl gallate (LG), hexadecylphosphonic acid (HDPA),  $\text{Ca}(\text{NO}_3)_2 \cdot 4\text{H}_2\text{O}$ ,  $(\text{NH}_4)_2\text{HPO}_4$ ,  $\text{NH}_4\text{OH}$ , poly(methyl methacrylate) (PMMA) and n-butanol (Aldrich) were used. HA precipitation was performed at a temperature of 70 °C by the slow addition of a 0.6 M  $(\text{NH}_4)_2\text{HPO}_4$  solution to a 1.0 M  $\text{Ca}(\text{NO}_3)_2$  solution. The pH of the solutions was adjusted to 11 by the addition of  $\text{NH}_4\text{OH}$ . Then LG or HDPA solutions in n-butanol were added. After ultrasonication and stirring for 10 min, the HA particles were extracted to the n-butanol phase. The mass ratio of HA to the extractants was 3:1.

Suspensions containing the extracted HA particles were added to PMMA solution in acetone and obtained stable suspensions were used for spray coating of stainless-steel substrates. The mass ratio of HA and PMMA in the suspensions was 4:1.

Electron microscopy investigations were performed using a JEOL JSM-7000F scanning electron microscope (SEM) and FEI Tecnai Osiris transmission electron microscope (TEM). FTIR studies were performed on Bruker Vertex 70 spectrometer. X-ray diffraction (XRD) studies were performed using a powder diffractometer (Nicolet I2, CuK $\alpha$  radiation).

#### **4.4 Results and Discussion**

Liquid-liquid extraction of oxide and hydroxide nanomaterials offers many potential benefits, which have not been utilized for practical applications due to the lack of efficient extracting agents. Inspired by Nature's mechanisms of strong mussel adsorption on surfaces, which involves catechol groups from mussel adhesive proteins [9], we used LG as an extractor for HA particles. The chemical structure of LG (Figure 4-1A) includes a galloyl group, which similar to catechol, contains OH groups, which are bonded to adjacent carbon atoms of the aromatic ring. Previous investigations of catecholates and gallic acid adsorption showed that such molecules create bidentate chelating or bidentate bridging bonding with metal atoms on the particle surface [9]. Similar mechanisms can be suggested for the LG adsorption (Figure 4-1B) on HA particles. HDPa is another promising extractor molecule (Figure 4-1C) due to the presence of a phosphonate group. The adsorption mechanisms of the phosphonate molecules are based on bidentate or



tridentate bonding [10], involving chelation or bridging bonding (Figure 4-1D). LG and HDPA are of particular interest for extraction technology, because bidentate or tridentate bonding allow for superior bonding strength and adsorption, compared to monodentate bonding [9], which is typical for many extractors and dispersants. The structures of LG and HDPA include long hydrocarbon chains, which can be beneficial for steric stabilization of HA nanoparticles.

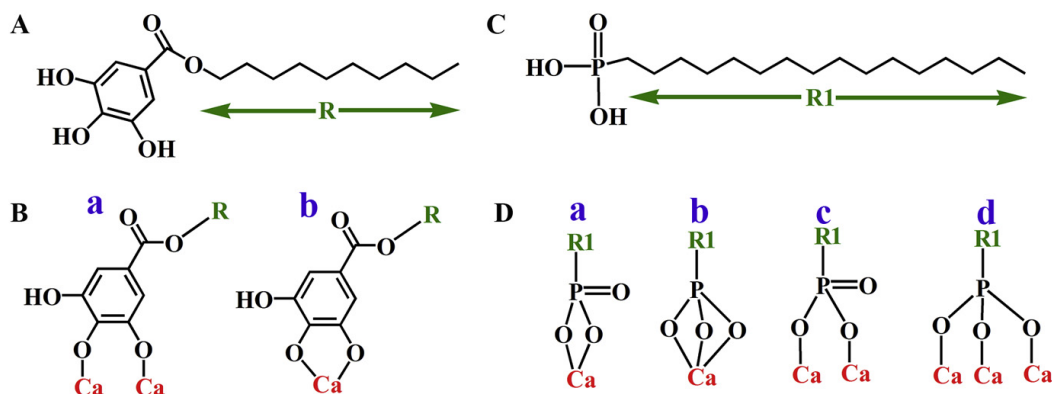


Figure 4-1: (A) Chemical structure of LG, (B) adsorption of LG, involving (a) bridging, (b) chelation, (C) chemical structure of HDPA, (D) adsorption of HDPA, involving (a, b) chelation, (c, d) bridging.

X-ray diffraction studies (Figure 4-2A) confirmed the formation of HA crystals. Figure 4-2B shows a TEM image of HA particles, which exhibit a nanorod morphology with a typical length of 150–200 nm and an aspect ratio of 8–10.

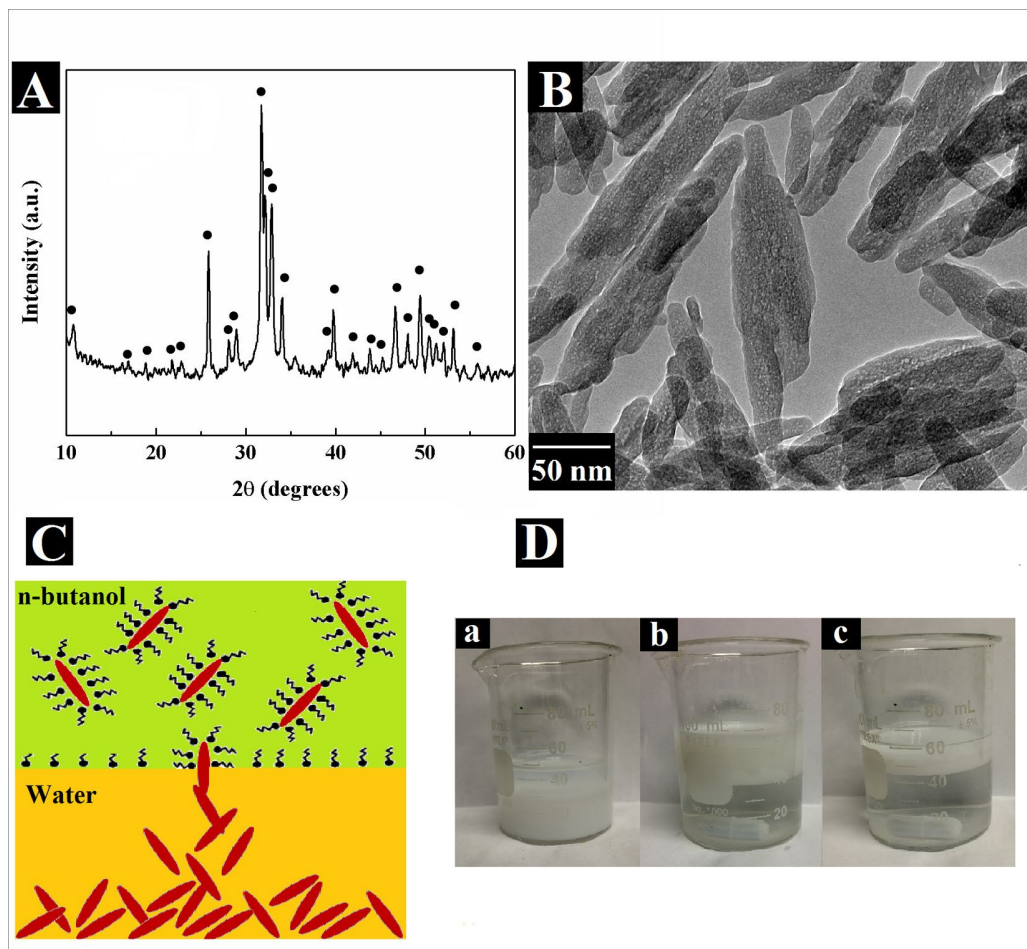


Figure 4-2: (A) X-ray diffraction pattern of HA (●- JCPDS file 09-0432), (B) TEM image of HA, (C) schematic of liquid-liquid extraction, (D) (a) as precipitated HA, (b) HA extraction using LG, (c) HA extraction using HDPA.

Previous investigations [9] showed that various water-soluble molecules, containing galloyl or phosphonate groups, adsorbed on oxide particles in water. Our extraction strategy was based on the use of water-insoluble molecules, such as LG, containing a galloyl group, and HDPA, containing a phosphonate group. In this strategy, the adsorption occurs at the interface of water and the organic solvent. After the synthesis, the HA particles were successfully extracted from the aqueous phase and transferred to n-

butanol. Figure 4-2C shows a schematic of the extraction mechanism, involving LG or HDPA adsorption on the HA particles at the liquid-liquid interface and HA transfer to the top n-butanol phase, which was achieved against the force of gravity. Figure 4-2D shows suspensions of HA before and after extraction. The synthesized HA precipitated in aqueous suspension, whereas the extracted HA formed stable suspensions due to the steric stabilization effect of adsorbed LG or HDPA. The formation of stable suspensions is critical for the colloidal processing, and the use of LG and HDPA allowed for high extraction efficiency.

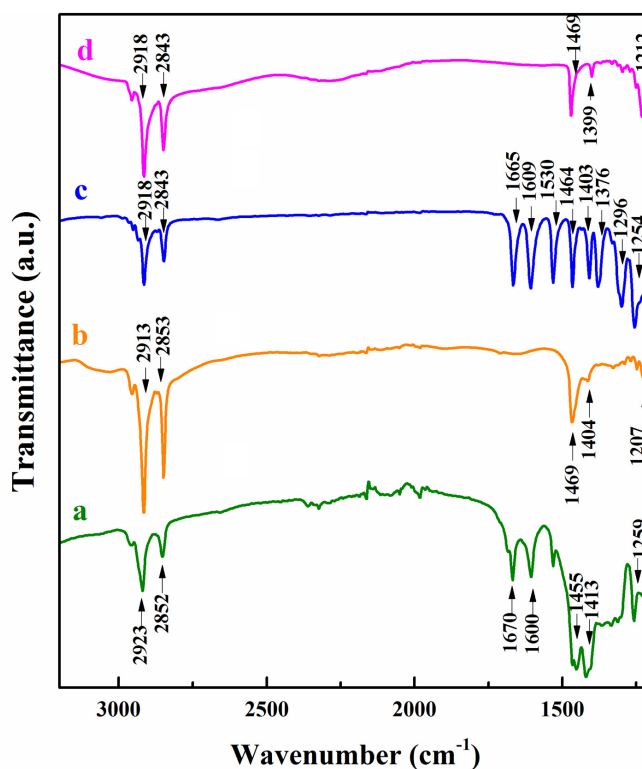


Figure 4-3: FTIR spectra of (a) HA, extracted using LG, (b) HA, extracted using HDPA, (c) LG (d) HDPA.

Adsorption of HDPA and LG on HA particles was confirmed by the analysis of FTIR spectra (Figure 4-3(a-d)). Absorptions at 1800–2000  $\text{cm}^{-1}$  in the spectra of extracted HA are attributed to the stretching vibrations of the aliphatic C-H bonds of the adsorbed organic molecules [11]. The FTIR spectra of HDPA and LG showed similar adsorptions. The LG adsorption on HA has also been confirmed by the observation of stretching vibrations of the C=O group [11] at 1670  $\text{cm}^{-1}$  and C-C stretching vibrations of aromatic ring in the range of 1400-1600  $\text{cm}^{-1}$ . Similar absorptions were observed in the spectrum of pure LG. The absorptions at 1469  $\text{cm}^{-1}$  in the spectra of HA, extracted using HDPA and pure HDPA material are attributed to the deformation C-H vibrations of HDPA.

For many different applications colloidal particles are prepared using chemical precipitation in water and must be subsequently dispersed in organic solvents that contain dissolved functional organic materials, which are water insoluble. We demonstrated the benefits of liquid-liquid extraction during preparation of HA-PMMA coatings, which contained water insoluble PMMA and extracted HA. Figure 4-4 compares the SEM images of dried HA powders, prepared from the suspension, shown in Figure 3-2D(a) to deposited coatings. Coatings prepared from the powder samples contained relatively large agglomerates, with a size of 1–5  $\mu\text{m}$  (Figure 4-4A). In contrast, the formation of such agglomerates was avoided in the deposited coatings, containing HA, prepared by liquid-liquid extraction. SEM images of the resultant coatings showed rod-like particles of HA and PMMA. (Figure 4-4B-C).

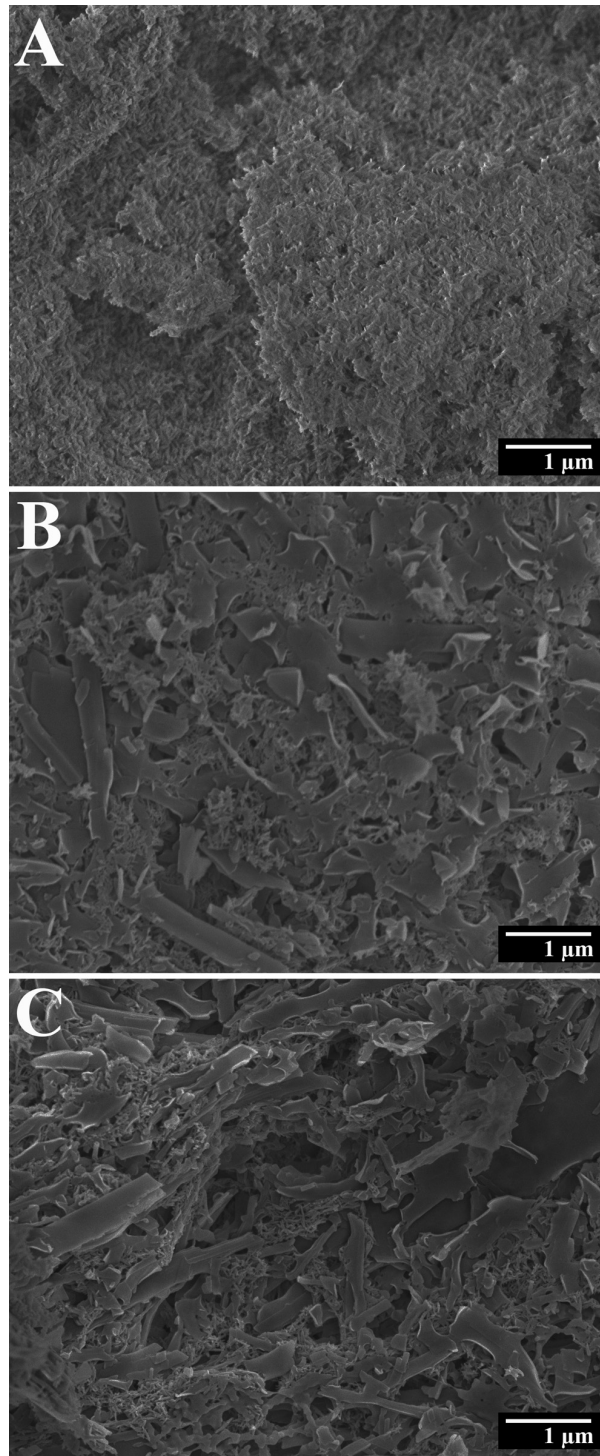


Figure 4-4: SEM images of (A) HA powder after drying, arrows show agglomerates, (B) HA-PMMA prepared using LG, (C) HA-PMMA prepared using HDPA.

## 4.5 Conclusions

Successful liquid-liquid extraction of HA was the result of the use of efficient extractors, which allow for strong adsorption on HA particles. The galloyl group of LG and phosphonate group of HDPa allowed for bi-or tridentate bonding to the Ca atoms on the HA surface, which resulted in a strong adsorption. Another important factor, which must be considered in the development of efficient extractors is their insolubility in water. Problems related to particle agglomeration during the drying stage can be avoided using liquid-liquid extraction. In addition, composite fabrication can also be simplified by avoiding the drying stage. Another benefit of the liquid-liquid extraction is the colloidal stabilization of HA particles transferred to the organic phase. The method can be used for the fabrication of organic-inorganic nanocomposites.

## 4.6 Acknowledgements

The authors acknowledge NSERC Canada for the financial support.

## 4.7 References

- [1] A.R. Boccaccini, S. Keim, R. Ma, Y. Li, I. Zhitomirsky, Electrophoretic deposition of biomaterials, *J. R. Soc. Interface* 7 (2010) S581–S613.
- [2] P. Koley, M. Sakurai, T. Takei, M. Aono, Facile fabrication of silk protein sericin mediated hierarchical hydroxyapatite-based bio-hybrid architectures: excellent adsorption of toxic heavy metals and hazardous dye from wastewater, *RSC Adv.* 6 (2016) 86607–86616.
- [3] I. Kubo, K. Fujita, K. Nihei, N. Masuoka, Non-antibiotic antibacterial activity of dodecyl gallate, *Bioorgan. Med. Chem.* 11 (2003) 573–580.

- [4] C. Locatelli, F.B. Filippin-Monteiro, T.B. Creczynski-Pasa, Alkyl esters of gallic acid as anticancer agents: a review, *Eur. J. Med. Chem.* 60 (2013) 233–239.
- [5] R. Boissezon, J. Muller, V. Beaugeard, S. Monge, J.-J. Robin, Organophosphonates as anchoring agents onto metal oxide-based materials: synthesis and applications, *RSC Adv.* 4 (2014) 35690–35707.
- [6] H.T. Ong, J.S.C. Loo, F.Y.C. Boey, S.J. Russell, J. Ma, K.-W. Peng, Exploiting the high-affinity phosphonate-hydroxyapatite nanoparticle interaction for delivery of radiation and drugs, *J. Nanoparticle Res.* 10 (2008) 141–150.
- [7] A. Zieba, G. Sethuraman, F. Perez, G.H. Nancollas, D. Cameron, Influence of organic phosphonates on hydroxyapatite crystal growth kinetics, *Langmuir* 12 (1996) 2853–2858.
- [8] C. Arnould, C. Volcke, C. Lamarque, P.A. Thiry, J. Delhalle, Z. Mekhalif, Titanium modified with layer-by-layer sol-gel tantalum oxide and an organodiphosphonic acid: a coating for hydroxyapatite growth, *J. Colloid Interface Sci.* 336 (2009) 497–503.
- [9] M. Ata, Y. Liu, I. Zhitomirsky, A review of new methods of surface chemical modification, dispersion and electrophoretic deposition of metal oxide particles, *RSC Adv.* 4 (2014) 22716–22732.
- [10] M. Ata, P. Wojtal, I. Zhitomirsky, Surface modification and electrophoretic deposition of materials using carboxyalkylphosphonic acids, *Mater. Lett.* 184 (2016) 320–323.
- [11] E.S. Dzunuzovic, J.V. Dzunuzovic, A.D. Marinkovic, M.T. Marinovi-Cincovic, K.B. Jeremic, J.M. Nedeljkovic, Influence of surface modified TiO<sub>2</sub> nanoparticles by gallates on the properties of PMMA/TiO<sub>2</sub> nanocomposites, in: *Eur. Polymer J.* 48 (2012) 1385–1393.

**Chapter 5: Biomimetic modification of poly-L-lysine and electrodeposition of nanocomposite coatings for orthopaedic applications**

A. Clifford, B.E.J. Lee, K. Grandfield and I. Zhitomirsky

Colloids and Surfaces B: Biointerfaces

Volume 176, pp.115-121

1 April 2019

Reprinted with permission. © 2018 Elsevier



## 5.1 Abstract

For the first time, a biomimetic method has been developed for the chemical modification of poly-L-lysine (PLL) with catechol in order to improve polymer adhesion to inorganic particles and surfaces. The method is based on the Schiff base reaction of amino groups of PLL monomers and aldehyde groups of 3,4-dihydroxybenzylaldehyde (DHBA) molecules. It was found that adherent PLL-DHBA films can be prepared by cathodic electrophoretic deposition (EPD). Nanocomposite coating with dual micro-nano topography have been developed for orthopaedic and dental coating applications. The catechol groups of PLL-DHBA facilitated its adsorption on hydroxyapatite (HA) and rutile ( $\text{TiO}_2$ ) and allowed for the fabrication of stable suspensions for EPD. PLL-DHBA was used as both a charging and film-forming agent for EPD of HA and  $\text{TiO}_2$ . Moreover, the methods allowed co-deposition of HA and  $\text{TiO}_2$  and fabrication of composite films, which combines the benefits of both bioceramics. In addition to having dual scale topography, the films exhibited both sub-micron surface roughness and hydrophilic behaviour, which both have been found to promote osteoblast adhesion and proliferation. *In vitro* studies revealed that the fabricated coatings showed increased cell metabolism and alkaline phosphatase activity over the period studied, with PLL-DHBA- $\text{TiO}_2$  showing the greatest increase. This work paves the way for both the development of the next generation of biomedical implant coatings, with improved osseointegration and lifespan, as well as one-step low-temperature processing.

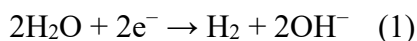
## 5.2 Introduction

Poly-L-lysine (PLL) is a cationic biopolymer that is synthesized from L-lysine, a naturally occurring essential amino acid found in food sources with high protein content, such as meat and eggs [1]. It has also been found to have anti-microbial properties [2,3], which makes it well suited for biomedical applications. The amine group in PLL is protonated in biological conditions and has been found to promote cell proliferation and adhesion [4]. As a result, PLL is commonly used as a coating agent in tissue culture equipment [5]. PLL has been used for a variety of biomedical applications, such as tissue scaffolds [2,3], drug delivery [4], cell labeling [6] and gene delivery [7]. PLL is also being explored for bone scaffold and orthopaedic coating applications, as it is believed to promote proliferation and adhesion of osteoblasts due to its peptide structure [4].

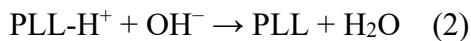
Recent interest has been generated in the area of biopolymer modification with catechol (CAT), in order to improve polymer adhesion to inorganic particles and surfaces. This interest is inspired by nature; observing the ability of the mussel to cling to inorganic surfaces in aggressive marine environments. This ability has been attributed to the presence of L-3,4-dihydroxyphenylalanine (L-DOPA), an amino acid that is the primary constituent of the adhesion protein in the byssal plaque [8]. The naturally occurring biopolymer, chitosan (CHIT) has been modified previously with CAT using a variety of techniques for modification, including reductive amination or chemical, enzymatic, or electrochemical synthesis [9]. A two-step method for electrochemical synthesis has been described, which involves the cathodic electrodeposition of chitosan, followed by anodic deposition of catechol [10]. We have previously developed a new one-step technique for the modification

of CHIT, utilizing the CAT containing organic compound 3,4-dihydroxybenzylaldehyde (DHBA) [11]. In our technique, CHIT-DHBA was fabricated by attaching DHBA to CHIT monomer at the amine group, utilizing a Schiff base reaction. CHIT-DHBA films were then fabricated using cathodic electrophoretic deposition (EPD).

EPD is an attractive coating technique for orthopaedic and dental implants due to its ability to coat substrates with complex shapes and incorporate multiple components while being relatively cheap and facile [12]. PLL films have previously been fabricated using EPD [13]. In this technique, it was suggested that the amino group of PLL became protonated upon the dissolution of PLL-hydrobromide in water, forming PLL-H<sup>+</sup>. PLL-H<sup>+</sup> then migrated towards the cathode under the influence of an applied electric field. The application of the electric field results in local increase in pH at the cathode surface, governed by the following reaction



As PLL polyelectrolyte enters the locally alkaline region at the cathode surface, it becomes deprotonated



and coagulates on the cathode surface, forming an electrically neutral and water insoluble film. Using this method, PLL has been used for the fabrication of organic-inorganic

composite films with hydroxyapatite (HA) [13], which is a synthetic bioceramic that has a chemical composition similar to the inorganic constituent in human bone [14]. There are no reports of the use of PLL for the electrodeposition or co-deposition of inorganic particles besides the aforementioned HA.

The goal of this investigation was to fabricate and characterize catechol-modified PLL composite films using a one-step electrodeposition technique and determine their feasibility for use as orthopaedic and dental implant coatings. In our work, we functionalized PLL with catechol and formed composite films with HA, and rutile ( $\text{TiO}_2$ ). We also achieved co-deposition of HA with  $\text{TiO}_2$ , and fabricated coatings with dual nano- and micro-scale topography in one step, which was found to promote adhesion and proliferation of osteoblast-like Saos-2 cells. This work paves the way for the fabrication of a new generation of nanocomposite coatings with superior adhesion and dual-scale topography for improved osseointegration and increased lifespan of biomedical implant materials.

## **5.3 Experimental Procedure**

### **5.3.1 Chemicals**

Poly-L-lysine hydrobromide (PLL-HBr), 3,4-dihydroxybenzylaldehyde (DHBA),  $\text{TiO}_2$  (rutile, <100 nm),  $\text{Ca}(\text{NO}_3)_2 \cdot 4\text{H}_2\text{O}$ ,  $(\text{NH}_4)_2\text{HPO}_4$ ,  $\text{NH}_4\text{OH}$  and titanium foil (0.127 mm) were purchased from Sigma-Aldrich Canada. HA nanorods were synthesised using wet chemical precipitation [15]. A solution consisting of 0.6 M  $(\text{NH}_4)_2\text{HPO}_4$  was slowly

added to 1.0 M  $\text{Ca}(\text{NO}_3)_2$  solution at 70°C. The solution pH was adjusted to 11 using  $\text{NH}_4\text{OH}$  and was stirred for 8 h at 70°C, followed by stirring for 24 h at room temperature. The average length of the synthesized HA nanorods was approximately  $169 \pm 15$  nm, and the average width was approximately of  $31 \pm 1.4$  nm.

PLL-DHBA films were fabricated by first dissolving PLL-HBr and DHBA into deionized water, forming aqueous solutions of PLL and DHBA with final concentrations of  $1 \text{ g L}^{-1}$  and  $5 \text{ g L}^{-1}$  respectively. Upon the dissolution of PLL-HBr in DI water, the amine group became protonated, forming cationic PLL. PLL was modified in the liquid state utilizing a Schiff base reaction with DHBA solution, using a 2:1 mass ratio of PLL to DHBA. The resulting solution obtained a yellow hue and was diluted with anhydrous ethanol, with a final concentration of 70% ethanol-30% water, for the fabrication of PLL-DHBA films using cathodic EPD.

### 5.3.2 Electrochemical Coating Fabrication

Ti foil was used as both the film substrate and cathode in the electrochemical cell set-up. Pt counter electrodes were located 15mm on either side of the Ti cathode. All coatings were deposited at 50 V, and pure PLL-DHBA films were fabricated. In addition to pure PLL-DHBA films, composite films containing hydroxyapatite (HA), rutile ( $\text{TiO}_2$ ) and a combination of both HA and  $\text{TiO}_2$  were fabricated using cathodic EPD. The concentration of HA or  $\text{TiO}_2$  nanoparticles dispersed in the PLL-DHBA solution was  $1 \text{ g L}^{-1}$ .

### **5.3.3 Coating Characterization**

A JEOL 7000 F scanning electron microscope (SEM) was used to characterize the surface coating morphology. Atomic force microscopy (AFM) was used to determine the surface roughness, and all measurements were carried out using a Bruker Bioscope Catalyst atomic force microscope. The area probed on each surface was equal to  $22.5 \text{ mm}^2$ , and the average roughness for each surface was calculated from this area. The sessile drop method was used to characterize the wettability of the PLL-DHBA coatings. An OCA 35 contact angle measuring device was used to conduct the experiment. To take a measurement, three microlitres of deionized water was dropped onto the sample surface and the contact angle on the left and right side of the drop was calculated immediately upon contact using the corresponding contact angle measurement software, SCA 20. Readings were taken from five different areas of the sample, and the average wetting angle was calculated from these measurements. Coating adhesion was measured according to the procedure outlined in ASTM standard D3359–09. An Aligent Carry 5000 spectrometer was used for ultraviolet-visible (UV–vis) spectroscopy measurements. PLL, DHBA, and PLL-DHBA dissolved in ethanol solution were analyzed in matching 10mm quartz cuvettes, using dual beam mode. Fourier transform infrared spectroscopy measurements were obtained using a Bruker Vertex 70 Spectrometer. A powder diffractometer equipped with a Rigaku Cu K $\alpha$  rotating anode and a Bruker SMART6000 CCD were used for X-ray diffraction experiments.

### **5.3.4 Cell Culturing**

Saos-2 cells were grown in McCoy's 5 A modified media in 15% fetal bovine serum and 1% penicillin/streptomycin. Cells were obtained from ATCC ® while other cell culture

reagents were obtained from Life Technologies Inc. Cells were maintained at 37 °C with 5% CO<sub>2</sub> and media was exchanged every 4 days. Once a confluent cell monolayer was obtained, cells were detached with trypsin in 0.25% ethylenediaminetetraacetic acid (EDTA). EPD film samples (15mm diameter) were placed in a 24 well plate and cells were plated at a density of 10,000 cells/cm<sup>2</sup>. All samples were sterilized under UV radiation for 15 min prior to cell seeding. Cells were counted using an Invitrogen Countess Automated Cell Counter. Cells grew on the surfaces of the films for 1 and 3 days. 5 samples were used for each film and time point combination. Methods were similar to those used in previous published work [16].

### **5.3.5 Cell Metabolism**

Cell metabolism was measured using an alamarBlue® dye obtained from Life Technologies Inc. alamarBlue®, or resazurin, is only converted to the fluorescent resorufin when it interacts with metabolizing cells which allows for it to be an indication of cellular activity. The pre-existing media was removed from each well and was subsequently replaced by 650 µL of a 5% alamarBlue solution (in McCoy's 5 A media). The samples were incubated in the dark for 1 h at 37 °C with 5% CO<sub>2</sub>. Fluorescence values were determined using a Tecan Infinite ® M1000 at 540–580 nm (excitation-emission). The blank reading was subtracted from each value to obtain the signal corresponding to the cells only. Following plate reading, the alamarBlue solution was removed and 300 µL of 0.1% triton lysis solution (in PBS) was added to each well in preparation for additional assays.

### **5.3.6 Alkaline Phosphatase Activity**

Alkaline phosphatase (ALP) activity was measured using the ALP assay from Abcam®. P-nitrophenol phosphate powder was dissolved in ALP assay buffer to prepare incubation solution. The phosphate group is cleaved off in the presence of alkaline phosphatase and the resulting p-nitrophenol emits light. 25  $\mu\text{L}$  of lysed cells in PBS was added to a 96 well plate, in triplicate, for each sample. Subsequently, 50  $\mu\text{L}$  of incubation solution was added to each well and the plate was incubated for 20 min in the dark at 37°C with 5%  $\text{CO}_2$ . Absorbance was read using a Tecan Infinite® M1000 at 405 nm. A standard curve was prepared using prescribed concentrations of p-nitrophenol as per Abcam instructions. The blank absorbance reading was subtracted from each data point and, via the standard curve, ALP activity was determined.

### **5.3.7 Statistical Analysis**

Statistical analysis was performed using the programming language, R, using a two-way ANOVA at a significance of  $\alpha=0.05$  and Tukey's HSD test was used to evaluate contrasts. All in vitro data was accepted to be normally distributed as per the Shapiro-Wilk test ( $p > 0.05$ ).

## **5.4 Results and Discussion**

In order to combine the advantageous properties of PLL, such as cell adhesion and proliferation, with the unique adhesive properties of catechol, we modified PLL with the catechol-containing molecule DHBA (Figure 5-1). The chemical structure of DHBA consists of a catechol group attached to an aldehyde, which makes it well suited for



attachment to the amine group via Schiff base reaction, building on our previous work with chitosan [11].

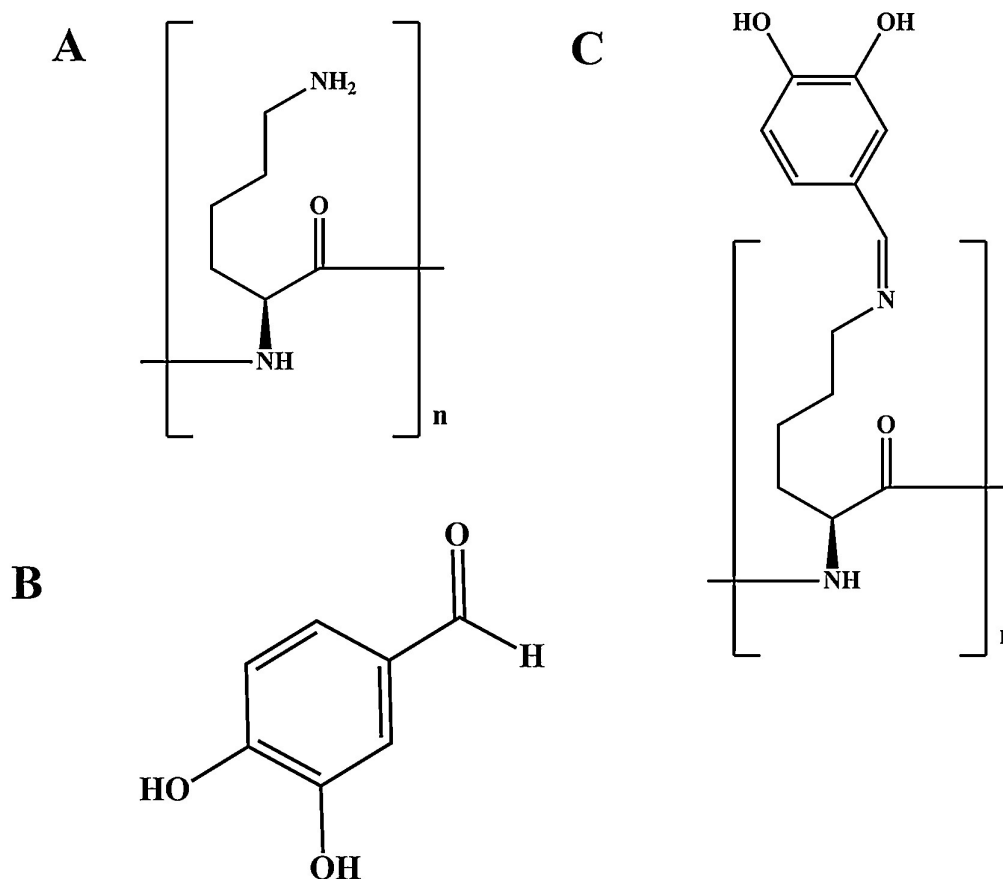


Figure 5-1. Chemical structure of (A) PLL, (B) DHBA and (C) PLL-DHBA.

In a Schiff base reaction, the amine group acts as a nucleophile and attacks the aldehyde group in DHBA. The nitrogen in the amine replaces the oxygen in the carbonyl group, and as a result the PLL monomer is modified with a catechol group. The chemical structure of the modified PLL monomer can be seen in Figure 5-1C. In the present work, PLL-DHBA films were fabricated using cathodic EPD, which is governed by the local pH increase at the electrode surface (described by Eq. (1)). The presence of a Schiff base was confirmed

using UV–vis and Fourier Transform Infrared (FTIR) spectroscopy, as features from both the PLL and DHBA spectra can be found in both the PLL-DHBA UV–vis and FTIR spectra (Figure 5-2 and Supporting Information Figure 5-S1). In the UV–vis spectra, the absorptions between 250 and 350 nm are characteristic of the catechol group in DHBA [17].

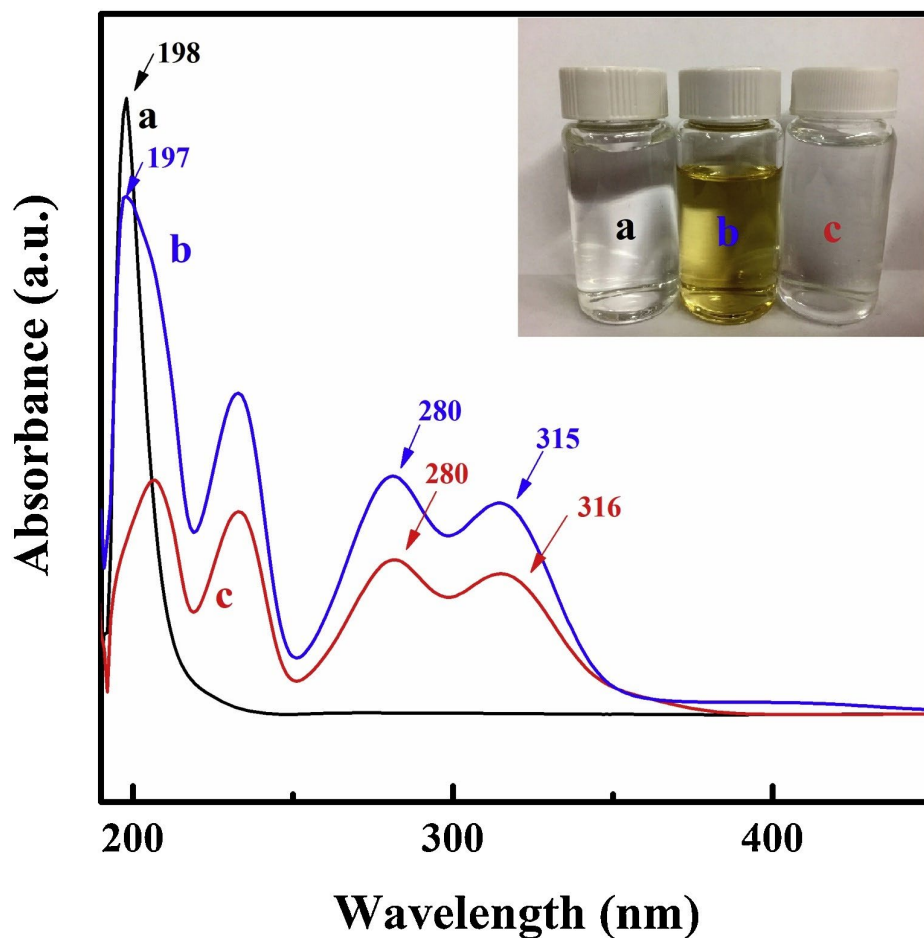


Figure 5-2: UV–vis spectra of (a) PLL, (b) DHBA and (c) PLL-DHBA. Insert: (a) pure PLL, (b) PLL-DHBA, and (c) pure DHBA in solution.

These characteristic catechol adsorptions are not found in the pure PLL spectra but can be found in the spectra of PLL-DHBA, which is indicative that PLL monomers were successfully modified with DHBA. The PLL-DHBA spectrum also contains a large absorption with a maxima around 197 nm, which is also found in the pure PLL spectra [18] and indicates that both PLL and DHBA are present. The FTIR spectra also confirmed modification of the PLL monomer with catechol, as it revealed characteristic absorbances at approximately 2854 and 2921  $\text{cm}^{-1}$  from DHBA in accordance with the manufacturer's specifications. Characteristic absorbances from the pure poly-L-lysine spectra were also observed, such as NH and C=O at 1530 and 1650  $\text{cm}^{-1}$ , respectively [4]. The presence of Schiff base formation is also indicated by a solution colour change, from clear to yellow (Figure 5-2 inset).

Past experiments have found that catechol-containing molecules allow for superior adsorption to the surface of metal, metal oxide and hydroxide particles [19]. Superior coating adhesion was also observed in the present study, with all coatings achieving 5B classification according to the ASTM D3359–09 Tape Test, which is the highest level of adhesion (Supporting Information, Figure 5-S2). The adsorption of catechol is not only advantageous for increasing coating adhesion, but also for the fabrication of composite coatings using EPD, because the adsorbed organic molecule imparts an electric charge to the particles. This allows for improved dispersion via electrosteric repulsion. It has been suggested that the mechanism of catechol adsorption on metal oxide or hydroxide particles involves interaction between the hydroxyl groups of the catechol moiety and metallic atoms on the inorganic particle surface [19]. It can be inferred that a similar adsorption mechanism

is at play between PLL-DHBA and Ca or Ti atoms in the HA or TiO<sub>2</sub> nanoparticle surface. Catechol adsorption has two possible configurations: bridging or chelating. A schematic diagram of these two adsorption configurations of PLL-DHBA and either Ca or Ti can be found in Figure 5-S3 in the supporting information. In the present study, the functionalization of PLL with DHBA allowed for catecholate bonding, which resulted in improved adsorption of PLL-DHBA on the HA or TiO<sub>2</sub> particle surface. PLL-DHBA was used as a dispersing, charging, and film forming agent. Thick composite films, containing HA, TiO<sub>2</sub>, or both HA and TiO<sub>2</sub> were deposited. XRD was used to confirm co-deposition of HA and TiO<sub>2</sub>, and X-ray diffraction patterns of PLL-DHBA-HA, PLL-DHBA-TiO<sub>2</sub>, and PLL-DHBA-HA-TiO<sub>2</sub> can be seen in Figure 5-3. Sharp peaks were observed for both HA and TiO<sub>2</sub>, which confirmed the fabrication of the coating containing both bioceramics.

Many efforts have been made to develop organic-inorganic nano- composite coatings to improve the osseointegration of orthopaedic implant materials via the incorporation of bioactive bioceramic materials, but it is also known that the surface roughness and contact angle also have a strong effect [20]. It has been found previously that lower contact angles, and thus greater hydrophilicity, and increased surface roughness of biomedical implant coatings improves osseointegration [20]. More recently it has been determined that surface topography has a strong influence on osteoblast adhesion and proliferation, and that a dual scale topography, one that includes both nano- and microscale features is optimal for promoting osteoblast adhesion [21–23]. A variety of treatments have been used previously to introduce nano-scale roughness to previously fabricated micro-scale features, including electrochemical etching, sand-blasting and acid-etching [21].

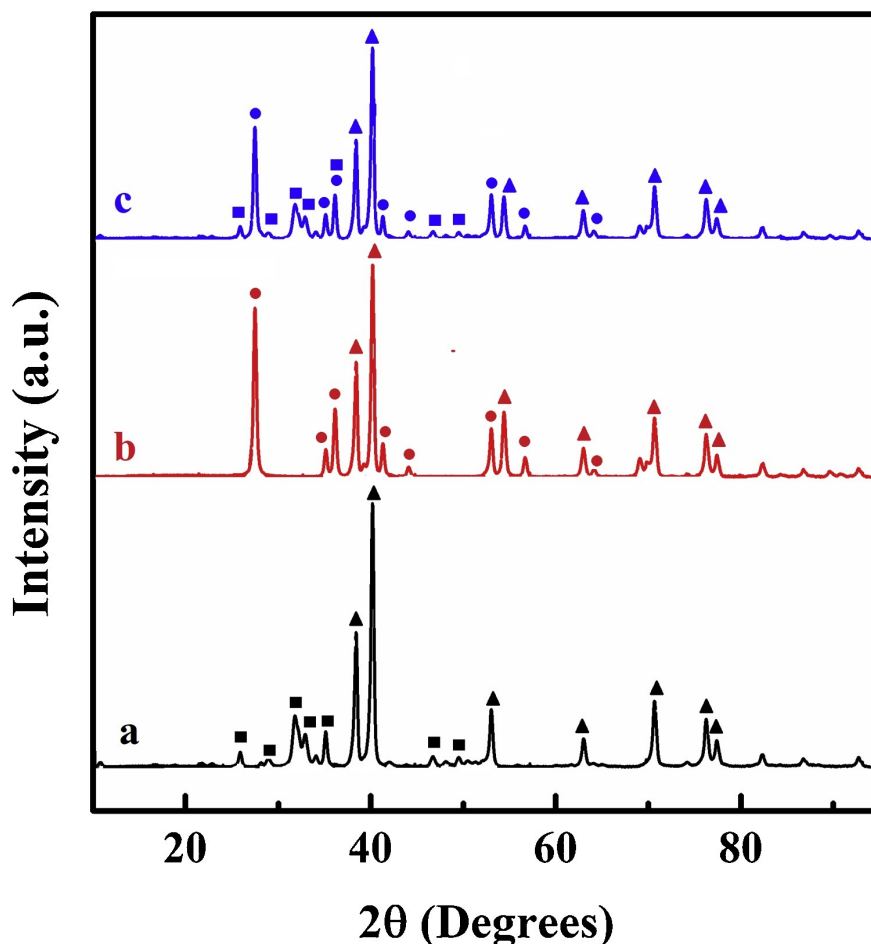


Figure 5-3: X-ray diffraction patterns for (a) PLL-DHBA-HA, (b) PLL-DHBA-TiO<sub>2</sub> and (c) PLL-DHBA-HA-TiO<sub>2</sub>, (■ – corresponds to JCPDS file 00-024-0033 for HA, ● – corresponds to JCPDS file 01-089-0553 TiO<sub>2</sub>, and ▲ – corresponds to JCPDS file 00-044-1294 for Ti substrate).

In the present study, we have obtained dual scale topography in one step (Figure 5-4). As can be seen in the low-magnification SEM images, all coatings exhibited micro-scale “clusters” of HA, TiO<sub>2</sub> or HA and TiO<sub>2</sub> nanoparticles within the PLL-DHBA matrix (Figure 5-4A and B for HA coatings, supporting information Figure 5-S4 for all other coatings). At higher magnification, we can see in the SEM images that the nanoparticles

are well-dispersed within the PLL-DHBA matrix and thus provide features at both the nano- and micro-scale for cell interaction.

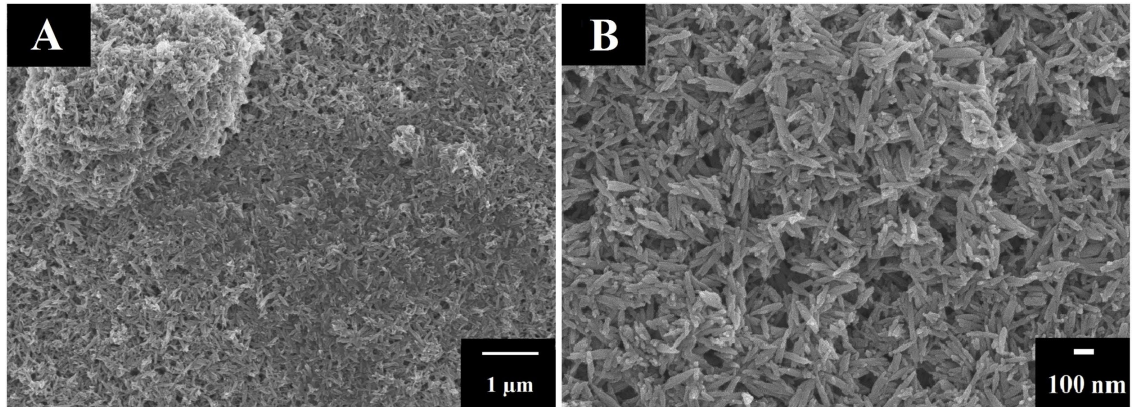


Figure 5-4: SEM images of PLL-DHBA-HA coatings at (A) low and (B) high magnification, exhibiting dual-scale topography.

AFM was used to further study the surface morphology of the PLL-DHBA-HA, PLL-DHBA-TiO<sub>2</sub> and PLL-DHBA-HA-TiO<sub>2</sub> coatings. Three-dimensional reconstructions of the surface can be found in Figure 5-5. It can be seen from the surface reconstructions that all coatings exhibited topography on the micrometer scale. The average surface roughness results can be found in Table 5-1. PLL-DHBA-HA-TiO<sub>2</sub> exhibited the greatest average roughness, followed by PLL-DHBA-TiO<sub>2</sub> and PLL-DHBA-HA. It has been reported that the optimal average roughness for dental implant surfaces lies within 0.5 µm and 1.0 µm [20], the average roughness of all composite films fell within this range, with the exception of PLL-DHBA-HA-TiO<sub>2</sub>.

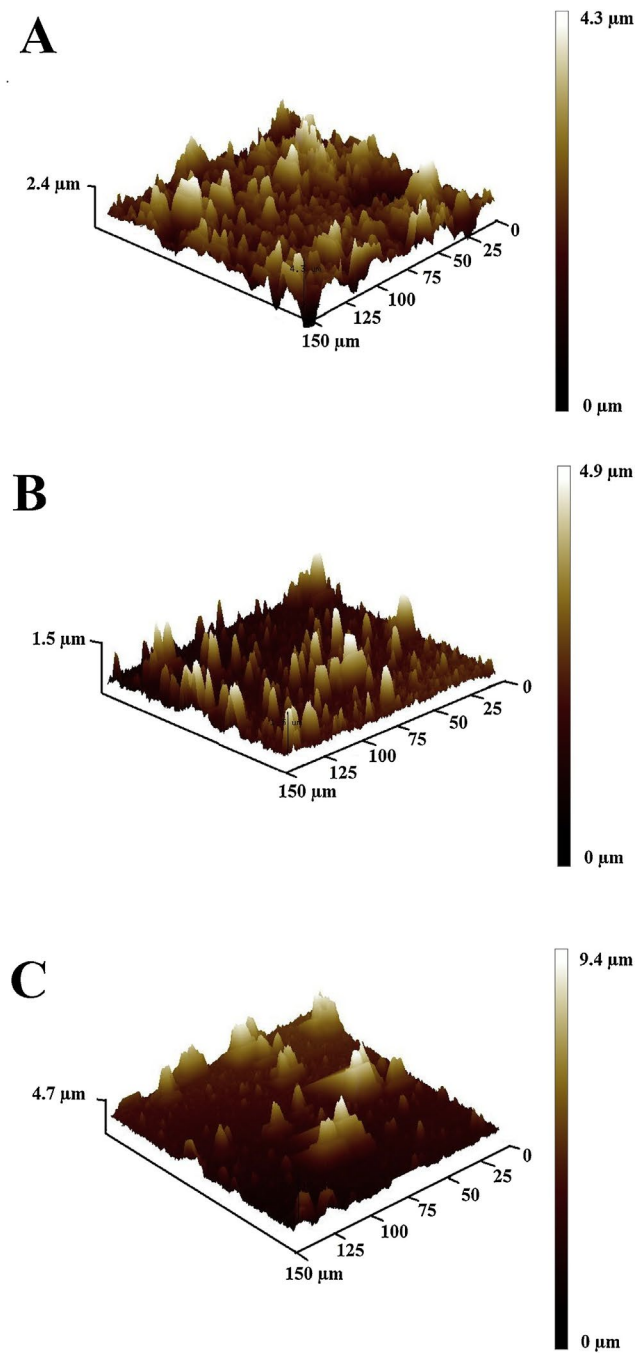


Figure 5-5: AFM results for (A) PLL-DHBA-HA, (B) PLL-DHBA-TiO<sub>2</sub> and (C) PLL-DHBA-HA-TiO<sub>2</sub>. PLL-DHBA-HA-TiO<sub>2</sub> exhibited the greatest surface roughness, followed by PLL-DHBA-HA and then PLL-DHBA-TiO<sub>2</sub>.

These results combined with SEM characterization confirmed that we achieved the desired dual-scale topography for all three coatings. We hypothesize that this unique surface topography was achieved in one-step due to our choice of relatively high deposition voltage. Previous investigations by our group used a deposition voltage of 10 V for the fabrication of pure PLL-HA composite films, and smooth, uniform films were achieved [13]. This is in sharp contrast to the films that were fabricated in this study, which used a deposition voltage of 50 V and exhibited rough surface topography. In a previous study, it was discovered that the coating porosity of pure HA increased with increasing voltage when deposited using EPD [15]. When low voltages were used for deposition, it resulted in the preferred deposition of small particles, but a larger range of particle sizes were deposited at higher voltages [15]. Coatings with greater porosity were also achieved at higher voltages. These changes in surface morphology and particle size, that were observed with an increase in voltage, can be attributed to the tendency of particles to partially agglomerate with the application of a stronger electric field, as well as the increased hydrogen evolution at the cathode surface [15]. In addition to exhibiting surface roughness and dual-scale topography, the surface wettability must also be increased in order to promote cell proliferation and adhesion [20]. Simultaneously increasing the surface roughness and wettability has proved challenging, as techniques such as acid-etching and grit-blasting have been found to greatly increase hydrophobicity in titanium dental implant materials [24]. It is hypothesized that this increase in contact angle was a result of air trapped below the wetting liquid, and a variety of additional surface modification techniques have been developed to decrease the contact angle while maintaining surface roughness, such as



modification with polyelectrolytes, plasma or alkaline surface treatments [24]. Contact angle measurements determined that the presence of inorganic nanoparticles increased the wettability of PLL-DHBA (Supporting Information Figure 5-S5 and Table 5-1). PLL-DHBA-HA exhibited the smallest contact angle, followed by PLL-DHBA-TiO<sub>2</sub> and PLL-HA-TiO<sub>2</sub>. The observed decrease in contact angle following the addition of ceramic nanoparticles could be attributed to the subsequent increase in porosity, compared to pure PLL-DHBA. This effect was observed comparing in the literature when characterizing alginate/bioglass® coatings, and it was realized that coatings with micron-sized pores and high porosity achieve increased surface wettability, since the water droplet can more easily penetrate the coating structure [25].

**Table 5-1:** Comparison of average contact angles and average roughness for PLL-DHBA coatings

| Coating                      | Average Contact Angle (°) | Average Roughness (μm) |
|------------------------------|---------------------------|------------------------|
| PLL-DHBA                     | 53.8 ± 5                  | 0.046 ± 0.02           |
| PLL-DHBA-HA                  | 20.8 ± 10                 | 0.900 ± 0.06           |
| PLL-DHBA-TiO <sub>2</sub>    | 33.8 ± 4                  | 0.942 ± 0.04           |
| PLL-DHBA-HA-TiO <sub>2</sub> | 47.8 ± 9                  | 1.21 ± 0.10            |

In a previous study that measured the relationship between wettability, protein absorption and cell adhesion, it was found that the optimal contact angle range lies between 30-60° [24]. The contact angles of all our bioceramic-containing coatings measured in this study had an average contact angle within this optimal range, with the exception of the

PLL-DHBA-HA coatings, which had an average contact angle slightly below this threshold.

The cell metabolism results are shown in Figure 5-6A which approximate fluorescence to cell metabolism. For all EPD films, the cell metabolism increased in magnitude from 1 to 3 days, however, this was only statistically significant for the PLL-DHBA-TiO<sub>2</sub> film ( $p < 0.05$ ). Additionally, at the 3-day time point, the PLL-DHBA-TiO<sub>2</sub> film showed significantly increased metabolism compared to both the PLL-DHBA-HA and PLL-DHBA-HA-TiO<sub>2</sub> films ( $p < 0.05$ ).

Alkaline phosphatase activity, Figure 5-6B, was shown, similar to cell metabolism, to increase in magnitude from 1 to 3 days for both the PLL-DHBA-TiO<sub>2</sub> and PLL-DHBA-HA-TiO<sub>2</sub> films. Similar to cell metabolism, the PLL-DHBA-TiO<sub>2</sub> film showed a statistically significant increase from 1 to 3 days ( $p < 0.05$ ) and at 3 days had more ALP activity than both PLL-DHBA-HA and PLL-DHBA-HA-TiO<sub>2</sub> films ( $p < 0.05$ ). Overall, the effects observed in ALP activity correspond directly to cell metabolism results. *In vitro* results demonstrated that the EPD films did not have noticeable cytotoxic effects when considering cell metabolism and alkaline phosphatase activity. The PLL-DHBA-TiO<sub>2</sub> film showed improved cell metabolism and alkaline phosphatase activity than both the PLL-DHBA-HA and PLL-DHBA-HA-TiO<sub>2</sub> films at 3 days and was the only film to show a statistically significant increase from 1 to 3 days. Previous studies have suggested that nanoscale HA particles may have cytotoxic effects which may be a contributing reason for the lack of statistically significant changes for the EPD films containing HA [26,27].

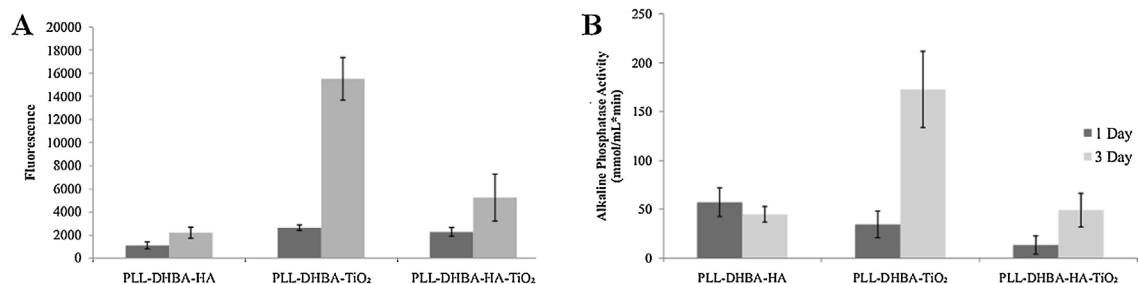


Figure 5-6: (A) Cell metabolism results for EPD films at 1 and 3-day time points. Cell metabolism showed significant increases from 1 to 3 days for the PLL-DHBA-TiO<sub>2</sub> film only ( $p < 0.05$ ). Additionally, the PLL-DHBA-TiO<sub>2</sub> film demonstrated significantly greater cell metabolism at 3 days compared to the other EPD films. Errors bars represent standard deviation. (B) ALP activity results for EPD films at 1 and 3-day time points. ALP activity showed significant increases from 1 to 3 days for the PLL-DHBA-TiO<sub>2</sub> film only ( $p < 0.05$ ). The PLL-DHBA-TiO<sub>2</sub> film demonstrated significantly greater ALP activity at 3 days compared to the other EPD films ( $p < 0.05$ ).

The HA nanorods used in the films had an average width of  $31 \pm 1.4$  nm, and an average length of  $169 \pm 15$  nm. Other authors have found that similar sized nanorods were relatively non-cytotoxic [28]. However, despite these concerns, the films containing HA were not cytotoxic as demonstrated by the maintained cell metabolism and ALP activity results. HA films and deposition have a history of being successfully used in biomaterials with success, so it is possible that the observation period was too short to elucidate the response of the HA films [29,30]. As a preliminary *in vitro* analysis, it could be concluded that the PLL-DHBA-TiO<sub>2</sub> film performed better than the other films. TiO<sub>2</sub> particles and films have both demonstrated improved response from bone cells in the past which is agreeable with the results of this study [31,32]. This is supported by the contact angle data which shows that the films are hydrophilic which is generally considered beneficial for

early biomaterial tissue interactions [31]. The sub-micron roughness of the surface, contributed from both meso- and nanoparticles, matches previous studies which support the use of dual-topographies in implant-based materials [33–35]. Going forward, additional studies using longer time points, alternative cell lines and perhaps in vivo work will be necessary to understand the cellular responses to these dual-topography EPD films.

## 5.5 Conclusions

For the first time we demonstrate a novel one-step fabrication technique for the development of catechol-modified PLL nanocomposite films that exhibit dual nano- and micro-scale topography with high wettability. Our modification technique utilizes a Schiff base reaction to modify L-lysine monomers with a catechol group, using the catechol containing DHBA molecule. This new method allows for the co-deposition of both HA and TiO<sub>2</sub>, combining the bioactivity of HA with the biocompatibility and stability of TiO<sub>2</sub>. Our new strategy for co-dispersion and deposition is based on biomimetic catecholate type bonding, which significantly increases adhesion compared to pure PLL which exhibits weak adsorption to inorganic particles. This technique also achieves dual-scale topography in one-step, with the use of cathodic electrophoretic deposition at a relatively high voltage (50 V). All composite coatings fabricated were found to be hydrophilic in addition to exhibiting high surface roughness, which is advantageous for osteoblast attachment and proliferation. *in vitro* testing revealed that all coatings studied were not cytotoxic and showed an increase in cell metabolism as well as alkaline phosphatase activity in the

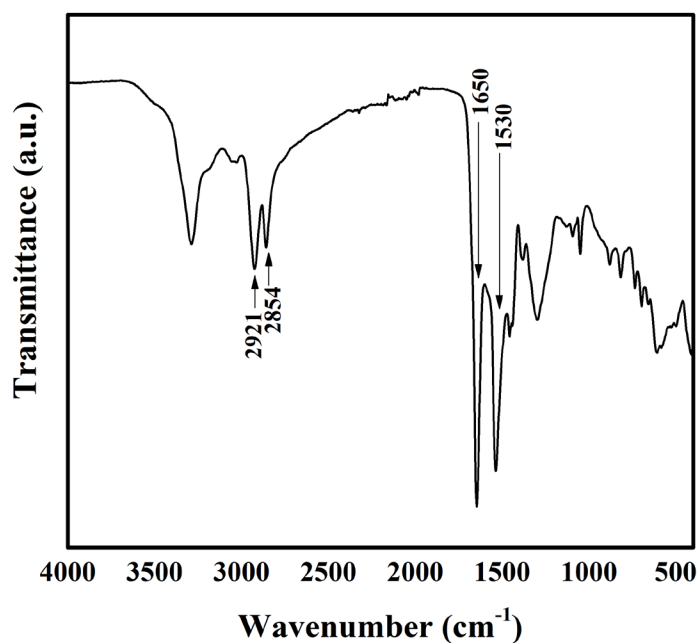
studied time period. This work paves the way for the next generation of biomedical implants with improved osseointegration and increased lifespan.

## 5.6 Acknowledgements

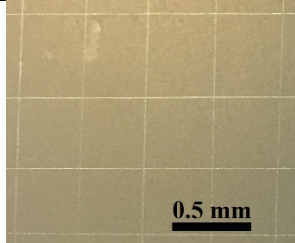
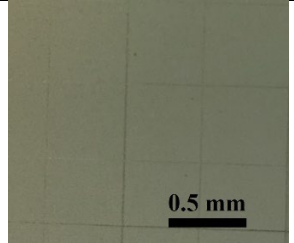
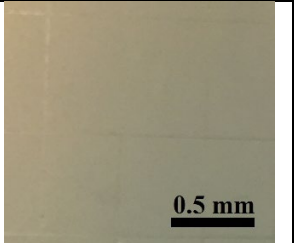
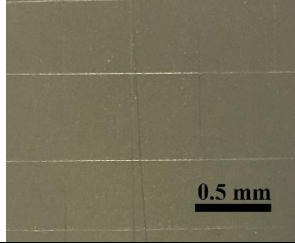
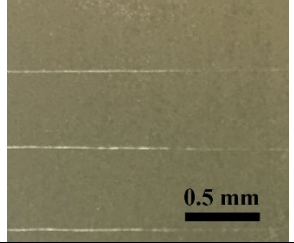
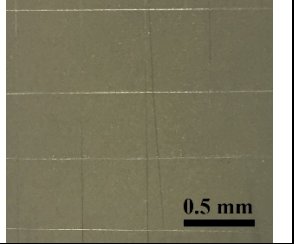
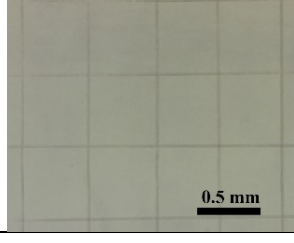
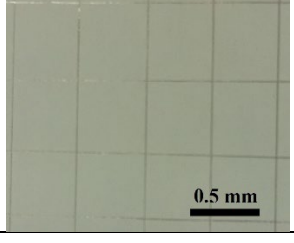
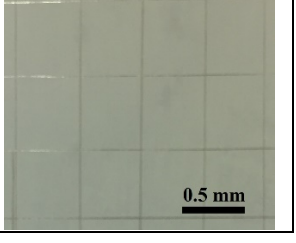
The authors gratefully acknowledge the Natural Sciences and Engineering Research Council of Canada for the financial support and Biointerfaces Institute of McMaster University for the cell studies.

## 5.7 Appendix A. Supplementary Data

**Figure 5-S1:** FTIR spectrum of PLL-DHBA.



**Figure 5-S2:** Representative images of PLL-DHBA coatings after adhesive tape test.

| Coating                      | Sample No.   |   |  |
|------------------------------|--|---|--|
|                              | 1  | 2   | 3  |
| PLL-DHBA-HA                  |   |   |   |
| PLL-DHBA-TiO <sub>2</sub>    |   |   |   |
| PLL-DHBA-HA-TiO <sub>2</sub> |  |  |  |

**Figure 5-S3:** Chemical adsorption of PLL-DHBA involving interactions with metal ions (M) on the inorganic particle surface: (A) bridging and (B) chelating bonding.

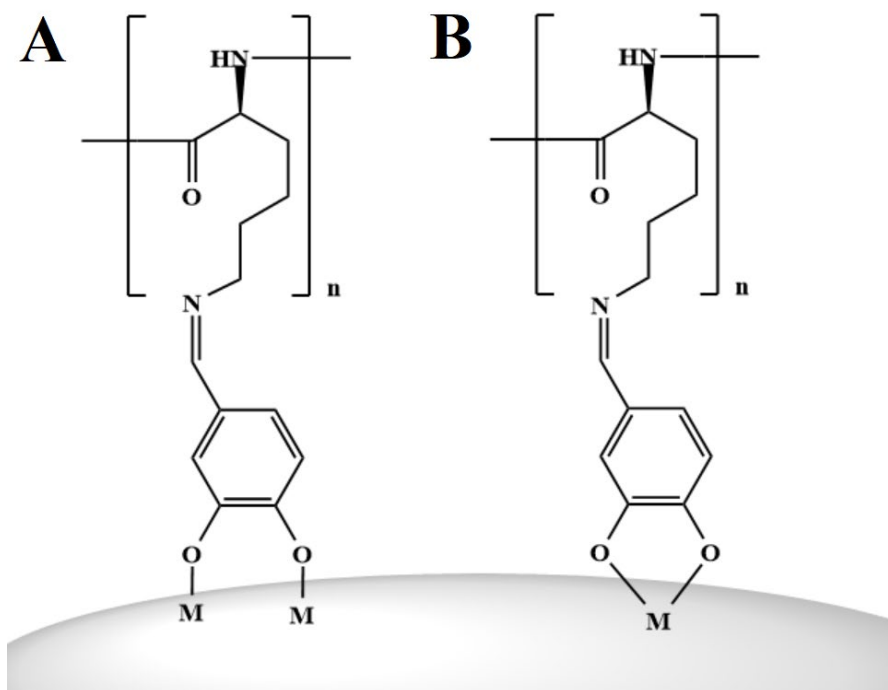


**Figure 5-S4:** SEM images of (A,B) PLL-DHBA-TiO<sub>2</sub> and (C,D) PLL-DHBA-HA-TiO<sub>2</sub> coatings at low and high magnification, exhibiting dual-scale topography.

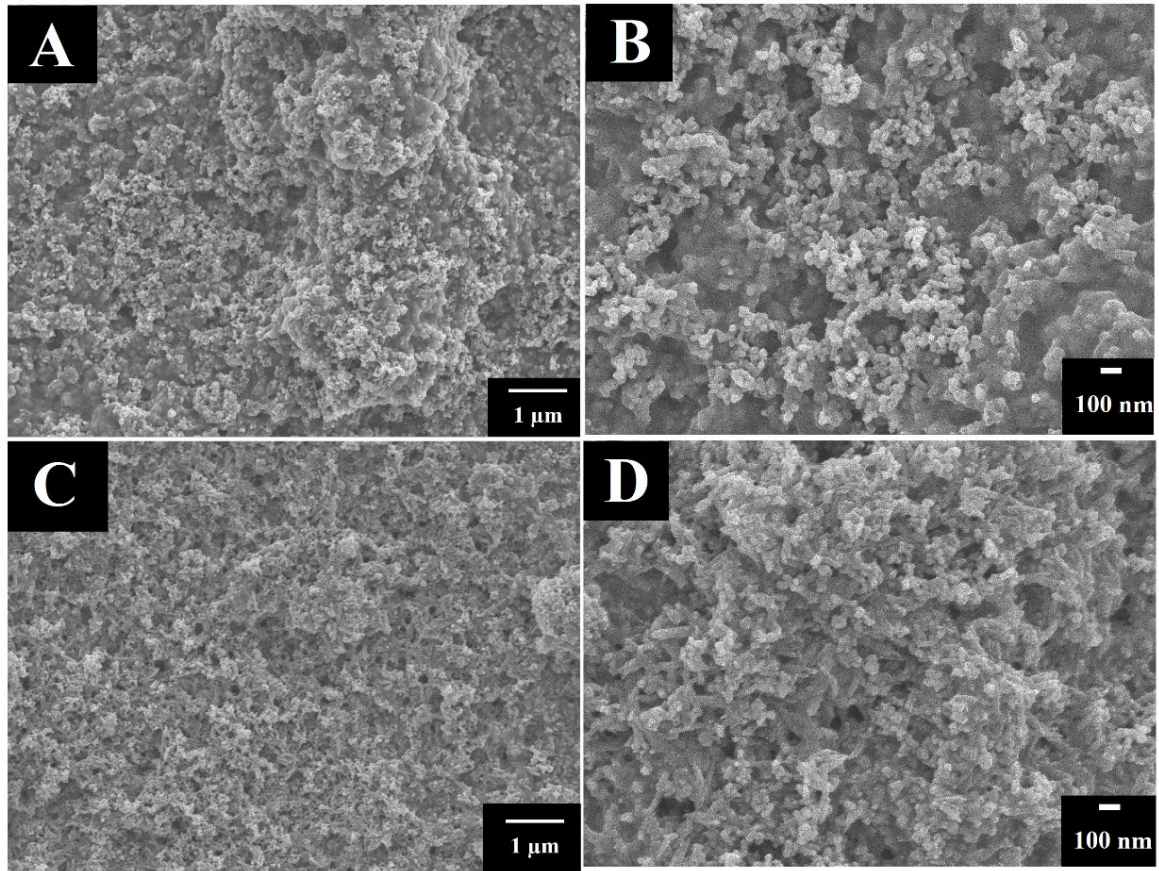
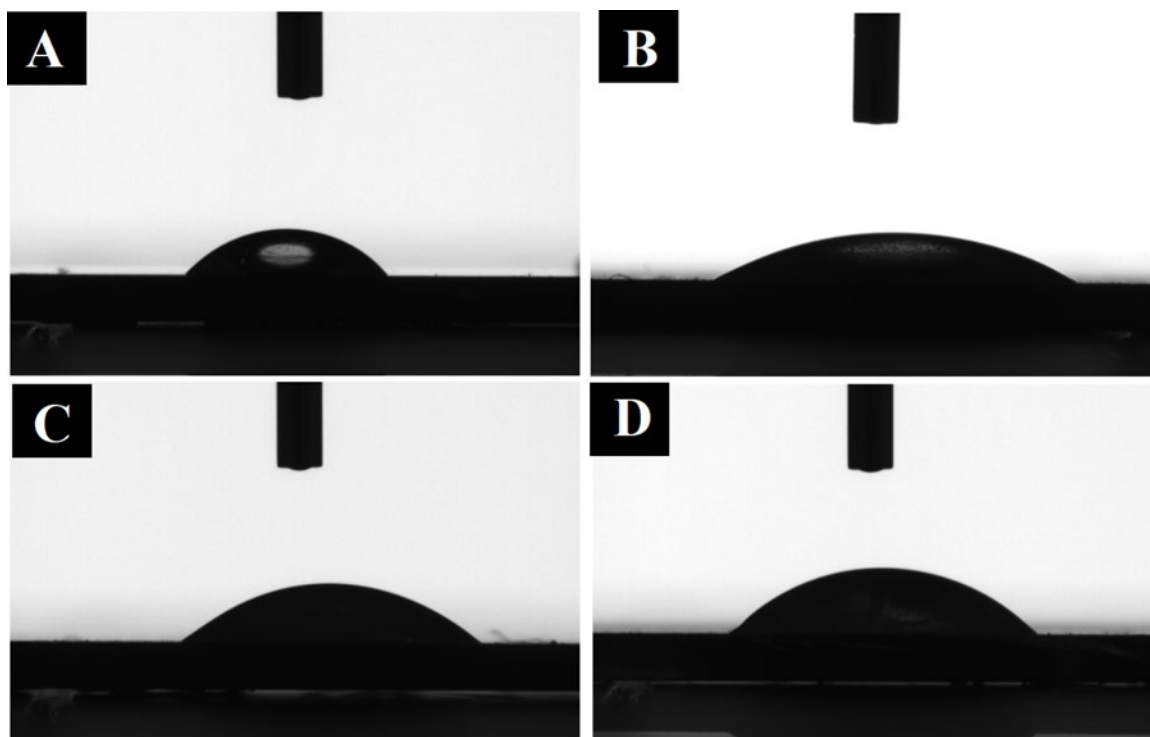




**Figure 5-S5:** Contact angle results for (A) PLL-DHBA, (B) PLL-DHBA-HA, (C) PLL-DHBA-TiO<sub>2</sub>, and (D) PLL-DHBA-HA-TiO<sub>2</sub>. All coatings were hydrophilic, but PLL-DHBA-HA exhibited the greatest hydrophilicity, followed by PLL-DHBA-TiO<sub>2</sub>, PLL-DHBA-HA-TiO<sub>2</sub>, and PLL-DHBA.



## 5.8 References

- [1] N. Sahiner, Single step poly(L-Lysine) microgel synthesis, characterization and biocompatibility tests, *Polymer (United Kingdom)* 121 (2017) 46–54.
- [2] Z. Tan, T. Bo, F. Guo, J. Cui, S. Jia, Effects of  $\epsilon$ -Poly-L-lysine on the cell wall of *Saccharomyces cerevisiae* and its involved antimicrobial mechanism, *Int. J. Biol. Macromol.* 118 (Part B) (2018) 2230–2236.
- [3] G. Sun, Q. Yang, A. Zhang, J. Guo, X. Liu, Y. Wang, Q. Ma, Synergistic effect of the combined bio-fungicides  $\epsilon$ -poly-L-lysine and chitooligosaccharide in controlling grey mould (*Botrytis cinerea*) in tomatoes, *Int. J. Food Microbiol.* 276 (2018) 46–53.

- [4] M. Kouhi, M. Fathi, M.P. Prabhakaran, M. Shamanian, S. Ramakrishna, Poly L lysine-modified PHBV based nanofibrous scaffolds for bone cell mineralization and osteogenic differentiation, *Appl. Surf. Sci.* 457 (2018) 616–625.
- [5] M. Mekhail, K. Jahan, M. Tabrizian, Genipin-crosslinked chitosan/poly-l-lysine gels promote fibroblast adhesion and proliferation, *Carbohydr. Polym.* 108 (2014) 91–98.
- [6] X. Wang, H. Zhang, H. Jing, L. Cui, Highly efficient labeling of human lung Cancer cells using cationic Poly-l-lysine-Assisted magnetic Iron oxide nanoparticles, *Nano- Micro Lett.* 7 (2015) 374–384.
- [7] H. Jin, Y. Yu, W.B. Chrisler, Y. Xiong, D. Hu, C. Lei, Delivery of microRNA-10b with polylysine nanoparticles for inhibition of breast cancer cell wound healing, *Breast Cancer Basic Clin. Res.* 5 (2011) 9–19.
- [8] L. Li, H. Zeng, Marine mussel adhesion and bio-inspired wet adhesives, *Biotribology* 5 (2016) 44–51.
- [9] J. Hyun, S. Hong, H. Lee, *Acta Biomaterialia* Bio-inspired adhesive catechol-conjugated chitosan for biomedical applications : a mini review, *Acta Biomater.* 27 (2015) 101–115.
- [10] T.E. Winkler, H. Ben-Yoav, S.E. Chocron, E. Kim, D.L. Kelly, G.F. Payne, R. Ghodssi, Electrochemical study of the catechol-modified chitosan system for clozapine treatment monitoring, *Langmuir* 30 (2014) 14686–14693.
- [11] A. Clifford, X. Pang, I. Zhitomirsky, Biomimetically modified chitosan for electrophoretic deposition of composites, *Colloids Surfaces A Physicochem*, 544 (2018) 28–34.
- [12] A.R. Boccaccini, S. Keim, R. Ma, Y. Li, I. Zhitomirsky, Electrophoretic deposition of biomaterials, *J. R. Soc. Interface* 7 (2010) S581–S613.
- [13] Y. Wang, X. Pang, I. Zhitomirsky, Electrophoretic deposition of chiral polymers and composites, *Colloids Surf. B Biointerfaces* 87 (2011) 505–509.
- [14] A. Szcześ, L. Hołysz, E. Chibowski, Synthesis of hydroxyapatite for biomedical applications, *Adv. Colloid Interface Sci.* 249 (2017) 321–330.

- [15] I. Zhitomirsky, L. Gal-Or, Electrophoretic deposition of hydroxyapatite, *J. Mater. Sci. Mater. Med.* 8 (1997) 213–219.
- [16] B.E.J. Lee, H. Exir, A. Weck, K. Grandfield, Characterization and evaluation of femtosecond laser-induced sub-micron periodic structures generated on titanium to improve osseointegration of implants, *Appl. Surf. Sci.* 441 (2018) 1034–1042.
- [17] M. Andjelković, J. Van Camp, B. De Meulenaer, G. Depaemelaere, C. Socaciu, M. Verloo, R. Verhe, Iron-chelation properties of phenolic acids bearing catechol and galloyl groups, *Food Chem.* 98 (2006) 23–31.
- [18] C. Shan, H. Yang, D. Han, Q. Zhang, A. Ivaska, L. Niu, Water-soluble graphene covalently functionalized by biocompatible poly-L-lysine, *Langmuir* 25 (2009) 12030–12033.
- [19] M.S. Ata, Y. Liu, I. Zhitomirsky, A review of new methods of surface chemical modification, dispersion and electrophoretic deposition of metal oxide particles, *RSC Adv.* 4 (2014) 22716–22732.
- [20] C.N. Elias, Y. Oshida, J.H.C. Lima, C.A. Muller, Relationship between surface properties (roughness, wettability and morphology) of titanium and dental implant removal torque, *J. Mech. Behav. Biomed. Mater.* 1 (2008) 234–242.
- [21] K. Gulati, M. Prideaux, M. Kogawa, L. Lima-Marques, G.J. Atkins, D.M. Findlay, D. Losic, Anodized 3D–printed titanium implants with dual micro- and nano-scale topography promote interaction with human osteoblasts and osteocyte-like cells, *J. Tissue Eng. Regen. Med.* 11 (2017) 3313–3325.
- [22] I.J. Macha, B. Ben-Nissan, J. Santos, S. Cazalbou, A. Stamboulis, D. Grossin, G. Giordano, Biocompatibility of a new biodegradable polymer-hydroxyapatite composite for biomedical applications, *J. Drug Deliv. Sci. Technol.* 38 (2017) 72–77.
- [23] B.E.J. Lee, S. Ho, G. Mestres, M. Karlsson Ott, P. Koshy, K. Grandfield, Dual-topography electrical discharge machining of titanium to improve biocompatibility, *Surf. Coatings Technol.* 296 (2016) 149–156.

- [24] F. Rupp, L. Liang, J. Geis-Gerstorfer, L. Scheideler, F. Hüttig, Surface characteristics of dental implants: a review, *Dent. Mater.* 34 (2018) 40–57.
- [25] Q. Chen, L. Cordero-Arias, J.A. Roether, S. Cabanas-Polo, S. Virtanen, A.R. Boccaccini, Alginate/Bioglass® composite coatings on stainless steel deposited by direct current and alternating current electrophoretic deposition, *Surf. Coat. Technol.* 233 (2013) 49–56.
- [26] X. Zhao, S. Ng, B.C. Heng, J. Guo, L. Ma, T.T.Y. Tan, K.W. Ng, S.C.J. Loo, Cytotoxicity of hydroxyapatite nanoparticles is shape and cell dependent, *Arch. Toxicol.* 87 (2013) 1037–1052.
- [27] M. Motskin, D.M. Wright, K. Muller, N. Kyle, T.G. Gard, A.E. Porter, J.N. Skepper, Hydroxyapatite nano and microparticles: correlation of particle properties with cytotoxicity and biostability, *Biomaterials* 30 (2009) 3307–3317.
- [28] J. Scheel, S. Weimans, A. Thiemann, E. Heisler, M. Hermann, Exposure of the murine RAW 264.7 macrophage cell line to hydroxyapatite dispersions of various composition and morphology: assessment of cytotoxicity, activation and stress response, *Toxicol. In Vitro* 23 (2009) 531–538.
- [29] R.M.G. Rajapakse, W.P.S.L. Wijesinghe, M.M.M.G.P.G. Mantilaka, K.G. Chathuranga Senarathna, H.M.T.U. Herath, T.N. Premachandra, C.S.K. Ranasinghe, R.P.V.J. Rajapakse, M. Edirisinghe, S. Mahalingam, I.M.C.C.D. Bandara, S. Singh, Preparation of bone-implants by coating hydroxyapatite nanoparticles on self-formed titanium dioxide thin-layers on titanium metal surfaces, *Mater. Sci. Eng. C.* 63 (2016) 172–184.
- [30] H. Zhou, J. Lee, Nanoscale hydroxyapatite particles for bone tissue engineering, *Acta Biomater.* 7 (2011) 2769–2781.
- [31] T. Shinonaga, M. Tsukamoto, A. Nagai, K. Yamashita, T. Hanawa, N. Matsushita, G. Xie, N. Abe, Cell spreading on titanium dioxide film formed and modified with aerosol beam and femtosecond laser, *Appl. Surf. Sci.* 288 (2014) 649–653.

- [32] H. Te Chen, H.Y. Shu, C.J. Chung, J.L. He, Assessment of bone morphogenic protein and hydroxyapatite-titanium dioxide composites for bone implant materials, *Surf. Coatings Technol.* 276 (2015) 168–174.
- [33] K. Grandfield, Bone, implants, and their interfaces, *Phys. Today* 68 (2015) 40–45,
- [34] C. Eriksson, H. Nygren, K. Ohlson, Implantation of hydrophilic and hydrophobic titanium discs in rat tibia: Cellular reactions on the surfaces during the first 3 weeks in bone, *Biomaterials* 25 (2004) 4759–4766.
- [35] F.A. Shah, B. Nilson, R. Brånemark, P. Thomsen, A. Palmquist, The bone-implant interface - nanoscale analysis of clinically retrieved dental implants, *Nanomedicine Nanotechnology, Biol. Med.* 10 (2014) 1729–1737.

**Chapter 6: Aqueous electrophoretic deposition of drugs using bile acids as solubilizing, charging and film-forming agents**

A. Clifford and I. Zhitomirsky

Materials Letters

Volume 227, pp. 1-4

15 September 2018

Reprinted with permission. © 2018 Elsevier

## **6.1 Abstract**

A new electrophoretic deposition (EPD) technique is reported for the fabrication of composite coatings containing drugs, which have low solubility in water. We present a conceptually new approach, which is based on the use of bile salts (BS) as solubilizing, charging and film forming agents. Composite films were obtained using tetracycline and ibuprofen as model drugs with commercial BS, such as cholic acid sodium salt and deoxycholic acid sodium salt. The suggested mechanism involves solubilization of drugs in BS solutions, followed by the formation of mixed charged micelles, containing drugs and charged BS, which allow electrophoretic transport of the drugs to the electrode surface. The EPD mechanism involves a pH decrease at the anode surface, protonation of carboxylic groups of BS and formation of water insoluble films. This approach can be used for deposition of other functional organic molecules and inorganic nanoparticles.

## **6.2 Introduction**

Electrophoretic deposition (EPD) has recently attracted attention for the fabrication of drug-containing composite coatings [1]. Using this technique, antibiotic loaded polymer microsphere-alginate antibacterial coatings [2] have been prepared. In another strategy, tetracycline hydrochloride loaded halloysite nanotubes were co-deposited with chitosan [3]. Polymer and ceramic particles are increasingly being explored for encapsulation of drugs and EPD of composites [1]. The encapsulation techniques are especially attractive for the EPD of composite coatings, which contain various drugs that exhibit low solubility in water.

Here we propose another strategy for the EPD of such drugs, which is based on the use of BS for drug solubilization in aqueous solutions. It is known [4] that BS are powerful natural detergents, which solubilize vitamins, cholesterol, lipids and other organic molecules. The solubility of cholesterol in water increased more than million-fold in the presence of BS [5]. The ability of BS to solubilize drugs and form mixed micelles is of particular importance for drug delivery [4–6]. The use of BS in drug formulations has allowed for improved drug transport through paracellular and transcellular routes, facilitated drug penetration and absorption [7]. The formation of mixed BS-drug micelles protected drugs from degradation, allowed for organ-specific action and facilitated drug penetration to deeper tissues [7]. Of particular interest are applications of BS for the development of anticancer drug formulations [7]. Moreover, BS exhibit unique gel-forming properties [8], which are currently under intensive investigation for the fabrication of composite scaffolds for controlled drug delivery. In our previous investigations we developed EPD strategies and mechanisms for deposition of films from BS solutions [8–10]. Further development of such strategies is promising for the EPD of composite films, containing drugs.

The goal of this investigation was to use EPD for the fabrication of drug-containing composite films, using BS as solubilizing, charging and film forming agents. We selected tetracycline (TC) and ibuprofen (IB) as model drugs, due to their low solubility in water and commercially available BS, such as cholic acid sodium salt (ChNa) and deoxycholic acid sodium salt (DChNa).



### 6.3 Experimental Procedures

ChNa, DchNa, TC and IB were purchased from Sigma-Aldrich. TC and IB were dissolved in ChNa or DchNa aqueous solutions. EPD of composite films was performed from aqueous solutions, which contained 3 g L<sup>-1</sup> ChNa with 1 g L<sup>-1</sup> TC (ChNa-TC), 3 g L<sup>-1</sup> ChNa with 1 g L<sup>-1</sup> IB (ChNa-IB), 3 g L<sup>-1</sup> DchNa with 1 g L<sup>-1</sup> TC (DchNa-TC), and 3 g L<sup>-1</sup> DchNa with 1 g L<sup>-1</sup> IB (DchNa-IB). For comparison, EPD was also performed from 3 g L<sup>-1</sup> ChNa and 3 g L<sup>-1</sup> DchNa solutions. Anodic films were obtained on stainless steel substrates at a cell voltage of 10 V, the distance between the substrates and Pt counter electrodes was 15 mm. The deposition process was also studied by cyclic voltammetry (CV) at a scan rate of 5 m V s<sup>-1</sup>, using an Au wire working electrode, Ag/AgCl reference electrode and Pt counter electrode, K0264 micro-cell and PARSTAT 2273 potentiostat (Princeton Applied Research). X-ray diffraction (XRD) studies were performed using a powder diffractometer (Nicolet I2, monochromatized CuK $\alpha$  radiation). Electron microscopy investigations were performed using a JEOL JSM-7000F scanning electron microscope (SEM).

### 6.4 Results and Discussion

ChNa and DchNa (Figure 6-1) have amphiphilic structures with convex hydrophobic and concave hydrophilic sides, which include methyl and OH<sup>-</sup> groups, respectively. The dissociation of COONa groups of ChNa and DchNa in water resulted in the formation of anionic Ch and DCh species. We found that ChNa and DchNa facilitated the dissolution of TC and IB in water. It was suggested that ChNa and DchNa formed mixed

micelles with TC and IB. It is known [4,7] that the amphiphilic structure of BS is a key factor for the solubilization of organic molecules and formation of mixed micelles. On the basis of the analysis of literature on interactions of BS with various organic molecules in aqueous solutions [11] we suggested that hydrophobic interactions of ChNa and DchNa with TC and IB, interactions of  $\text{NH}_2$  groups of TC (Figure 6-1) with  $\text{COO}^-$  groups of Ch and DCh as well as hydrogen bonding between  $\text{OH}^-$  and  $\text{COO}^-$  groups of Ch and DCh with  $\text{OH}^-$  groups of TC and  $\text{COOH}$  group of IP (Figure 6-1) facilitated the formation of mixed micelles.

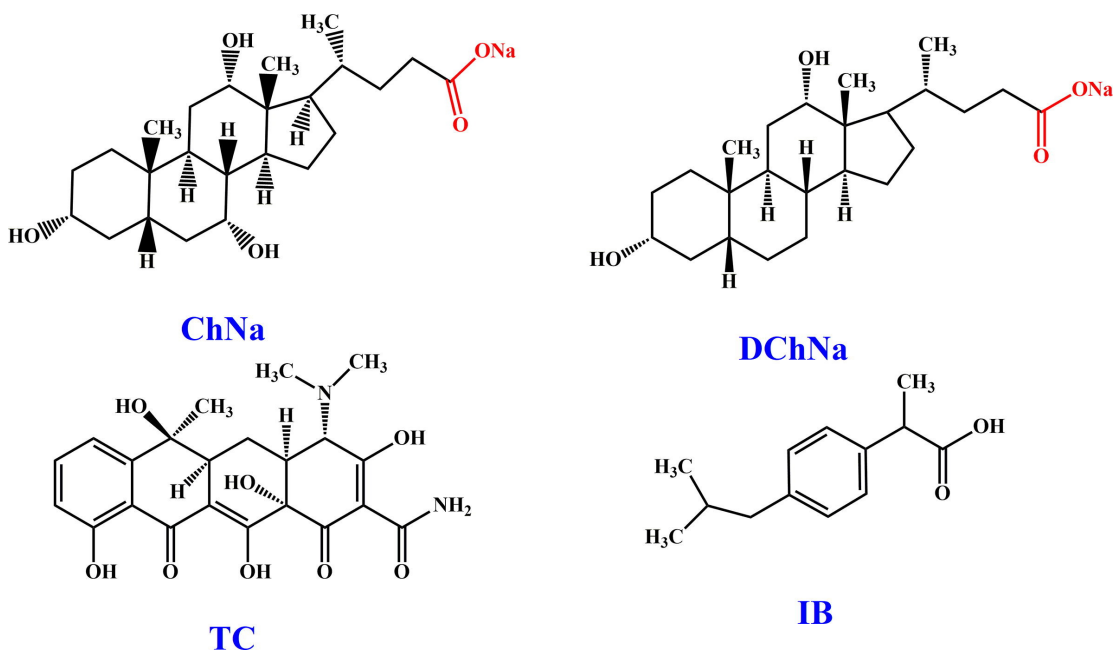
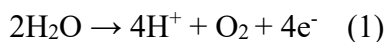


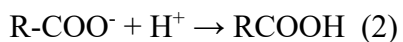
Figure 6-1: Chemical structures of ChNa, DchNa, TC and IB.

We suggested that the electrophoresis of mixed micelles, containing anionic Ch and DCh resulted in accumulation of Ch, DCh, TC and IB at the anode surface. Previous

investigations [8] showed that the EPD mechanism of film formation from ChNa and DChNa solutions involved local pH decrease at the anode surface due to the reaction:



The protonation of Ch and DCh species ( $\text{R-COO}^-$ ) at the anode resulted in the formation of water insoluble bile acid (BA) films, such as ChH and DChH ( $\text{RCOOH}$ ):



A similar mechanism can be suggested for EPD of mixed micelles and formation of composite films. In this mechanism, BS acted as solubilizing, charging and film-forming agents.

Figure 6-2 shows CV obtained in ChNa and DchNa solutions, containing TC and IB. Cycling in the potential range of 0–0.9 V resulted in the deposition of thin films.

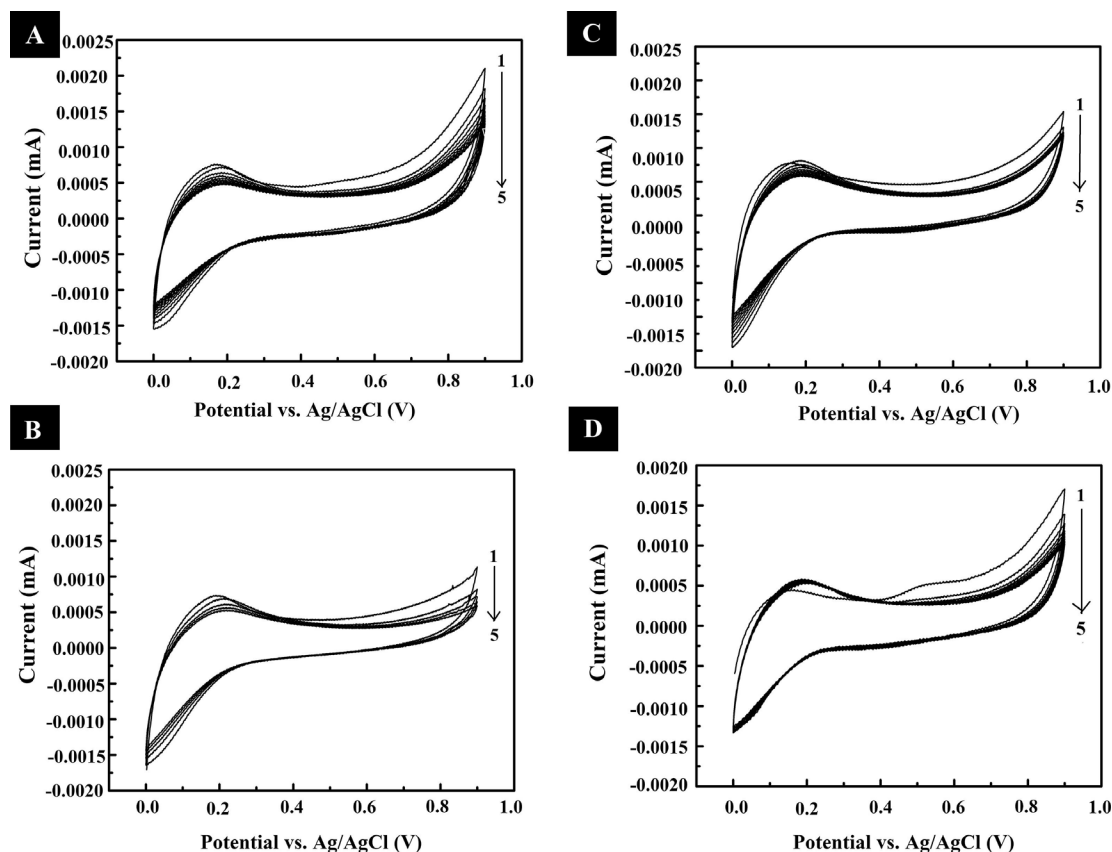


Figure 6-2: CVs for cycles 1–5 in (A) ChNa-TC, (B) ChNa-IB, (C) DchNa-TC, and (D) DchNa-IB solutions.

The observed decrease in current with increasing cycle number indicates growth of an insulating film. Constant voltage deposition experiments, conducted at a cell voltage of 10 V, allowed for formation of thick films with thickness of about 5mm, which were scraped off from the stainless steel substrates and characterized using XRD. The X-ray diffraction patterns (Figure 6-3) showed strong peaks of TC and IB in agreement with JCPDS data. Therefore, the XRD data confirmed the formation of composite films, containing TC or IB in the BS matrix.

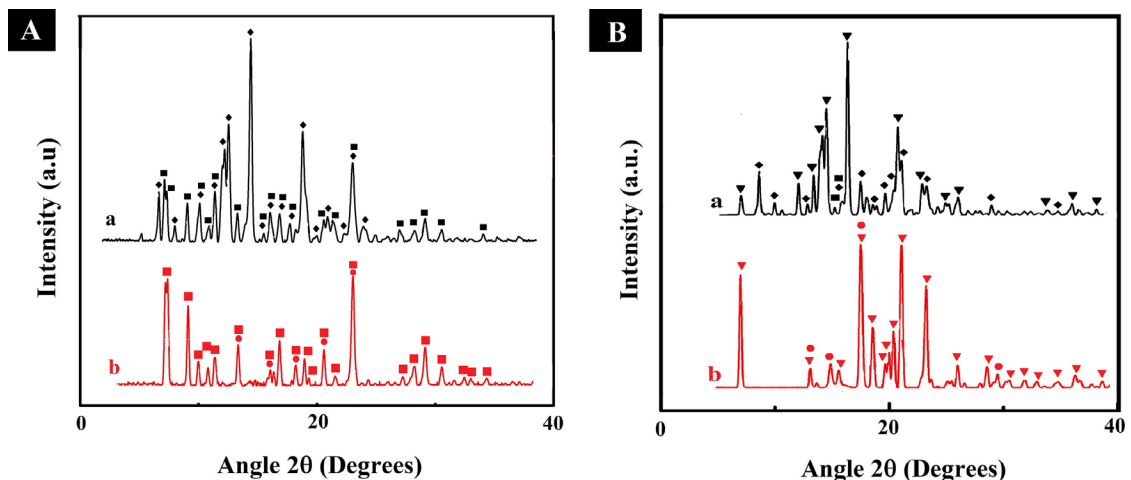


Figure 6-3: XRD patterns of deposits prepared from solutions (A) (a) ChNa-TC, (b) DchNa-TC and (B) (a) ChNa-IB, (b) DchNa-IB (■ – JCPDS file 039–1985 of TC, ▼ - JCPDS file 032–1723 of IB, ◆ - JCPDS file 015–1048 of ChH, ● – JCPDS file 008-0759 of DChH).

SEM analysis (Figure 6-4) of the films revealed a difference in the film morphology of pure BA films compared to composite films. ChH formed continuous films. Spherical particles were observed on the film surface. In contrast, DChH formed porous films. The composite ChH-TC films were continuous, however the particles on the film surface were of irregular shape. The DChH-TC and DChH-IB films contained flaky particles. The ChH-IB films were porous and contained particles with typical size of 0.2–1  $\mu\text{m}$ . The film adhesion corresponded to 4B classification (ASTM D3359).

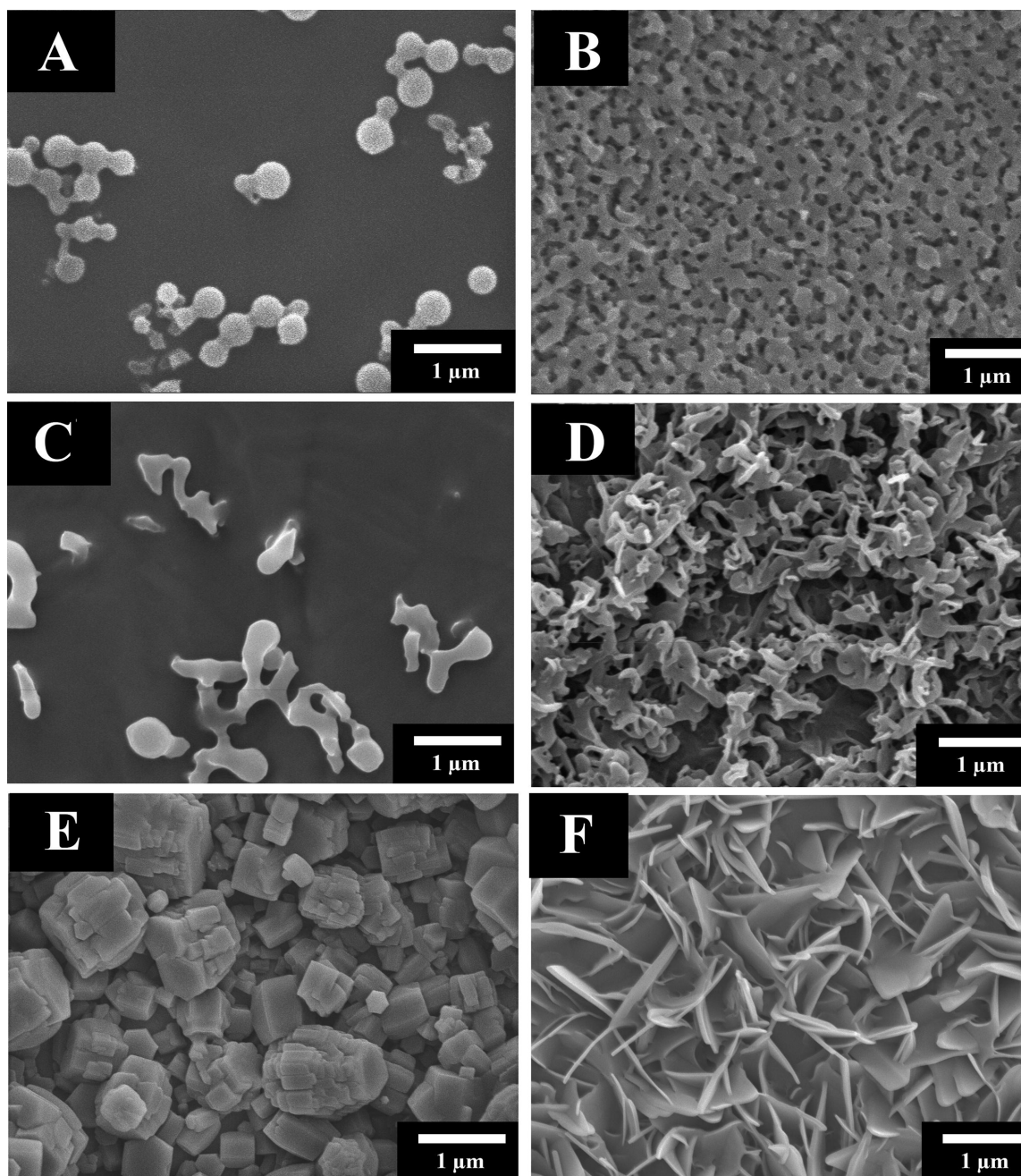


Figure 6-4: SEM images of films, prepared from (A) ChNa, (B) DchNa, (C) ChNa-TC, (D) DchNa-TC, I ChNa-IB and (F) DchNa-IB solutions.

The results of this investigation indicate that composite films, containing TC and IB, can be prepared using EPD in combination with BS. The approach was based on the use of BS for drug solubilization and charging. In our EPD method, charging of electrically neutral materials is typically achieved by adsorption of charged dispersants or polyelectrolytes. In this investigation we suggest a mechanism of deposition, which is based on the use of mixed micelles that contain charged BS molecules. Use of BS as a solubilizing, charging and film forming agent can be utilized for EPD of other functional organic molecules and inorganic nanoparticles.

## **6.5 Conclusions**

A method based on EPD has been developed for the deposition of ChH and DChH films, containing drugs. TC and IB were used as model drugs, which have low solubility in water. The suggested deposition mechanism involved solubilization of TC and IB in aqueous ChNa and DchNa solutions, formation of mixed micelles and electrophoresis of the mixed micelles. The local pH decrease and protonation of Ch and DCh species at the anode surface resulted in the formation of water insoluble composite films. The approach developed in this investigation can be used for the deposition of BA films containing other functional organic molecules and inorganic nanoparticles.

## **6.6 Acknowledgements**

Authors acknowledge the Natural Sciences and Engineering Research Council of Canada for the financial support.

## 6.7 References

- [1] S. Seuss, A.R. Boccaccini, Electrophoretic deposition of biological macromolecules, drugs, and cells, *Biomacromolecules* 14 (2013) 3355–3369.
- [2] Qiang Chen, Wei Li, O.-M. Goudouri, Yaping Ding, S. Cabanas-Polo, A.R. Boccaccini, Electrophoretic deposition of antibiotic loaded PHBV microspherical alginate composite coating with controlled delivery potential, *Colloids Surf. B Biointerfaces* 130 (2015) 199–206.
- [3] N.S. Radda'a, W.H. Goldmann, R. Detsch, J.A. Roether, L. Cordero-Arias, S. Virtanen, T. Moskalewicz, A.R. Boccaccini, Electrophoretic deposition of tetracycline hydrochloride loaded halloysite nanotubes chitosan/bioactive glass composite coatings for orthopedic implants, *Surf. Coat. Technol.* 327 (2017) 146–157.
- [4] A. Sayyed-Ahmad, L.M. Lichtenberger, A.A. Gorfe, Structure and dynamics of cholic acid and dodecylphosphocholine cholic acid aggregates, *Langmuir* 26 (2010) 13407–13414.
- [5] S. Mukhopadhyay, U. Maitra, Chemistry and biology of bile acids, *Curr. Sci.* 87 (2004) 1666–1683.
- [6] B. Jójárt, B. Viskolcz, M. Poša, S.N. Fejer, Global optimization of cholic acid aggregates, *J. Chem. Phys.* 140 (2014) 144302.
- [7] L. Galantini, M.C. di Gregorio, M. Gubitosi, L. Travaglini, J.V. Tato, A. Jover, F. Meijide, V.H.S. Tellini, N.V. Pavel, Bile salts and derivatives: rigid unconventional amphiphiles as dispersants, carriers and superstructure building blocks, *Curr. Opin. Colloid Interface Sci.* 20 (2015) 170–182.
- [8] M.S. Ata, R. Poon, A. Syed, J. Milne, I. Zhitomirsky, New developments in noncovalent surface modification, dispersion and electrophoretic deposition of carbon nanotubes, *Carbon* 130 (2018) 584–598.



- [9] M.S. Ata, I. Zhitomirsky, Colloidal methods for the fabrication of carbon nanotube–manganese dioxide and carbon nanotube–polypyrrole composites using bile acids, *J. Colloid Interface Sci.* 454 (2015) 27–34.
- [10] M. Ata, I. Zhitomirsky, Electrochemical deposition of composites using deoxycholic acid dispersant, *Mater. Manuf. Process.* 31 (2016) 67–73.
- [11] X. Sun, X. Xin, N. Tang, L. Guo, L. Wang, G. Xu, Manipulation of the gel behavior of biological surfactant sodium deoxycholate by amino acids, *J. Phys. Chem. B.* 118 (2014) 824–832.

**Chapter 7: Integrating TiO<sub>2</sub> Nanoparticles within a Catecholic Polymeric Network  
Enhances the Photoelectrochemical Response of Biosensors**

A. Victorious\*, A. Clifford\*, S. Saha, I. Zhitomirsky, and L. Soleymani

The Journal of Physical Chemistry C

Volume 123, Issue 26, pp. 16186-16193

*\*Indicates authors contributed equally to this work*

Reprinted with permission. © 2019 American Chemical Society

## 7.1 Abstract

Development of ultrasensitive biosensors for monitoring biologically relevant analytes is the key to achieving point-of-care diagnostics and health-monitoring devices. Photoelectrochemical readout, combining photonic excitation with electrochemical readout, is envisioned to enhance the limit of detection of biosensors by increasing their sensitivity and reducing background currents generated in biological samples. In spite of this, the functionalization of photoelectrochemical transducers with biorecognition elements significantly reduces the baseline current and signal-to-background ratio of these devices. Additionally, the stability of photoactive electrodes created using photoactive nanomaterial assemblies is often insufficient for withstanding multiple washing and potential cycling steps that are involved in biosensing protocols. To overcome these challenges, we created an effective conjugation strategy for integrating TiO<sub>2</sub> nanoparticles into photoactive electrodes. This strategy involves two components that work synergistically to increase the photoelectrochemical current of the transducers. The catechol-containing molecule, 3,4-dihydroxybenzaldehyde (DHB), is used to enhance the electronic and optical properties of TiO<sub>2</sub> nanoparticles for signal generation. Chitosan (CHIT) is used to enhance the film-forming properties of the DHB-conjugated TiO<sub>2</sub> nanoparticles to form uniform and stable films. Together, DHB and CHIT resulted in the formation of an extensive network of TiO<sub>2</sub> nanoparticles within the DHB–CHIT matrix and enhanced the generated photocurrent by a factor of 10. We modified the optimized photoelectrode with DNA probes to create a photoelectrochemical DNA detector. The TiO<sub>2</sub>–DHB–CHIT photoelectrodes offered the required stability and signal magnitude to

distinguish between complementary and noncomplementary DNA sequences, paving the route toward photoelectrochemical DNA sensing.

## 7.2 Introduction

TiO<sub>2</sub> nanoparticles are widely used as the photoactive building blocks of electrodes for applications in photoelectrochemistry (PEC).(1,2) In PEC, light is used to generate charge carriers in the photoactive material to drive electrochemical reactions. The possibility to operate PEC cells in photovoltaic, photoelectrosynthetic, or photocatalytic modes(3) enables them to be used in a wide range of applications such as energy conversion focused on water splitting and solar energy conversion,(4) developing self-cleaning and environmental cleaning surfaces for removing bacterial and other organic contaminants,(5–11) and biosensors for the detection of proteins and nucleic acids.(12–14) TiO<sub>2</sub> nanoparticles are widely used in these PEC-enabled applications due to their high photocatalytic activity,(15) photo- and chemical stabilities,(16–19) corrosion resistance,(18,20,21) high degree of control over morphology and crystallinity,(22,23) position of conduction and valence band levels for driving useful electrochemical reactions,(10,15,24–26) insolubility in aqueous media, nontoxicity, and low cost.(16,17)

In PEC, it is desirable to achieve a high incident photon-to-electron conversion efficiency (IPCE) to enhance the electrochemical reaction rate and the resultant photoelectrochemical current. This requires the photoactive materials, such as TiO<sub>2</sub> nanoparticles, to have high photon absorption and low-carrier recombination rates.(27,28) Additionally, it is critical for the photoactive building blocks to be embedded in a three-

dimensional and porous architecture with a high internal surface area that interacts effectively with the electrolyte, enables efficient charge transport, and offers low losses due to carrier recombination.(15,29–32)

P25-TiO<sub>2</sub> nanoparticles, combining anatase (>70%) and rutile structures, are regarded as the benchmark TiO<sub>2</sub> nanoparticles for PEC due to their enhanced photoactivity. This is attributed to increased carrier lifetime enabled by charge transfer from the rutile to the anatase phase, improved crystallinity, increased defect density, and larger crystal sizes.(33–35)

In spite of the abovementioned benefits, P25-TiO<sub>2</sub> in its pristine form has a wide band gap (3.0–3.2 eV),(36) which limits its absorption to the UV range.(18,37) To increase the number of absorbed photons and further increase the lifetime of photogenerated carriers, the electronic structure of this material has been altered by doping with impurities,(18,38) disorder engineering with the use of core-shell nanoparticles,(39–42) and surface modification with quantum dots,(20,37) plasmonic metal nanoparticles,(21) or organic ligands.(18) To exploit such electronically optimized materials in photoelectrochemical devices, it is essential to embed them in photoactive frameworks that have optimal charge-transfer properties and remain stable under electrochemical cycling in liquids.(31) Consequently, additional steps such as sintering,(43–45) addition of binders,(46,47) mechanical compression,(48) deposition of amorphous TiO<sub>2</sub> binder layers using postdeposition sol-gel and chemical vapor deposition,(49,50) and irradiation with microwave(51) have been employed to incorporate TiO<sub>2</sub> nanoparticles into photoactive electrodes. These additional steps could result in the loss of porosity in the three-

dimensional network of particles and add to the overall cost, complexity, and thermal budget of the process.

Our goal was to develop a strategy for creating high-performance photoelectrodes based on P25-TiO<sub>2</sub> nanoparticles for photoelectrochemical biosensing. This imposed stringent parallel requirements on the photoelectrode properties. It was essential for the photoelectrode to demonstrate large baseline photoelectrochemical currents to compensate for the signal loss caused by biofunctionalization, to demonstrate repeatable and stable photocurrents under electrochemical scanning in liquid, and the photoactive matrix needed to be easily functionalizable for coupling with biorecognition elements.<sup>(52)</sup> To address these requirements, we sought to develop a facile method for developing P25-TiO<sub>2</sub>-based materials with increased light absorption and charge separation, binding sites for attaching biorecognition probes, and built-in film-forming properties for creating well-adhered and uniform photoactive frameworks on the collector electrodes.

Organic ligands, such as conductive polymers, organic dyes, and phenolic compounds, are widely used for modifying the electronic properties of TiO<sub>2</sub> nanoparticles for use in PEC and photocatalysis.<sup>(21)</sup> In dye-sensitized solar cells, TiO<sub>2</sub> nanoparticles are modified with organic dyes to increase IPCE in the visible range by photoexcitation of the dye-to-TiO<sub>2</sub> charge-transfer band.<sup>(53)</sup> Among these, catecholic molecules are promising candidates for modifying the electronic properties and improving the dispersion of TiO<sub>2</sub> nanoparticles.<sup>(54)</sup> To exploit catechol-modified TiO<sub>2</sub> nanoparticles, having improved electronic, optical, and dispersion properties in PEC biosensing, we turned to bioinspired catecholic polymers. These polymers exploit the same material chemistry used by mussels

to adhere to surfaces in aqueous environments(55) and have been used in the laboratory as wet adhesives for modifying the surface of medical implants.(56,57)

We hypothesized that linking TiO<sub>2</sub> nanoparticles with a catecholic polymer would enable us to create a biosensing photoelectrode with enhanced IPCE, uniformity, and wet-state adhesion due to the synergistic contribution of catechol and the porous polymer network toward tuning the electronic and film-forming properties of the material. To evaluate this hypothesis, we dispersed TiO<sub>2</sub> nanoparticles into a chitosan (CHIT)–catechol polymer, utilizing a Schiff base reaction between 3,4-dihydroxybenzaldehyde (DHB) and chitosan (CHIT),(56) and applied this hybrid organic/inorganic material to a conductive electrode using a one-step drop-casting method. We evaluated the chemical modification of TiO<sub>2</sub> with DHB, CHIT, and DHB–CHIT using Fourier transform infrared spectroscopy (FTIR) and investigated their structural and functional characteristics using scanning electron microscopy (SEM), IPCE, and photocurrent measurements. Upon successful photoelectrode fabrication with optimized IPCE and PEC performances using the DHB–CHIT strategy, we modified our material system to integrate amine-terminated DNA capture probes within the hybrid organic/inorganic framework to create a photoelectrochemical DNA biosensor. This approach can be applied to a wide range of photoelectrochemical devices that have yet to be translated from the laboratory to the real world, where the use of air and water stable, nonpolluting, and nontoxic photoactive materials is essential.

### 7.3 Results and Discussion

To enhance the photocurrent of PEC biosensors, we modified bare P25-TiO<sub>2</sub> with DHB, CHIT, and DHB-CHIT (Figure 7-1). The catechol functional group of DHB offers ultra strong adhesion to inorganic particles and surfaces(54) and forms a charge-transfer complex between the particle and the catechol-containing molecule.(58,59) This modification tunes the electronic and optical properties of the material(58,59) and imparts redox activity.(27,60) In addition to electronic and optical tunability, catechol-containing molecules improve the dispersion of inorganic nanoparticles such as TiO<sub>2</sub>;(16) however, DHB on its own has poor film-forming properties needed for the fabrication of photoelectrodes. CHIT was introduced as a film-forming agent to integrate DHB-modified P25-TiO<sub>2</sub> nanoparticles into photoactive electrodes. Previous studies have found that CHIT combined with TiO<sub>2</sub> nanoparticles also boosts the electrochemical behavior due to the formation of a chelate bond between the amine and hydroxyl groups in the chitosan monomer and surface Ti ions.(19,61) However, pure CHIT is unstable under harsh operating conditions, but its stability increases when modified with a catechol group.(57)



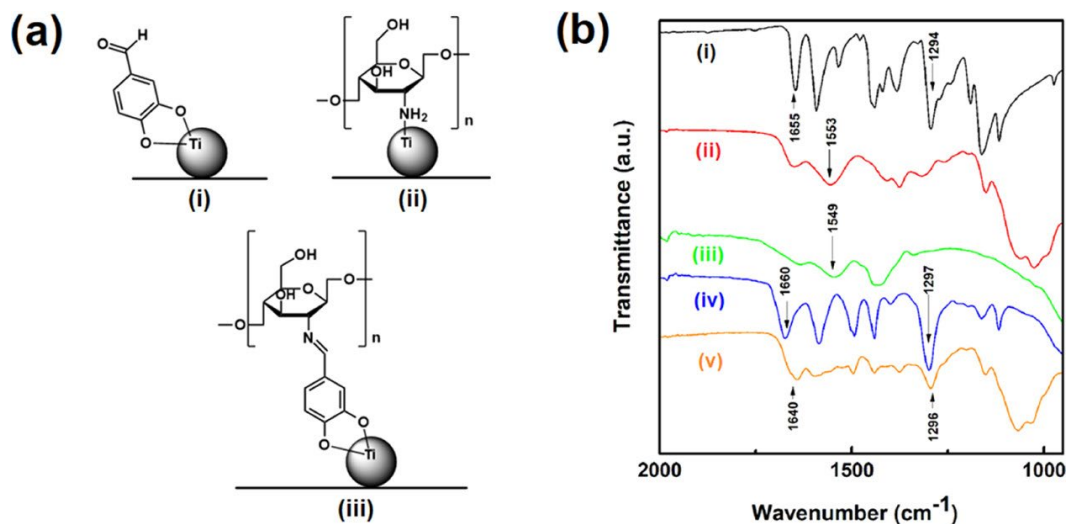


Figure 7-1: Chemical characterization of P25-TiO<sub>2</sub> modified with different ligands. (a) Chemical structures of (i) catecholic bonding of DHB to P25-TiO<sub>2</sub>, (ii) bonding between chitosan and P25-TiO<sub>2</sub>, and (iii) catecholic bonding between DHB-CHIT and P25-TiO<sub>2</sub>. (b) FTIR spectra of as-received (i) DHB and (ii) CHIT powders. FTIR spectra of P25-TiO<sub>2</sub> modified with (iii) CHIT, (iv) DHB, and (v) DHB-CHIT.

We expect catechol groups to serve a dual purpose in our PEC biosensors: improve the IPCE of P25-TiO<sub>2</sub> nanoparticles, especially in the visible range, and work with CHIT to form a uniform and stable film that can undergo multiple washing and electrochemical scanning steps, as encountered in sensing systems. As a result, we developed a simple one-step method of introducing catechol to CHIT using DHB. The modification procedure was based on a Schiff base reaction (Figure 7-1a) between DHB and CHIT.<sup>(34)</sup> The formation of DHB-modified CHIT was confirmed using FTIR (Figure 7-1b). In the as-received CHIT spectrum, characteristic absorptions were detected at approximately 1,081, 1,031, and 895 cm<sup>-1</sup>. These absorptions represent the stretching vibrations from the hydroxyl group, the C–O–C in the glucose circle, and the glucoside bond, respectively.<sup>(62)</sup> Characteristic

absorption at approximately  $1550\text{ cm}^{-1}$ , corresponding to the amide II group,(63) was also visible in the CHIT spectra and the spectra from P25-TiO<sub>2</sub> nanoparticles modified with pure CHIT. This confirms the surface modification of P25-TiO<sub>2</sub> with CHIT. The 1,081, 1,031, and  $895\text{ cm}^{-1}$  absorptions were detected in the spectra of P25-TiO<sub>2</sub> modified with the DHB-CHIT ligand. Absorptions at  $\sim 1660$  and  $1295\text{ cm}^{-1}$  from the as-received DHB spectra were also found in the spectra of P25-TiO<sub>2</sub> modified with DHB and DHB-CHIT ligands and are attributed to C=O and O-H vibrations from the aldehyde and phenol groups.(63) The weak absorption at  $\sim 1640\text{ cm}^{-1}$  in the DHB-modified CHIT spectra is indicative of a Schiff base formation and vibrations from the RCH=N-R' bond.(63) The presence of absorptions from the as-received CHIT and DHB spectra in the spectra acquired from P25-TiO<sub>2</sub> nanoparticles modified with the DHB-CHIT ligand and characteristic vibrations from RCH=N-R' confirm the formation of a Schiff base ligand between CHIT and DHB. It is known that characteristic bands of Schiff base functional groups are emitted in the range of  $1630\text{--}1690\text{ cm}^{-1}$ , but these bands appear weak in the infrared spectrum and intense in the Raman spectrum.(63) Formation of a Schiff base ligand was further confirmed (see Figure 7-S1) as evidenced by the intense band observed at  $\sim 1646\text{ cm}^{-1}$  in the Raman spectra of P25-TiO<sub>2</sub>-DHB-CHIT, which was not present in the Raman spectra collected from bare P25-TiO<sub>2</sub>, P25-TiO<sub>2</sub>-CHIT or P25-TiO<sub>2</sub>-DHB.

Scanning electron microscopy (SEM) was used to compare the surface morphology of photoelectrodes fabricated from unmodified P25-TiO<sub>2</sub> nanoparticles with those from functionalized P25-TiO<sub>2</sub> nanoparticles (P25-TiO<sub>2</sub>-DHB, P25-TiO<sub>2</sub>-CHIT, P25-TiO<sub>2</sub>-DHB-CHIT) (Figure 7-2). The films fabricated from unmodified nanoparticles were

nonuniform and contained large P25-TiO<sub>2</sub> agglomerates due to weak bonding of the nanoparticles to the electrode surface. The P25-TiO<sub>2</sub>-DHB films demonstrated a more even film with a reduced amount of agglomerates, and the P25-TiO<sub>2</sub>-CHIT films contained large agglomerates and less surface coverage than unmodified nanoparticles. Lastly, P25-TiO<sub>2</sub>-CHIT-DHB samples revealed a remarkable improvement in the film properties with the P25-TiO<sub>2</sub> nanoparticles distributed in a uniform film containing the smallest amount of agglomeration. In the case of CHIT, film formation occurs via hydrogen bonding between Ti-O-Ti inorganic network and CHIT, as well as coordination bonding in P25-TiO<sub>2</sub>-CHIT nanocomposite.(61) This allows for adhesion of the adjacent P25-TiO<sub>2</sub> layers. However, when the amount of P25-TiO<sub>2</sub> increases, small agglomerates form.(64) This phenomenon is attributed to the lack of adhesion between P25-TiO<sub>2</sub> and CHIT within each layer.

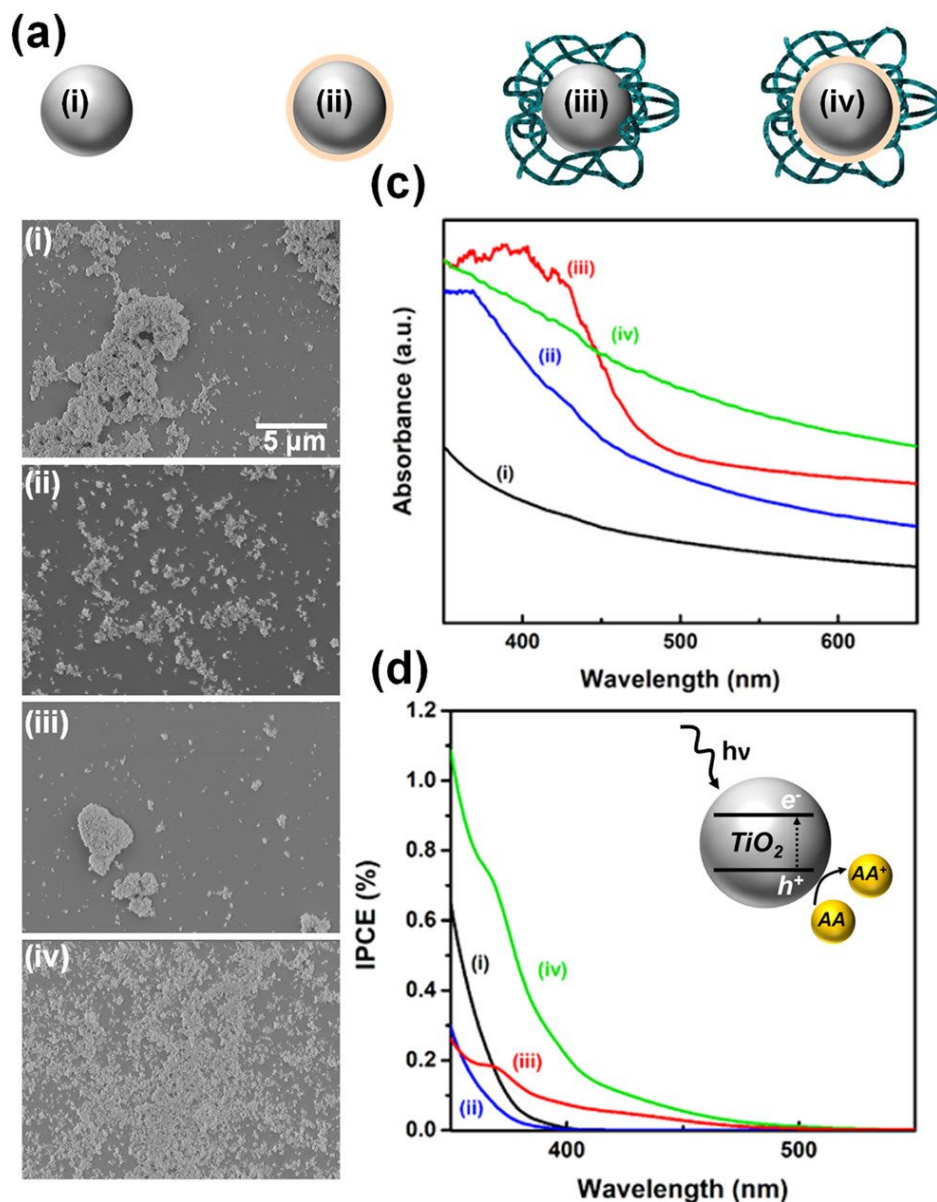


Figure 7-2: Structural, optical, and photoelectrochemical characterizations of films created from unmodified and functionalized P25- $\text{TiO}_2$  nanoparticles. (a) Schematics of (i) unmodified P25- $\text{TiO}_2$ , (ii) DHBA-modified P25- $\text{TiO}_2$ , (iii) chitosan-modified P25- $\text{TiO}_2$ , and (iv) DHBA-chitosan-modified P25- $\text{TiO}_2$ . Images demonstrating scanning electron micrographs (b), UV/visible absorbance (c), and IPCE (d) of films created from P25- $\text{TiO}_2$  nanoparticles demonstrated in (a). The inset in (d) demonstrates the mechanism of photoelectrochemical oxidation of ascorbic acid (AA) using P25- $\text{TiO}_2$

Irradiation of P25-TiO<sub>2</sub> with light having energy equal to or greater than its band-gap energy (3.0–3.2 eV) generates electron–hole pairs that participate in redox reactions.<sup>(65)</sup> Ascorbic acid (AA), a hole scavenger, then combines with photogenerated holes in TiO<sub>2</sub> and generates a PEC current through its oxidation at the surface of the working electrode (Figure 7-2d, inset).<sup>(66)</sup> The annihilation of holes by AA results in the movement of electrons from the conduction band of the P25-TiO<sub>2</sub> to the indium tin oxide (ITO) electrode where it is collected as a measurable current.

To understand the correlation between P25-TiO<sub>2</sub> functionalization and PEC response, we measured the UV/visible absorbance (Figure 7-2c) and IPCE of the four classes of P25-TiO<sub>2</sub> photoelectrodes fabricated using the successive deposition of solution-based nanoparticles onto ITO-coated poly(ethylene terephthalate) (PET) electrodes (Figure 7-2d). UV–visible spectroscopy confirmed the modification of the electronic structure of P25-TiO<sub>2</sub> by CHIT, DHB, and DHB–CHIT, since the absorption spectra of the electrodes fabricated using functionalized P25-TiO<sub>2</sub> nanoparticles were all shifted to longer wavelengths compared to those fabricated using unmodified P25-TiO<sub>2</sub> nanoparticles. Additionally, diffuse reflectance spectroscopy was performed on photoelectrodes fabricated with these different surface functionalizations. No change in band gap was seen in either of the functionalizations as compared to bare P25-TiO<sub>2</sub> (Figure 7-S2). This was also demonstrated by Janković et al. who saw an insignificant change in the band gap of TiO<sub>2</sub> following ligand modification.<sup>(67)</sup>

Even though both P25-TiO<sub>2</sub>–CHIT and P25-TiO<sub>2</sub>–DHB films demonstrate an enhancement in absorbance across the entire measurement range compared to unmodified

P25-TiO<sub>2</sub>, the IPCE measurements demonstrate that the modification of P25-TiO<sub>2</sub> with both DHB and CHIT results in a superior photoelectrochemical response across the wavelength range of 350–500 nm. This validates our hypothesis that the synergy between DHB and CHIT is essential in controlling the electronic and film-forming properties of P25-TiO<sub>2</sub> nanoparticles toward engineering high-performance electrodes for PEC. Furthermore, the IPCE of our electrodes was compared to an instance of ligand-modified P25-TiO<sub>2</sub> in the literature, where a composite P25-TiO<sub>2</sub> film was deposited on a transparent conductor using the doctor blade method.<sup>(68)</sup> Dopamine (DA) was then modified onto the fabricated electrodes via solution immersion.<sup>(68)</sup> Unlike our one-pot synthesis, this method required specialized machinery and multiple steps for synthesis. Furthermore, the IPCE of the DA-P25-TiO<sub>2</sub> photoelectrodes indicated a maximum enhancement of ~15% as compared to the unmodified P25-TiO<sub>2</sub> photoelectrodes. In contrast, an approximate enhancement of 69% in the IPCE of P25-TiO<sub>2</sub>-DHB-CHIT was exhibited by our photoelectrodes as compared to that of the unmodified P25-TiO<sub>2</sub> (Figure 7-2c). While our electrodes exhibited a better enhancement following ligand modification, it is important to note that the DA-P25-TiO<sub>2</sub> photoelectrodes fabricated by Kim et al. demonstrated a higher IPCE response. This can be attributed to their nonsolution-based electrode fabrication process, resulting in superior film quality.

In addition to IPCE, amperometric I–t measurements, a method typically used for photoelectrochemical readout in biosensors, were conducted on the photoelectrodes created using unmodified and functionalized P25-TiO<sub>2</sub> nanoparticles (Figure 7-3a). In accordance with the IPCE results, the unmodified P25-TiO<sub>2</sub> films showed the lowest current density,

while P25-TiO<sub>2</sub>-DHB and P25-TiO<sub>2</sub>-CHIT showed an increase in PEC current density. As expected, the largest amount of photocurrent was generated by the P25-TiO<sub>2</sub>-DHB-CHIT photoelectrodes. These photoelectrodes showed more than a 10-fold increase in photocurrent compared to unmodified P25-TiO<sub>2</sub>.

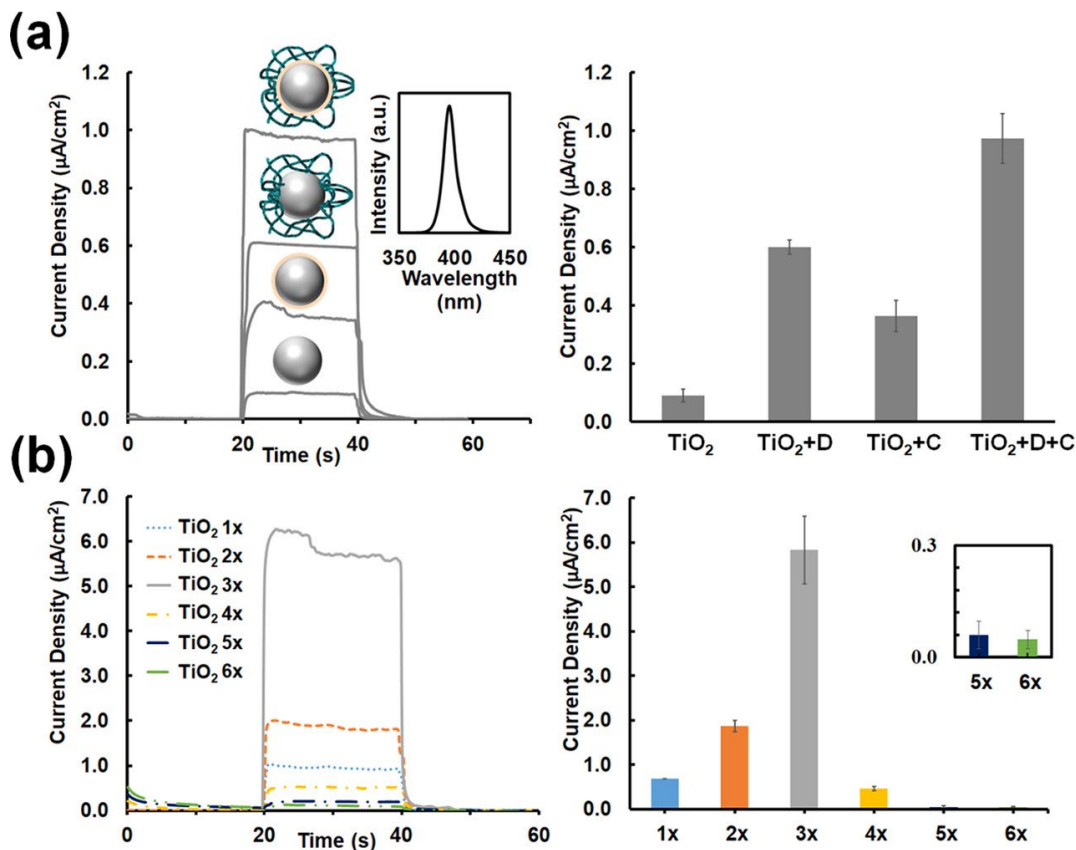


Figure 7-3: Enhancing the base photocurrent of the P25-TiO<sub>2</sub> electrodes. (a) PEC current density measurements for P25-TiO<sub>2</sub> with different surface functionalization and their respective current response (left) and as summarized in bar plots (right). The inset demonstrates the spectrum of the optical excitation source. “D” denotes DHB, and “C” denotes chitosan. (b) PEC current density measurements with increasing P25-TiO<sub>2</sub> concentration in a P25-TiO<sub>2</sub>-DHB-CHIT film (left) and as summarized as bar plots (right). Error bars represent one standard deviation and 1–6× concentration refers to 33.3, 66.6, 99.9, 133.2, 166.5, and 199.8 g L<sup>-1</sup>, respectively.

We expect this remarkable order-of-magnitude increase in photocurrent to be the result of increased photon absorption rate, as well as enhanced charge separation and collection rate. The UV/vis spectroscopy results demonstrate that there is a greater overlap between the emission spectrum of the excitation source (Figure 7-3a) and the absorption spectrum of P25-TiO<sub>2</sub>-DHB-CHIT nanoparticles (Figure 7-2c) compared to all other P25-TiO<sub>2</sub> films used in this study. Interestingly, even at 350 nm, where all modified P25-TiO<sub>2</sub> films demonstrate similar absorptions, films modified with both CHIT and DHB yield the highest conversion efficiency. We believe this is due to the improved film uniformity, surface coverage, and contact between the P25-TiO<sub>2</sub> and the ITO collector electrodes. Moreover, the micro- and nanostructures of the photoelectrode influence the accessibility of hole-scavenging species such as ascorbic acid to the surface of the photoelectrode, which, in turn, influences the generated photocurrent.<sup>(32)</sup> The use of chitosan in conjunction with DHB results in a micro/nanoporous material (Figure 7-4a), which exhibits enhanced film-forming and electronic properties, thereby synergistically enhancing the generated photocurrent.



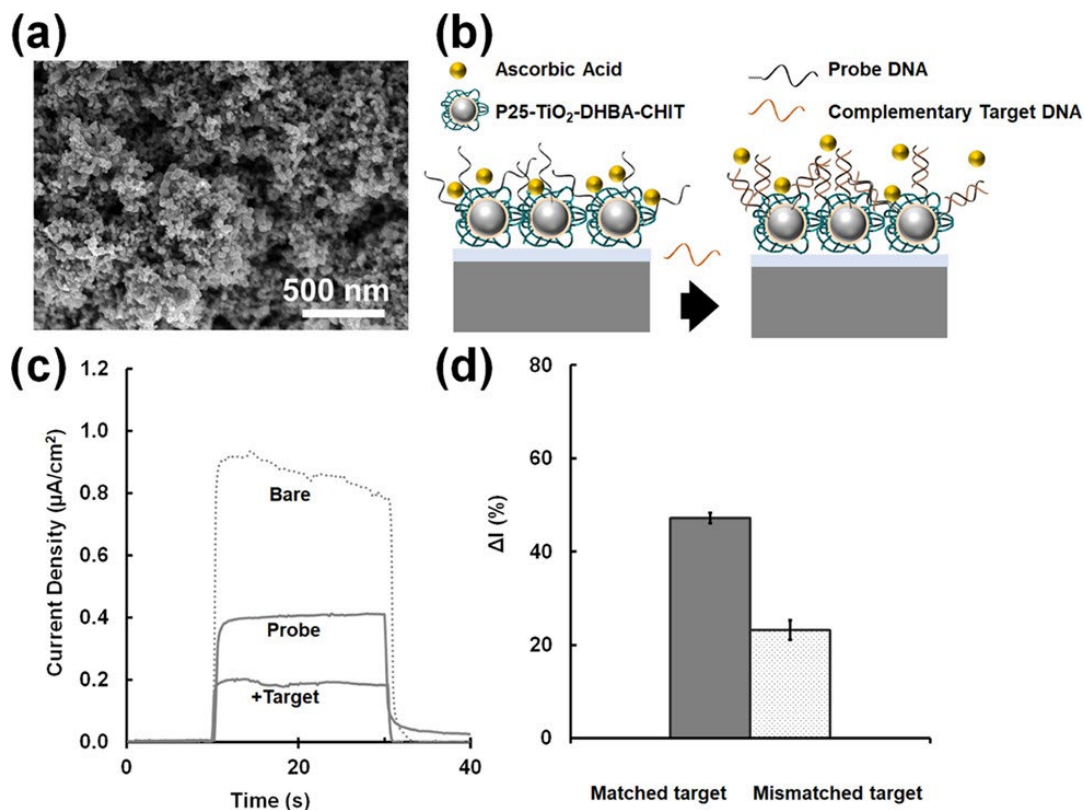


Figure 7-4: Photoelectrochemical DNA detection using  $\text{TiO}_2$ -DHB-CHIT electrodes. (a) Scanning electron micrograph of  $\text{TiO}_2$ -DHB-CHIT electrodes. (b) Schematic demonstration of the biofunctionalization of electrodes with probe DNA, hybridization with complementary target DNA, and photoelectrochemical detection using ascorbic acid as the reporter. (c) Photocurrent density of bare, probe-modified, and probe-modified electrode hybridized with complementary DNA target (+target). (d) Percentage current decrease measured between probe-modified electrodes incubated with matched (complementary) and mismatched target DNA. Error bars represent one standard deviation.

To find the optimal concentration of P25- $\text{TiO}_2$  for increasing the photocurrent, PEC experiments were performed at various concentrations of P25- $\text{TiO}_2$ , while keeping the concentration of DHB and CHIT in the co-functionalized P25- $\text{TiO}_2$ -DHB-CHIT films

constant (Figure 7-3b). As the concentration of P25-TiO<sub>2</sub> is increased, photocurrent density is enhanced until the P25-TiO<sub>2</sub> concentration is tripled. This observed increase in photocurrent is attributed to the presence of a larger population of P25-TiO<sub>2</sub> nanoparticles within the same geometric area, resulting in the increased absorption and generation of charge carriers.<sup>(69)</sup> The photocurrent density decrease observed beyond a threefold increase in P25-TiO<sub>2</sub> concentration is attributed to the unavailability of the sufficient amount of DHB-CHIT ligands to obtain films with optimal electronic property, uniformity, surface coverage, and reduced agglomeration. Furthermore, chopped light amperometry was performed to evaluate the stability of the various photoelectrodes under 10 light excitation cycles in a period of 600 s. The relative standard deviation (Rsd) is widely used statistically to express the precision and repeatability of measurement, and by extension, it is a measure of stability when applied in the context of photoelectrodes.<sup>(70)</sup> It is calculated as

$$Rsd\% = \frac{\sigma}{\mu} \times 100 \quad (1)$$

where  $\sigma$  is the standard deviation and  $\mu$  represents the mean of the sample population. Results indicated good stability in photoelectrodes fabricated by increasing P25-TiO<sub>2</sub> concentration from one time up to four times (Rsd of 4.39, 4.86, 5.40, and 1.10%, respectively) (Figure 7-S3). However, photoelectrodes formed by increasing the P25-TiO<sub>2</sub> concentration by five and six times revealed excellent stability (Rsd of 0.63 and 0.85%, respectively) (Figure 7-S3). Furthermore, a significant decrease in photocurrent density of ~42.6, 53.7, and 45.1% was exhibited by photoelectrodes synthesized from 1×, 2×, and 3× P25-TiO<sub>2</sub> concentrations, while a minimal decrease of ~8.2, 0.4, and 1.6% was exhibited

by 4×, 5×, and 6× P25-TiO<sub>2</sub> concentrations, respectively, following storage in dark conditions at 4 °C for 7 days (Figure 7-S4). It should be noted that although films created from 3× P25-TiO<sub>2</sub> demonstrated the largest PEC response, films with higher P25-TiO<sub>2</sub> concentrations might be preferred in applications where long-term stability is critical.

To create a PEC biosensor for detecting DNA hybridization, it is essential to develop surfaces that generate PEC currents and selectively capture DNA targets. To address this goal, we asked the question, is it possible to introduce DNA capture capability into the TiO<sub>2</sub>-DHB-CHIT films to combine enhanced PEC signals with DNA selectivity? For this purpose, we sought to couple amine-terminated DNA to P25-TiO<sub>2</sub>-DHB. However, the amine groups in DNA are expected to compete with the amine groups in CHIT for the aldehyde groups of DHB. We hypothesized that increasing the DHB concentration would increase the overall binding sites for DNA and CHIT and would increase the density of DNA probes. A PEC assay with an increased amount of DHB (3×) for successful probe immobilization was employed to distinguish between complementary and noncomplementary DNA (Figure 7-4). We expected that an increase in the concentration of DNA at the electrode surface would decrease the PEC current generated from AA oxidation by limiting the access of AA to the electrode surface (Figure 7-4b).(14) PEC measurements demonstrate a decrease in current following probe deposition, as well as after incubation with complementary targets (Figure 7-4c). A larger decrease in PEC current is seen following the introduction of complementary target compared to that of noncomplementary target (Figure 7-4d). As only the complementary target sequence can hybridize with the DNA probe, a larger decrease is exhibited by the complementary case

due to the increased steric hindrance of AA caused by the resulting double-stranded DNA.(71) The current decrease observed for the noncomplementary sequences is attributed to nonspecific adsorption on the photoelectrode surface.(72) It is evident from the data below that successful biofunctionalization and DNA hybridization detection were achieved using these high-performance P25-TiO<sub>2</sub>-DHB-CHIT electrodes.

## 7.4 Conclusions

In this work, we sought to create photoelectrodes having high incident photon-to-electron conversion efficiency (IPCE) that were stable and robust for use in photoelectrochemical biosensing. We hypothesized that integrating P25-TiO<sub>2</sub> nanoparticles in a catecholic polymeric framework would be an effective strategy for introducing photoactive materials onto collector electrodes for photoelectrochemical biosensing. Toward this goal, we compared unmodified P25-TiO<sub>2</sub>, P25-TiO<sub>2</sub> nanoparticles functionalized with chitosan, P25-TiO<sub>2</sub> nanoparticles functionalized with a catechol-containing molecule (3,4-dihydroxybenzaldehyde), and P25-TiO<sub>2</sub> nanoparticles functionalized with a catechol-modified chitosan. Films that included both the catechol and chitosan elements demonstrated increased photonic absorption over the UV and visible wavelengths and significantly enhanced IPCE and the resultant photoelectrochemical current by a factor of 10. The enhanced photoelectrochemical response was the result of the synergistic effect of the catechol-containing polymer in modifying the electronic and optical properties of P25-TiO<sub>2</sub> as indicated by UV and IPCE measurements and improving its film-forming properties as evidenced by SEM characterization. In addition to offering

an order-of-magnitude enhancement in photocurrent, these photoactive electrodes enabled integration with biorecognition elements such as DNA. Amine-terminated DNA was easily conjugated within the photoactive framework through Schiff base reactions with the catechol-containing 3,4-dihydroxybenzaldehyde. The biofunctionalized photoactive electrodes developed here offered the signal-to-noise ratio and stability that are required for performing biosensing experiments and were able to distinguish between complementary and noncomplementary DNA sequences at a concentration of 0.5  $\mu\text{M}$ . One-pot fabrication of stable photoactive electrodes using a fully solution-based process, such as the one developed in this work, is critical to ensure the translation of materials synthesized in lab to an industrial scale. As such, the unique and facile route developed here for enhancing the performance of  $\text{TiO}_2$ -based photoelectrodes is instrumental in paving the way for improved efficiency in other PEC technologies developed for energy conversion and environmental cleaning.

## **7.5 Methods**

### **7.5.1 Chemicals**

Chitosan, from shrimp shells (degree of deacetylation  $\geq 75\%$ ), acetic acid, 3,4-dihydroxybenzaldehyde (DHB), and poly(ethylene terephthalate)/indium tin oxide (PET/ITO) substrate were purchased from Sigma-Aldrich, Canada. Aeroxide P25- $\text{TiO}_2$  was obtained from Nippon Aerosil Co. Ltd.

### 7.5.2 TiO<sub>2</sub> Surface Modification

Four different aqueous P25-TiO<sub>2</sub> suspensions were prepared. One suspension contained bare P25-TiO<sub>2</sub> and other three contained surface-modified P25-TiO<sub>2</sub>. CHIT, DHB, and DHB-CHIT were used for surface modification and dispersion of P25-TiO<sub>2</sub>. Aqueous CHIT solution was prepared by dissolving CHIT in deionized (DI) water using 1% acetic acid. The final CHIT concentration was 3 g L<sup>-1</sup>. An aqueous solution of DHB was prepared by dissolving DHB in deionized water, with a final concentration of 8 g L<sup>-1</sup>. DHB-modified CHIT solution was obtained by modifying CHIT in the liquid phase. The mass ratio of DHB to CHIT added to the CHIT solution was 2:1, and upon the addition of DHB solution to CHIT solution, the solution color changed from clear to yellow. P25-TiO<sub>2</sub> was added to either a CHIT solution, DHB solution, or DHB-modified CHIT solution to form suspensions containing surface-modified P25-TiO<sub>2</sub>.

### 7.5.3 Electrode Fabrication

All PET/ITO substrates with dimensions of 1.0 cm x 0.7 cm were masked using vinyl tape to preserve the electrode contact area. Once masked, substrates were treated in oxygen plasma for 1 min.

All films were fabricated by dropping 10 microliters of solution onto the exposed PET/ITO substrate surface. They were then air-dried for 30 min, washed in deionized (DI) water, and air-dried for a second time. This process was repeated for a total of three layers.

#### **7.5.4 Material Characterization**

The surface morphology of the fabricated substrates was analyzed using scanning electron microscopy (JEOL JSM-7000F) using conventional sample preparation procedures. A Bruker Vertex 70 spectrometer was used for Fourier transform infrared spectroscopy (FTIR), and flame-S-UV-vis-ES assembly was used for ultraviolet-visible (UV-vis) spectroscopy. Incident photon-to-current conversion efficiency (IPCE) measurements were obtained using a Zahner CIMPS-QE/IPCE3 Photo-Electrochemical Workstation in a three-electrode cell configuration with a solution containing 0.1 M phosphate-buffered saline (PBS) and 0.1 M ascorbic acid (AA) as the supporting electrolyte and a tunable light source probing wavelengths from 300 to 600 nm.

#### **7.5.5 Photoelectrochemical Characterization**

PEC measurements were carried out in a three-electrode cell setup with an ultraviolet flashlight to facilitate illumination of the photoelectrode surface. Platinum (Pt) wire was used as the counter electrode and silver/silver chloride (Ag/AgCl) as the reference electrode with the deposited films on PET/ITO substrates acting as the working electrode. A 0.1 M PBS solution with 0.1 M ascorbic acid (AA) was used as the supporting electrolyte. Linear sweeps were measured by a CHI 660D electrochemical station, under UV illumination at every 20 s for a period of 100 s. Photocurrents were reported as the difference in current with and without incident light on the face of the TiO<sub>2</sub> electrode.

### 7.5.6 DNA Hybridization Experiments

Electrodes were fabricated using a layer-by-layer drop-casting method, followed by probe ssDNA (1  $\mu\text{M}$ ) deposition for 3 h and incubation with noncomplementary (0.5  $\mu\text{M}$ ) and complementary (0.5  $\mu\text{M}$ ) target DNA for 60 min. Electrodes were washed between each deposition step using DI water. Photoelectrochemical tests were run using a CHI 660D workstation and PBS/AA as the supporting electrolyte.

### 7.6 Supporting Information

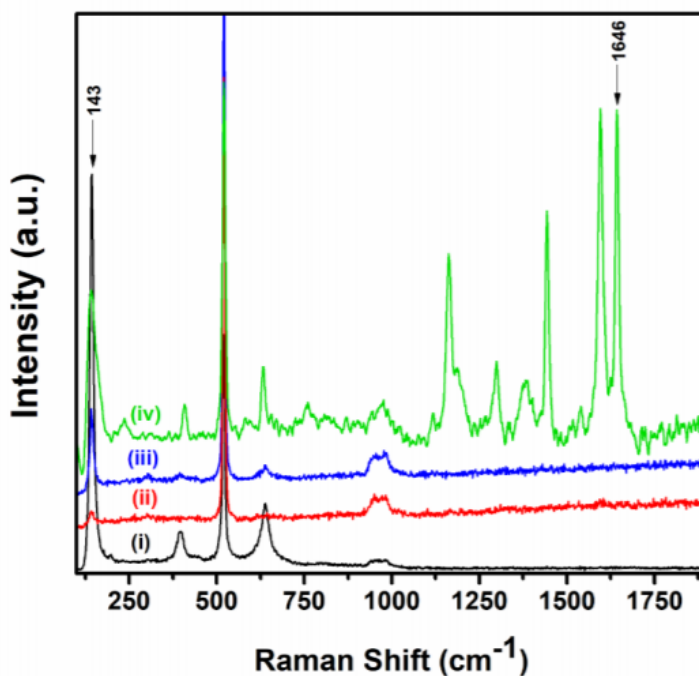


Figure 7-S1: Raman spectroscopy of i) unmodified P25-TiO<sub>2</sub>, ii) DHBA-modified P25-TiO<sub>2</sub>, iii) chitosan-modified P25-TiO<sub>2</sub>, and iv) DHBA-chitosan-modified P25-TiO<sub>2</sub>.



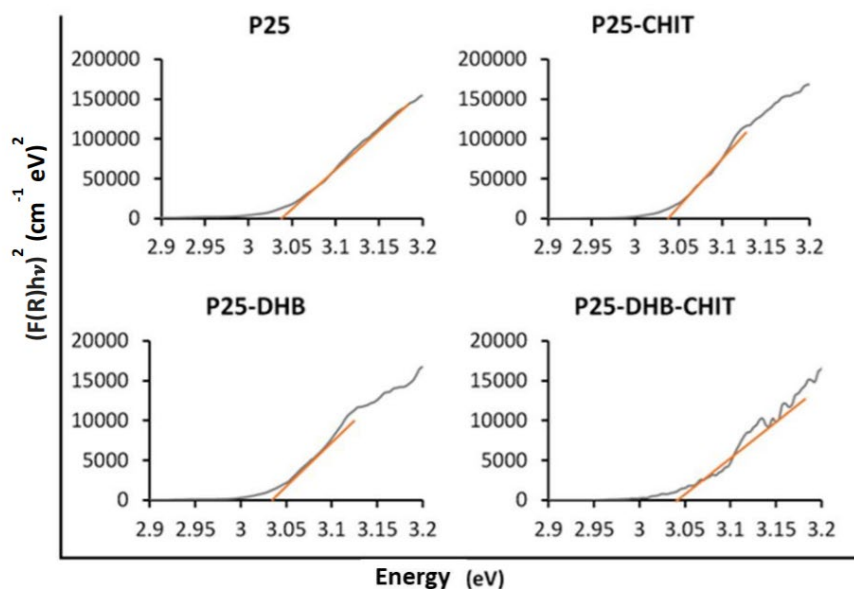


Figure 7-S2: Bandgap measurements of modified TiO<sub>2</sub> nanoparticles

Diffuse reflectance spectroscopy was performed on photo-electrodes with different surface functionalization. Bandgap of 3.04 eV was obtained for all four materials by extrapolating the linear portion of the obtained curves to determine the x-intercept. No significant change in bandgap was seen in either of the functionalizations as compared to bare P25-TiO<sub>2</sub>.

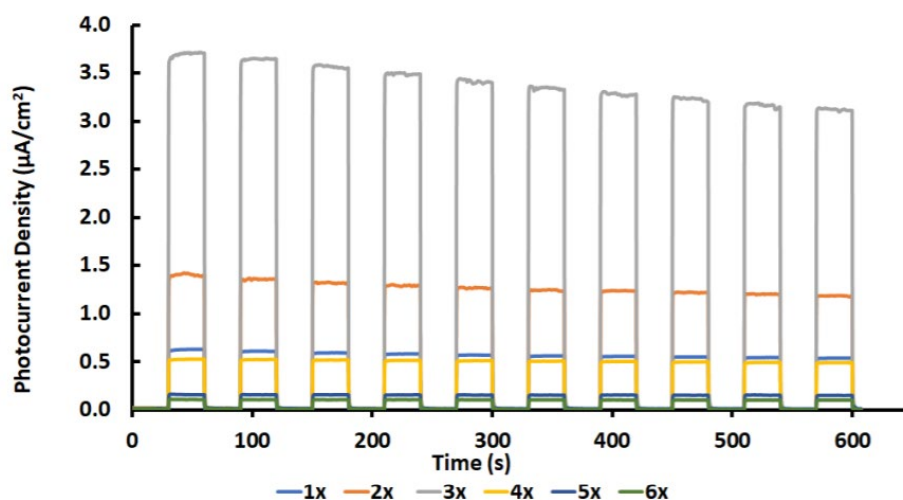


Figure 7-S3: Stability measurements of electrodes fabricated with increasing P25-TiO<sub>2</sub> concentration in a P25-TiO<sub>2</sub>-DHB-CHIT film.

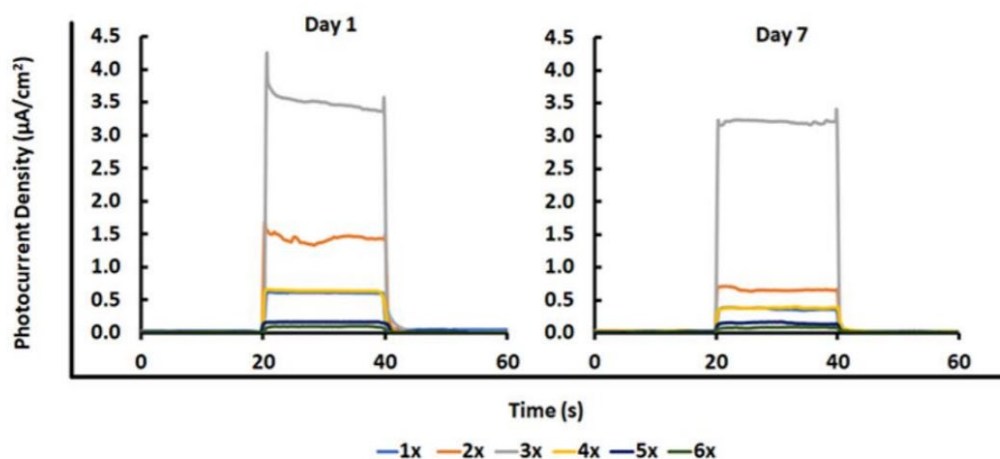


Figure 7-S4: Photocurrent response following storage in dark condition at 4°C for 7 days.

## 7.7 Acknowledgements

The authors acknowledge the financial support provided for this work from NSERC and Ontario Ministry of Research and Innovation. L.S. is the Canada Research Chair in

Miniaturized Biomedical Devices and is supported by the Canada Research Chairs Program. L.S. is the recipient of the Ontario Early Researcher Award. S.S. is the recipient of the NSERC PGS-D scholarship. The microscopy work was carried out at the Canadian Centre for Electron Microscopy, a facility supported by the Canada Foundation for Innovation under the Major Science Initiative program, NSERC, and McMaster University.

## 7.8 References

- (1) Devadoss, A.; Sudhagar, P.; Terashima, C.; Nakata, K. New Insights into Promising Photoelectrodes and Signal Amplification Strategies. *J. Photochem. Photobiol., C*. 2015, 24, No. 43.
- (2) Shen, S.; Chen, J.; Wang, M.; Sheng, X.; Chen, X.; Feng, X.; Mao, S. S. Titanium Dioxide Nanostructures for Photoelectrochemical Applications. *Prog. Mater. Sci.* 2018, 299–385.
- (3) Aikens, D. A. *Electrochemical Methods, Fundamentals and Applications*. *J. Chem. Educ.* 1983, 60, No. A25.
- (4) Fujishima, K.; Honda, A. Electrochemical Photolysis of Water at a Semiconductor Electrode. *Nature* 1972, 238, 37–38.
- (5) Konstantinou, I. K.; Albanis, T. A. TiO<sub>2</sub>-Assisted Photocatalytic Degradation of Azo Dyes in Aqueous Solution: Kinetic and Mechanistic Investigations: A Review. *Appl. Catal., B* 2004, 49, 1–14.
- (6) Barakat, M. A. New Trends in Removing Heavy Metals from Industrial Wastewater. *Arab. J. Chem.* 2011, 4, 361–377.
- (7) Jardim, W. F.; Moraes, S. G.; Takiyama, M. M. K. Photocatalytic Degradation of Aromatic Chlorinated Compounds Using TiO<sub>2</sub>: Toxicity of Intermediates. *Water Res.* 1997, 31, 1728–1732.
- (8) Lhomme, L.; Brosillon, S.; Wolbert, D. Photocatalytic Degradation of Pesticides in Pure Water and a Commercial Agricultural Solution on TiO<sub>2</sub> Coated Media. *Chemosphere* 2008,

70, 381–386.

(9) Daghrir, R.; Drogui, P.; Robert, D. Modified TiO<sub>2</sub> for Environmental Photocatalytic Applications: A Review. *Ind. Eng. Chem. Res.* 2013, 3581–3599.

(10) Reddy, K. R.; Hassan, M.; Gomes, V. G. Hybrid Nanostructures Based on Titanium Dioxide for Enhanced Photocatalysis. *Appl. Catal., A* 2015, 489, 1–16.

(11) Fu, G.; Vary, P. S.; Lin, C.-T. Anatase TiO<sub>2</sub> Nanocomposites for Antimicrobial Coatings. *J. Phys. Chem. B* 2005, 109, 8889–8898.

(12) Yan, Z.; Wang, Z.; Miao, Z.; Liu, Y. Dye-Sensitized and Localized Surface Plasmon Resonance Enhanced Visible-Light Photoelectrochemical Biosensors for Highly Sensitive Analysis of Protein Kinase Activity. *Anal. Chem.* 2016, 88, 922–929.

(13) Shu, J.; Qiu, Z.; Lv, S.; Zhang, K.; Tang, D. Plasmonic Enhancement Coupling with Defect-Engineered TiO<sub>2</sub>-x: A Mode for Sensitive Photoelectrochemical Biosensing. *Anal. Chem.* 2018, 90, 2425–2429.

(14) Saha, S.; Chan, Y.; Soleymani, L. Enhancing the Photoelectrochemical Response of DNA Biosensors Using Wrinkled Interfaces. *ACS Appl. Mater. Interfaces* 2018, 10, 31178–31185.

(15) Fujishima, A.; Rao, T. N.; Tryk, D. A. Titanium Dioxide Photocatalysis. *J. Photochem. Photobiol., C* 2000, 1, 1–21.

(16) Saraswat, S. K.; Rodene, D. D.; Gupta, R. B. Recent Advancements in Semiconductor Materials for Photoelectrochemical Water Splitting for Hydrogen Production Using Visible Light. *Renewable Sustainable Energy Rev.* 2018, 89, 228–248.

(17) Joy, J.; Mathew, J.; George, S. C. Nanomaterials for Photoelectrochemical Water Splitting – Review. *Int. J. Hydrogen Energy* 2018, 43, 4804–4817.

(18) Abdullah, H.; Khan, M. M. R.; Ong, H. R.; Yaakob, Z. Modified TiO<sub>2</sub> Photocatalyst for CO<sub>2</sub> Photocatalytic Reduction: An Overview. *J. CO<sub>2</sub> Util.* 2017, 22, 15–32.

(19) Karthikeyan, K. T.; Nithya, A.; Jothivenkatachalam, K. Photocatalytic and Antimicrobial Activities of Chitosan-TiO<sub>2</sub> Nanocomposite. *Int. J. Biol. Macromol.* 2017, 104, 1762–1773.

- (20) Yan, K.; Wang, R.; Zhang, J. A Photoelectrochemical Biosensor for o-Aminophenol Based on Assembling of CdSe and DNA on TiO<sub>2</sub> film Electrode. *Biosens. Bioelectron.* 2014, 53, 30–3074.
- (21) Kumar, S. G.; Rao, K. S. R. K. Comparison of Modification Strategies towards Enhanced Charge Carrier Separation and Photocatalytic Degradation Activity of Metal Oxide Semiconductors (TiO<sub>2</sub>, WO<sub>3</sub> and ZnO). *Appl. Surf. Sci.* 2017, 391, 124–148.
- (22) Chemseddine, A.; Moritz, T. Nanostructuring Titania: Control over Nanocrystal Structure, Size, Shape, and Organization. *Eur. J. Inorg. Chem.* 1999, 1999, 235–245.
- (23) Rajh, T.; Chen, L. X.; Lukas, K.; Liu, T.; Thurnauer, M. C.; Tiede, D. M. Surface Restructuring of Nanoparticles: An Efficient Route for Ligand-Metal Oxide Crosstalk. *J. Phys. Chem. B* 2002, 106, 10543–10552.
- (24) Lan, Y.; Lu, Y.; Ren, Z. Mini Review on Photocatalysis of Titanium Dioxide Nanoparticles and Their Solar Applications. *Nano Energy* 2013, 2, 1031–1045.
- (25) Park, H.; Park, Y.; Kim, W.; Choi, W. Surface Modification of TiO<sub>2</sub> Photocatalyst for Environmental Applications. *J. Photochem. Photobiol., C* 2013, No. 20.
- (26) Xu, Q.; Zhang, L.; Yu, J.; Wageh, S.; Al-Ghamdi, A. A.; Jaroniec, M. Direct Z-Scheme Photocatalysts: Principles, Synthesis, and Applications. *Mater. Today* 2018, 21, 1042–1063.
- (27) Kim, E.; Liu, Y.; Bentley, W. E.; Payne, G. F. Redox Capacitor to Establish Bio-Device Redox-Connectivity. *Adv. Funct. Mater.* 2012, 22, 1409–1416.
- (28) Pesci, F. M.; Wang, G.; Klug, D. R.; Li, Y.; Cowan, A. J. Efficient Suppression of Electron-Hole Recombination in Oxygen- Deficient Hydrogen-Treated TiO<sub>2</sub> Nanowires for Photoelectrochemical Water Splitting. *J. Phys. Chem. C* 2013, 117, 25837–25844.
- (29) Shankar, K.; Basham, J. I.; Allam, N. K.; Varghese, O. K.; Mor, G. K.; Feng, X.; Paulose, M.; Seabold, J. A.; Choi, K.; Grimes, C. A. Recent Advances in the Use of TiO<sub>2</sub> Nanotube and Nanowire Arrays for Oxidative. *J. Phys. Chem. C* 2009, 113, 6327–6359.
- (30) Snaith, H. J.; Moule, A. J.; Klein, C.; Meerholz, K.; Friend, R.H.; Grätzel, M. Efficiency Enhancements in Solid-State Hybrid Solar Cells via Reduced Charge Recombination and Increased Light Capture. *Nano Lett.* 2007, 7, 3372–3376.

- (31) Fattakhova-Rohlfing, D.; Zaleska, A.; Bein, T. Three-Dimensional Titanium Dioxide Nanomaterials. *Chem. Rev.* 2014, 114, 9487– 9558.
- (32) Zhang, Q.-H.; Han, W.-D.; Hong, Y.-J.; Yu, J.-G. Photocatalytic Reduction of CO<sub>2</sub> with H<sub>2</sub>O on Pt-Loaded TiO<sub>2</sub> Catalyst. *Catal. Today* 2009, 148, 335–340.
- (33) Bellardita, M.; Di Paola, A.; Megna, B.; Palmisano, L. Determination of the Crystallinity of TiO<sub>2</sub> Photocatalysts. *J. Photochem. Photobiol., A* 2018, 367, 312–320.
- (34) Qian, R.; Zong, H.; Schneider, J.; Zhou, G.; Zhao, T.; Li, Y.; Yang, J.; Bahnemann, D. W.; Pan, J. H. Charge Carrier Trapping, Recombination and Transfer during TiO<sub>2</sub> Photocatalysis: An Overview. *Catal. Today* 2018, No. 53.
- (35) Ohtani, B.; Prieto-Mahaney, O. O.; Li, D.; Abe, R. What Is Degussa (Evonic) P25? Crystalline Composition Analysis, Reconstruction from Isolated Pure Particles and Photocatalytic Activity Test. *J. Photochem. Photobiol., A* 2010, 216, 179–182.
- (36) Apopei, P.; Catrinescu, C.; Teodosiu, C.; Royer, S. Mixed- Phase TiO<sub>2</sub> Photocatalysts: Crystalline Phase Isolation and Reconstruction, Characterization and Photocatalytic Activity in the Oxidation of 4-Chlorophenol from Aqueous Effluents. *Appl. Catal., B* 2014, 160–161, 374–382.
- (37) Li, S.; Wang, Y.; Gao, C.; Ge, S.; Yu, J.; Yan, M. “Signal-off” Photoelectrochemical DNA Sensing Strategy Based on Target Dependent DNA Probe Conformational Conversion Using CdS Quantum Dots Sensitized TiO<sub>2</sub> nanorods Array as Photoactive Material. *J. Electroanal. Chem.* 2015, 759, 38–45.
- (38) Hantusch, M.; Bessergenev, V.; Mateus, M. C.; Knupfer, M.; Burkel, E. Electronic Properties of Photocatalytic Improved Degussa P25 Titanium Dioxide Powder. *Catal. Today* 2018, 307, 111–118.
- (39) Wang, X.; Estradé, S.; Lin, Y.; Yu, F.; Lopez-Conesa, L.; Zhou, H.; Gurram, S. K.; Peiró, F.; Fan, Z.; Shen, H.; et al. Enhanced Photoelectrochemical Behavior of H-TiO<sub>2</sub> Nanorods Hydrogenated by Controlled and Local Rapid Thermal Annealing. *Nanoscale Res. Lett.* 2017, 12, No. 336.

- (40) Lü, X.; Chen, A.; Luo, Y.; Lu, P.; Dai, Y.; Enriquez, E.; Dowden, P.; Xu, H.; Kotula, P. G.; Azad, A. K.; et al. Conducting Interface in Oxide Homojunction: Understanding of Superior Properties in Black TiO<sub>2</sub>. *Nano Lett.* 2016, 16, 5751–5755.
- (41) Yan, P.; Liu, G.; Ding, C.; Han, H.; Shi, J.; Gan, Y.; Li, C. Photoelectrochemical Water Splitting Promoted with a Disordered Surface Layer Created by Electrochemical Reduction. *ACS Appl. Mater. Interfaces* 2015, 7, 3791–3796.
- (42) Fan, C.; Chen, C.; Wang, J.; Fu, X.; Ren, Z.; Qian, G.; Wang, Z. Black Hydroxylated Titanium Dioxide Prepared via Ultrasonication with Enhanced Photocatalytic Activity. *Sci. Rep.* 2015, 5, No. 11712.
- (43) Yu, J.; Yu, H.; Cheng, B.; Trapalis, C. Effects of Calcination Temperature on the Microstructures and Photocatalytic Activity of Titanate Nanotubes. *J. Mol. Catal. A: Chem.* 2006, 249, 135–142.
- (44) Tebby, Z.; Babot, O.; Michau, D.; Hirsch, L.; Carlos, L.; Toupance, T. A Simple Route towards Low-Temperature Processing of Nanoporous Thin Films Using UV-Irradiation: Application for Dye Solar Cells. *J. Photochem. Photobiol., A* 2009, 205, 70–76.
- (45) Lewis, L. N.; Spivack, J. L.; Gasaway, S.; Williams, E. D.; Gui, J.Y.; Manivannan, V.; Siclovan, O. P. A Novel UV-Mediated Low- Temperature Sintering of TiO<sub>2</sub> for Dye-Sensitized Solar Cells. *Sol. Energy Mater. Sol. Cells* 2006, 90, 1041–1051.
- (46) Kay, A.; Grätzel, M. Low Cost Photovoltaic Modules Based on Dye Sensitized Nanocrystalline Titanium Dioxide and Carbon Powder. *Sol. Energy Mater. Sol. Cells* 1996, 44, 99–117.
- (47) De Marco, L.; Manca, M.; Giannuzzi, R.; Malara, F.; Melcarne, G.; Ciccarella, G.; Zama, I.; Cingolani, R.; Gigli, G. Novel Preparation Method of TiO<sub>2</sub>-Nanorod-Based Photoelectrodes for Dye-Sensitized Solar Cells with Improved Light-Harvesting Efficiency. *J. Phys. Chem. C* 2010, 114, 4228–4236.
- (48) Hagfeldt, A.; Lindström, H.; Holmberg, A.; Magnusson, E.; Lindquist, S.-E.; Malmqvist, L. A New Method for Manufacturing Nanostructured Electrodes on Plastic Substrates. *Nano Lett.* 2001, 1, 97–100.

- (49) Yu, H.; Zhang, S.; Zhao, H.; Xue, B.; Liu, P.; Will, G. High- Performance TiO<sub>2</sub> Photoanode with an Efficient Electron Transport Network for Dye-Sensitized Solar Cells. *J. Phys. Chem. C* 2009, 113, 16277–16282.
- (50) Miyasaka, T.; Kijitori, Ō.Y.; Murakami, T. N.; Kimura, M.; Uegusa, S. Efficient Nonsintering Type Dye-Sensitized Photocells Based on Electrophoretically Deposited Voltage. *Chem. Lett.* 2002, 1250–1251.
- (51) Tahir, A. A.; Peiris, T. A. N.; Wijayantha, K. G. U. Enhancement of Photoelectrochemical Performance of AA CVD Produced TiO<sub>2</sub> Electrodes by Microwave Irradiation While Preserving the Nanostructure. *Chem. Vap. Depos.* 2012, 18, 107–111.
- (52) Soleymani, L.; Li, F. Mechanistic Challenges and Advantages of Biosensor Miniaturization into the Nanoscale. *ACS Sensors* 2017, 2, 458–467.
- (53) Tae, E. L.; Lee, S. H.; Lee, J. K.; Yoo, S. S.; Kang, E. J.; Yoon, K. B. A Strategy to Increase the Efficiency of the Dye-Sensitized TiO<sub>2</sub> Solar Cells Operated by Photoexcitation of Dye-to-TiO<sub>2</sub> Charge-Transfer Bands. *J. Phys. Chem. B* 2005, 109, 22513–22522.
- (54) Ata, M. S.; Liu, Y.; Zhitomirsky, I. A Review of New Methods of Surface Chemical Modification, Dispersion and Electrophoretic Deposition of Metal Oxide Particles. *RSC Adv.* 2014, 4, 22716–22732.
- (55) Li, L.; Zeng, H. Marine Mussel Adhesion and Bio-Inspired Wet Adhesives. *Biotribology* 2016, 5, 44–51.
- (56) Clifford, A.; Pang, X.; Zhitomirsky, I. Biomimetically Modified Chitosan for Electrophoretic Deposition of Composites. *Colloids Surf. A*, 2018, 544, 28–34.
- (57) Ryu, J. H.; Hong, S.; Lee, H. Bio-Inspired Adhesive Catechol- Conjugated Chitosan for Biomedical Applications: A Mini Review. *Acta Biomaterialia*; Acta Materialia Inc, 2015; pp 101–115.
- (58) Janković, I. A.; Šaponjić, Z. V.; Čomor, M. I.; Nedeljković, J. M. Surface Modification of Colloidal TiO<sub>2</sub> Nanoparticles with Bidentate Benzene Derivatives. *J. Phys. Chem. C* 2009, 113, 12645–12652.



- (59) Wang, G. L.; Xu, J. J.; Chen, H. Y. Dopamine Sensitized Nanoporous TiO<sub>2</sub> Film on Electrodes: Photoelectrochemical Sensing of NADH under Visible Irradiation. *Biosens. Bioelectron.* 2009, 24, 2494–2498.
- (60) Kim, E.; Liu, Y.; Shi, X. W.; Yang, X.; Bentley, W. E.; Payne, G. F. Biomimetic Approach to Confer Redox Activity to Thin Chitosan Films. *Adv. Funct. Mater.* 2010, 20, 2683–2694.
- (61) Khan, R.; Dhayal, M. Electrochemical Studies of Novel Chitosan/TiO<sub>2</sub> Bioactive Electrode for Biosensing Application. *Electrochem. Commun.* 2008, 10, 263–267.
- (62) Pan, S.; Wu, S.; Kim, J. Preparation of Glucosamine by Hydrolysis of Chitosan with Commercial  $\alpha$ -Amylase and Glucoamylase. *J. Zhejiang Univ., Sci., B* 2011, 12, 931–934.
- (63) Socrates, G. *Infrared and Raman Characteristic Group Frequencies*; John Wiley & Sons, 2004.
- (64) Norranattrakul, P. Fabrication of Chitosan/Titanium Dioxide Composites Film for the Photocatalytic Degradation of Dye. *J. Met., Mater. Miner.* 2013, 23, 9–22.
- (65) Ni, M.; Leung, M. K. H.; Leung, D. Y. C.; Sumathy, K. A Review and Recent Developments in Photocatalytic Water-Splitting Using TiO<sub>2</sub> for Hydrogen Production. *Renewable Sustainable Energy Rev.* 2007, 11, 401–425.
- (66) Fan, D.; Wu, D.; Cui, J.; Chen, Y.; Ma, H.; Liu, Y.; Wei, Q.; Du, B. An Ultrasensitive Label-Free Immunosensor Based on CdS Sensitized Fe-TiO<sub>2</sub> with High Visible-Light Photoelectrochemical Activity. *Biosens. Bioelectron.* 2015, 74, 843–848.
- (67) Janković, I. A.; Šaponjić, Z. V.; Džunuzović, E. S.; Nedeljković, J. M. New Hybrid Properties of TiO<sub>2</sub> Nanoparticles Surface Modified With Catecholate Type Ligands. *Nanoscale Res. Lett.* 2010, 5, 81–88.
- (68) Kim, S.; Moon, G.; Kim, G.; Kang, U.; Park, H.; Choi, W. TiO<sub>2</sub> Complexed with Dopamine-Derived Polymers and the Visible Light Photocatalytic Activities for Water Pollutants. *J. Catal.* 2017, 346, 92–100.
- (69) Plana, D.; Fermín, D. J. Photoelectrochemical Activity of Colloidal TiO<sub>2</sub> Nanostructures Assembled at Polarisable Liquid/Liquid Interfaces. *J. Electroanal. Chem.* 2016, 780, 373–378.

(70) Kenkel, J. *Analytical Chemistry for Technicians*, 3rd; CRC Press, 2002.

(71) Yan, K.; Liu, Y.; Yang, Y.; Zhang, J. A Cathodic “Signal-off” Photoelectrochemical Aptasensor for Ultrasensitive and Selective Detection of Oxytetracycline. *Anal. Chem.* 2015, 87, 12215–12220.

(72) Galasso, K.; Livache, T.; Roget, A.; Vieil, E. Electrogravimetric Detection of DNA Hybridization on Polypyrrole Copolymer. *J. Chim. Phys. Phys.-Chim. Biol.* 1998, 95, 1514–1517.

## Chapter 8: Conclusions

### 8.1 Summary of Conclusions and Contributions

In summary, the primary objective of this work was to develop multi-functional nanocomposite materials used primarily for orthopaedic applications, but also for other applications such as electrochemical biosensing. The overarching objective was achieved, and as a result of this work, fifteen new organic-inorganic nanocomposite biomaterials and their corresponding processing techniques have been created, none of which had previously existed before this work. Specific major findings can be summarized as follows:

- A novel one-step technique for the modification of chitosan (CHIT), and poly-L-lysine (PLL) with catechol (CAT) utilizing EPD and a Schiff base reaction has been developed. This technique improves upon previously described two-step electrochemical fabrication techniques for biopolymer functionalization with CAT and has allowed for the fabrication of nanocomposite films containing bioceramics, such as HA and TiO<sub>2</sub> for orthopaedic and dental coating applications. Specifically, CAT-PLL was used for the fabrication of composite coatings consisting of HA, TiO<sub>2</sub> and HA co-deposited with TiO<sub>2</sub>. These coatings were hydrophilic while simultaneously exhibiting surface roughness, and incorporated features on both the micron and nanoscale, as well as ultra-strong coating adhesion. The coatings also were found to promote cell proliferation and adhesion in preliminary *in vitro* studies, and this combination of advantageous surface features has not been achieved in one fabrication step previously.

- The functionalization of CHIT with CAT imparted the films with unique pseudocapacitive behaviour, which has been used previously for voltammetric biosensor applications, due to the ability to amplify current output in the presence of redox mediators. Our improved one-step fabrication technique resulted in increasing the pseudocapacitive behaviour of the films by approximately two orders of magnitude, using a lower scan rate, compared to what was reported in the literature using films fabricated using the two-step technique. This increased redox-behaviour was utilized for the formation of nanocomposite Ag-CAT-CHIT films, which were fabricated using novel *in-situ* reduction and subsequent fabrication of films containing uniformly sized and well-dispersed Ag nanoparticles, a well-known anti-microbial agent. Other organic-inorganic nanocomposite CAT-CHIT films were also fabricated for biomedical implant applications, containing bioactive ceramics such as HA and TiO<sub>2</sub>, as well as HA co-deposited with TiO<sub>2</sub>. Resulting films are multi-functional and may be used towards both orthopaedic implant and electrochemical voltammetric sensing applications.
- Building upon previous work with CAT-CHIT, we discovered that ligand modification of TiO<sub>2</sub> nanoparticles using CAT-CHIT altered the electronic structure of the TiO<sub>2</sub> nanoparticles and resulted in increased photocurrent generation upon ultraviolet light excitation. This modification was found to not only increase the generated photocurrent, but also increased the range of excitation

wavelengths so that photocurrent may be generated by the CAT-CHIT TiO<sub>2</sub> films in not only the ultraviolet range, but also in the visible spectrum. Single strand probe DNA was attached to the film surface and was used as a signal-off PEC biosensor for DNA detection. These novel composite TiO<sub>2</sub> films may not only be used for genetic sensing, but other applications that require increased photocatalytic efficiency such as photovoltaics, water splitting and CO<sub>2</sub> reduction.

- A conceptually new technique for the fabrication of composite gel coatings for drug delivery, containing commercially available drugs with low solubility in water, was also developed. In this work BAS, which are powerful natural anionic biosurfactants, were used as dispersing, charging, and film-forming agents. Model bile acid salts sodium deoxycholate (DChNa) and sodium cholate (NaCh) were used for the solubilization and subsequent composite film fabrication, with commercially available water-insoluble drugs ibuprofen (IB), and tetracycline (TC) (anti-biotic). This was the first report of the use of charged mixed micelles for film formation using EPD and is unique compared to the traditional use of polyelectrolytes for charging, dispersion, and film formation.

## **8.2 Limitations and Future Work**

Although we present coating systems for orthopaedic implants, to be used in combination with metallic substrates to combine advantageous properties of mechanical strength from the metallic substrate with biological and chemical properties of the coating, much work could be done towards fabrication of a truly biomimetic composite to

replace human bone. Such a composite would utilize collagen, HA nanoparticles and bone morphogenic proteins, and would not only mimic the biochemical composition of bone, but also the hierarchical structure. Invention of such a synthetic biomimetic composite would solve many remaining problems, including the stress-shielding effect.

Another issue that requires further consideration is surfaces that support osseointegration and osseointegration while simultaneously preventing bacterial adhesion and formation of biofilms. In our attempts to fabricate surfaces that are anti-bacterial, we create a surface that is more hostile towards tissue integration. If we fabricate a surface that promotes cell adhesion and proliferation, this also creates favourable conditions for adhesion and spreading of other microorganisms.

For future work, I propose *in vitro* characterization of the composite CAT-CHIT composite films. For the films containing bioceramic particles, such as HA and TiO<sub>2</sub>, I suggest *in vitro* characterization for the purpose of determining cell viability, but for the Ag containing coatings, I propose the anti-bacterial effect of incorporation of Ag within the CAT-CHIT matrix should be studied. In addition to *in vitro* testing, *In vivo* characterization could be performed for both the CAT-CHIT and CAT-PLL films. In terms of the composite BAS coatings, drug release studies must be performed to determine the drug release profile. *In vitro* anti-bacterial testing must also be conducted to determine the efficacy of the incorporated anti-biotic, tetracycline, for prevention of post-operative infection. I also plan to develop coating fabrication techniques utilizing pure BA, which have previously not been explored for use as dispersing agents or coating fabrication.

## Chapter 9: Contributions

### 9.1 Peer-reviewed Publications

1. S. Saha\*, A. Victorious\*, R. Pandey, A. Clifford, I. Zhitomirsky, L. Soleymani, DNA nano-rulers enable programmable electrochemical biosensing by modulating plasmonic hot electron transfer, *Nature Communications*, submitted 07/08/2019.
2. A. Victorious\*, A. Clifford\*, S. Saha, I. Zhitomirsky, L. Soleymani, Integrating TiO<sub>2</sub> Nanoparticles within a Catecholic Polymeric Network Enhances the Photoelectrochemical Response of Biosensors, *The Journal of Physical Chemistry C*, 2019, 123, 16186-16193.
3. Z.Z. Wang, A. Clifford, J. Milne, R. Matthews, I. Zhitomirsky, Colloidal-electrochemical fabrication strategies for linear polyethylenimine composites, *Journal of Colloid and Interface Science*, 2019, 552 1-8.
4. A. Clifford, B.E.J. Lee, K. Grandfield, I. Zhitomirsky, Biomimetic modification of poly-l-lysine and electrodeposition of nanocomposite coatings for orthopaedic applications, *Colloids and Surfaces B: Biointerfaces*, 2019, 176, 115-121.
5. A. Clifford and I. Zhitomirsky, Aqueous electrophoretic deposition of drugs using bile acids as solubilizing, charging and film-forming agents, *Materials Letters*, 2018, 227, 1-4. **Featured Letter**
6. M. Albert, A. Clifford, I. Zhitomirsky, O. Rubel, Adsorption of maleic acid monomer on the surface of hydroxyapatite and TiO<sub>2</sub>: a pathway toward biomaterial composites. *ACS Applied Materials & Interfaces*, 2018, 10 (29), 24382–24391.
7. A. Clifford, X. Pang, I. Zhitomirsky, Biomimetically modified chitosan for electrophoretic deposition of composites, *Colloids and Surfaces A: Physicochemical and Engineering Aspects*, 2018, 544, p.28-34.
8. X. Zhao, A. Clifford, R. Poon, R. Mathews, I. Zhitomirsky, Carboxymethyl cellulose and composite films prepared by electrophoretic deposition and liquid-liquid particle extraction, *Colloid and Polymer Science*, 2018, 298(5), 927-934.

9. T. Zhang, X. Zhao, R. Poon, A. Clifford, R. Mathews, I. Zhitomirsky, Synthesis and liquid-liquid extraction of non-agglomerated  $\text{Al}(\text{OH})_3$  particles for deposition of cellulose matrix composite films, *Journal of Colloid and Interface Science*, 2017, 508, 49-55.
10. A. Clifford, M.S. Ata, I. Zhitomirsky, Synthesis, liquid – Liquid extraction and deposition of hydroxyapatite nanorod composites, *Materials Letters*, 2017, 201(15), 140-143.
11. R. Chen, M. S. Ata, X. Zhao, A. Clifford, I. Puri, I. Zhitomirsky, Strategies for liquid-liquid extraction of oxide particles for applications in supercapacitor electrodes and thin films, *Journal of Colloid and Interface Science*, 2017, 499, 1-8.
12. R. Poon, X. Zhao, M.S. Ata, A. Clifford, I. Zhitomirsky, Phase transfer of oxide particles for application in thin films and supercapacitors, *Ceramics International*, 2017, 43(11), 8314-8320.
13. A. Clifford\*, D. Luo\*, I. Zhitomirsky, Colloidal strategies for electrophoretic deposition of organic-inorganic composites for biomedical applications, *Colloids and Surfaces A: Physicochemical and Engineering Aspects*, 2017, 516, 219-225.

*\*Indicates Both authors contributed equally to this work*

## 9.2 Patents

L. Soleymani, I. Zhitomirsky, A. Victorious, A. Clifford, Photoelectrodes with Catecholic Polymer Films, Provisional Patent Filed 19/06/2019, No. 62863540

## 9.3 Conference Presentations

1. A. Clifford, B.E.J. Lee, K. Grandfield, I. Zhitomirsky, “Electrophoretic deposition of bioactive catechol-modified poly-l-lysine nanocomposite films for orthopaedic coating applications”. *CBS 2019: Annual Meeting of the Canadian Biomaterials Society*. May 21-24 2019. Quebec City, Canada. Poster.



2. A. Clifford and I. Zhitomirsky, “Biomimetic Modification of Biopolymers for Electrochemical Synthesis of Organic-Inorganic Composites”. **2018 Materials Research Society Fall Meeting & Exhibit**. November 25-30, 2018. Boston, U.S.A. Poster. **MRS Best Poster Award Nominee**
3. A. Clifford and I. Zhitomirsky, “Fabrication of Composite Coatings for Drug Delivery Using Bile Acid Salts”. **2018 Materials Research Society Fall Meeting & Exhibit**. November 25-30, 2018. Boston, U.S.A. Poster.
4. A. Clifford and I. Zhitomirsky. “Organic-inorganic Composite Coating Fabrication Techniques for Biomedical Applications”. **ICANM 2017: International Conference and Exhibition on Advanced & Nano Materials**. August 7-9, 2017. Toronto, Canada. Oral.